Microscopic Theory of Coherent and Incoherent Optical Properties of Semiconductor Heterostructures

Dissertation
zur
Erlangung des Doktorgrades
der Naturwissenschaften
(Dr. rer. nat.)

dem Fachbereich Physik
der Philipps-Universität Marburg
vorgelegt

von
Martin Schäfer

aus Marburg

Marburg(Lahn), 2008

Vom Fachbereich Physik der Philipps-Universität Marburg
als Dissertation angenommen am 25.08.2008

Erstgutachter: Prof. Dr. S.W. Koch
Zweitgutachter: Prof. Dr. W. Stolz

Tag der mündlichen Prfung: 02.09.2008

Für Marianne

Zusammenfassung

Während der letzten Jahrzehnte sind Halbleiter wegen ihrer interessanten elektrischen Eigenschaften zu einem wichtigen Grundmaterial für eine Vielzahl technologischer Anwendungen geworden. Halbleiter zeigen beispielsweise im Gegensatz zu Metallen eine mit der Temperatur ansteigende Leitfähigkeit und es ist möglich, die Leitfähigkeit eines Halbleiters gezielt zu verändern indem man ihn bewusst verunreinigt. Dieses sogenannte *Dotieren* erlaubt es Bauteile mit genau definierten Leitfähigkeitseigenschaften herzustellen. Beispiele für solche Bauteile sind Dioden und Transistoren. Letztere haben schließlich die Entwicklung moderner Computer ermöglicht.

Unglücklicherweise führen dieselben physikalischen Prozesse, die eine gezielte Gestaltung der elektronischen Charakteristika von Halbleiterbauelementen erlauben, dazu, dass Halbleitereigenschaften sehr sensitiv auf ungewollte Verunreinigungen reagieren. Deswegen bezeichnete Wolfgang Paul Anfang der 1920er Jahre die Halbleiterphysik als "Dreckphysik". Mit modernen Epitaxiemethoden ist es jedoch heute möglich, Halbleitermaterialen auf einzelne Atomlagen genau zu wachsen und dabei eine sehr hohe Materialreinheit zu erreichen [1].

Die interessanten elektrischen Eigenschaften von Halbleitern sind auf ihre spezielle Bandstruktur zurückzuführen. Im Gegensatz zu Leitern und ähnlich zu Isolatoren haben Halbleiter im Grundzustand ein gänzlich gefülltes Valenzband und ein leeres Leitungsband. Die beiden Bänder sind energetisch durch die sogenannte Bandlücke getrennt. Im Vergleich zu Isolatoren ist die Bandlücke energetisch klein und liegt im Bereich von etwa 1 eV, so dass eine Anregung der Elektronen vom Valenzband in das Leitungsband möglich ist. Durch die Anregung bleiben im Valenzband Lücken in der Elektronenbesetzung zurück. Diese Lücken werden auch *Löcher* genannt und können quantenmechanisch wie Quasi-Teilchen behandelt werden. Die Löcher haben genau gegenteilige Ladung, Spin und freie Teilchenmasse wie die angeregten Elektronen. Abhängig von der genauen Struktur des Halbleiterbauteils und der Umgebungsbedingungen können sich die angeregten Elektronen ähnlich den freien Elektronen eines Metalls verhalten und zur Leitfähigkeit beitragen [2].

Neben den interessanten elektrischen Eigenschaften besitzen Halbleiterheterostrukturen auch bemerkenswerte optische Eigenschaften [3], da ihre Bandlückenenergie oftmals Wellenlängen im optischen Bereich entspricht. Aus diesem Grund kann auch sichtbares Licht dazu verwendet werden, die Elektronen im Halbleitermaterial anzuregen. Umgekehrt kann die Rekombination eines Elektron-Loch-Paares zu strahlender Emission im optischen Bereich führen. Diese Prozesse werden technologisch in wirtschaftlich sehr bedeutenden Anwendungen wie Leuchtdioden (LEDs), Laserdioden und Festkörperlasern genutzt [4–6]. So wurden beispielsweise alleine im Jahr 2006 mehr als 800 Millionen Laserdioden verkauft [7]. Optische Halbleiterbauteile finden heute eine Vielzahl von Anwendungen in so unterschiedlichen Bereichen wie zum Beispiel in DVD-Playern, Laserpointern, Lichtleitern, Laser Druckern, Barcode Lesegeräten, in der Medizintechnik oder der Laserchirurgie und der Messtechnik.

Zur Zeit werden immer mehr Glühbirnen und sogar Halogenlampen durch LEDs ersetzt, die eine wesentlich bessere Energieeffizienz aufweisen. Zusätzlich sind LEDs relativ kostengünstig in der Herstellung und haben eine lange Lebensdauer. Da die Emissionscharakteristika der LEDs stark von deren Aufbau und dem jeweils verwendeten Material abhängen, wird großer Aufwand betrieben neue Bauformen zu entwickeln, die optimierte Emissionseigenschaften zeigen. Oftmals werden für den Bau von LEDs niedrigdimensionale Halbleiterstrukturen wie beispielsweise Quantenfilme oder Quantendrähte verwendet, die in eine komplizierte dielektrische Umgebung eingebettet sind. Die niedrige Dimensionalität dieser Halbleiterstrukturen führt zur Einschränkung der Elektronenbeweglichkeit auf 2 Dimensionen in Quantenfilmen und auf eine Dimension in Quantendrähten. Deshalb unterscheiden sich die Zustandsdichten in diesen niedrigdimensionalen Strukturen von denen in dreidimensionalen Halbleiterkristallen, so dass das Verhalten von Elektronen und die Lichtemission im Allgemeinen von der Dimenisonalität der untersuchten Struktur abhängt.

Silizium ist der vielleicht bestverstandene Halbleiter und die meisten Halbleiterbauteile werden auf Silziumbasis gefertigt. Aufgrund der langjährigen technischen Erfahrung mit Silizium ist es mittlerweile das Material, das am reinsten hergestellt werden kann. Es äußerst erstrebenswert, einen Laser auf Siliziumbasis zu bauen, da ein solcher Laser neue Möglichkeiten eröffnen würde, das Design der optischen und der elektronischen Eigenschaften miteinander zu verbinden. Unglücklicherweise ist Silizium ein indirekter Halbleiter. Eine Verwendung als optisch aktives Material in Lasern kommt deshalb nicht in Frage. Es hat sich sogar gezeigt, dass gar der Bau eines Lasers, der auf Silizium aufgewachsen wird, ausgesprochen schwierig ist. Ein Grund für diese Schwierigkeit ist, dass Materialien, die eine ähnliche Gitterkonstante wie Silizium besitzen und sich gitterstörungsfrei auf Silizium aufwachsen lassen, in den allermeisten Fällen selber indirekte Halbleiter sind. Materialien mit unterschiedlicher Gitterkonstante führen jedoch zu Verspannungen und anderen Störungen, die den Laserbetrieb stark behindern gar unmöglich machen. Der Bau eines Lasers auf Siliziumbasis ist folglich extrem schwierig. Aufgrund dieser Schwierigkeiten ist es eine interessante Aufgabe, die mikroskopischen Prozesse zu untersuchen, die eine Verwendung von Silizium in Laserstrukturen verhindern. Eine wichtige Fragestellung in diesem Zusammenhang ist, ob es überhaupt ein Regime geben kann, in dem indirekte Halbleiter als optisch aktives Material in Halbleitern verwendet werden können. Diese Frage wird innerhalb der vorliegenden Arbeit diskutiert werden.

Zusätzlich zu den interessanten elektronischen und optischen Eigenschaften die Halbleiter besitzen, sind sie auch hervorragende Materialen, um die Quantennatur von Vielteilchenwechselwirkungen zu untersuchen. Im Zusammenhang mit diesen Vielteilchenwechselwirkung wurde viel Forschungsarbeit an Quasi-Teilchen geleistet. Beispiele für solche Quasi-Teilchen, die in Halbleitern vorkommen sind Phononen, die quantisierte Gitterschwingungen beschreiben, Exzitonen, die ein aufgrund Coulomb-Wechselwirkung gebundenes Elektron-Loch-Paar darstellen, und Polaritonen, die ein Quasi-Teilchen beschreiben, das sich aus einem Photon und einem Exziton zusammensetzt und in Quantenresonatoren entstehen kann. Vielfach wurde versucht, Bose-Einstein Kondensate dieser Quasi-Teilchen herzustellen (für Exzitonenkondensate siehe [8–13] und für Polarito-

nenkondensate [14–17]). In der Literatur herrscht momentan jedoch immer noch eine Kontroverse darüber, ob dies bereits gelungen ist oder ob überhaupt die Möglichkeit besteht, Exzitonen- und Polaritonenkondensate herzustellen. Grund für diese Kontroverse ist die fermionische Substruktur von Exzitonen, die sie zu nicht-idealen Bosonen macht. Im Rahmen der vorliegenden Arbeit wird gezeigt werden, dass die Erzeugung eines Exzitonenkondensats mit Hilfe inkohärenter Emission möglich ist.

Eine weitere Eigenschaft von Exzitonen, die die Bildung von Exzitonenkondensaten und gar die Beobachtung von Exzitonen allgemein erschwert, ist, dass Exzitonen in Quantenfilmen mit verschwindendem Schwerpunktsimpuls auf Zeitskalen von 10 Pikosekunden zerfallen. Wegen dieser schnellen Zerfallszeit würde auch ein Exzitonenkondensat, das sich aus ebensolchen Exzitonen mit verschwindendem Schwerpunktsimpuls zusammensetzt, auf derselben Zeitskala zerfallen. Aus diesem Grunde ist es sicherlich erstrebenswert eine Umgebung zu finden, in der Exzitonen eine längere Lebenszeit haben. Um dieses Ziel zu erreichen, wird in dieser Arbeit der Effekt von Mehrfachquantenfilmstrukturen auf die Lebenszeit von Exzitonen in Quantenfilmen untersucht.

Der Zerfall von Exzitonen geht einher mit phaseninkohärenter Lichtemission, sogenannter Photolumineszenz (PL). Lange Zeit wurde angenommen, dass exzitonische Resonanzen in PL-Spektren ein sicheres Zeichen für die Existenz von Exzitonen im untersuchten System sind. Diese Annahme wurde in Frage gestellt,als Berechnungen zeigten, dass auch ungebundenes Elektron-Loch-Plasma Lumineszenz derselben Frequenz aussendet [18, 19]. Es konnte jedoch gezeigt werden, dass Terahertzresonanzen, die Übergängen zwischen unterschiedlichen Exzitonenzuständen entsprechen, eindeutige Hinweise auf die Existenz von Exzitonen sind [20–25]. Ein großer Nachteil der Terahertzmessungen ist, dass sie insensitiv gegenüber der Schwerpunktsimpulsverteilung von Exzitonen sind. Das führt dazu, dass eventuelle Exzitonenkondensate mit Hilfe von Terahertzspektroskopie nicht von nicht-kondensierten Exzitonen unterschieden werden können. Außerdem konnte mittlerweile eine Strategie erarbeitet werden, die es erlaubt anhand der PL-Spektren zu entscheiden, ob Exzitonen im System sind oder nicht [18].

Neben den Vielteilchenwechselwirkungen im Halbleitermaterial ist der Anregunsprozess des Halbleiters selber ein interessantes Forschungsgebiet. In diesem Zusammenhang unterscheidet man die Anregung mit Hilfe verschiedener Lichquellen, deren Emission unterschiedliche Quantenstatistiken aufweisen [26]. Es zeigt sich, dass jede Quantenstatistik einen charakteristischen Quantenzustand im Halbleiter anregt. Viele dieser speziellen Zustände zeigen hochinteressante Eigenschaften. Anwendungen finden sich zum Beispiel im Bereich des Quantencomputers, bei dessen Bau beispielsweise die genau definierte Emission einzelner Photonen [27, 28] und Verschränkungseffekte [29, 30] benötigt werden.

Ein Beispiel für zwei Lichtquellen, die unterschiedliche Quantenstatistiken aufzeigen, sind die Emission eines Lasers und die Emission eines thermischen Strahlers. Die Laseremission ist phasenkohärent, d.h. alle emittierten Photonen tragen dieselbe Phase. Der Ursprung dieser Kohärenz ist der Prozess der stimulierten Emission, der unter anderem die Verstärkung im optisch aktiven Material eines Lasers bewirkt. Im Zuge dieses Prozesses induziert ein Photon die Rekombination eines Elektron-Loch-Paares unter Emission eines zweiten Photons. Das zweite Photon trägt dann die gleiche Phasenin-

formation wie das erste Photon. Aufgrund der Phasenkohärenz hat das emittierte Licht ein messbares klassisches elektrisches Feld. Dieses klassische elektrische Feld induziert eine Polarisation, sobald es auf Halbleitermaterial trifft.

Im Gegensatz zum Laserlicht ist die Emission einer thermischen Lichtquelle durch spontane Emission verursacht und daher vollständig inkohärent. Jedes Photon hat also eine vollständig zufällige Phaseninformation. Das führt dazu, dass sich die elektrischen Felder, die zu den einzelnen Photonen gehören, herausmitteln und folglich kein klassisches elektrisches Feld messbar ist. Stattdessen wird das elektrische Feld ausschließlich von Quantenfluktuation bestimmt. Folglich induziert ein thermischer Strahler auch keine maktroskopische Polarisation. Stattdessen dominieren quantenmechanische Korrekturen, sogenannte Korrelationen, den Quantenzustand. Somit ist der Quantenzustand, der von thermischer Emission angeregt wird, ein anderer als der Zustand, der von Laserlicht angeregt wird.

Eine theoretische Beschreibung der Licht-Materie-Wechselwirkung im kohärenten Regime wird durch die Halbleiter-Blochgleichungen (SBE) ermöglicht. Die entsprechenden Gleichungen im inkohärenten Regime sind die Halbleiter-Lumineszenz-Gleichungen (SLE). Beide Gleichungssysteme können die Coulombwechselwirkung der Ladungsträger und, falls gewünscht, auch die Wechselwirkung mit Phononen auf mikroskopischer Ebene beschreiben. Diese Vielseitigkeit erlaubt es mit Hilfe der beiden Sätze von Gleichungen ein breites Spektrum an Effekten konsistent zu beschreiben [31, 32]. Prinzipiell ist es gar möglich, SBE und SLE zu koppeln. Die aus dieser Kopplung entstehende Theorie beschreibt erfolgreich die Wechselwirkungen von kohärenten und inkohärenten Prozessen und erklärt beispielsweise Sekundäremissionen [33].

Im Rahmen dieser Arbeit wird sowohl der kohärente als auch inkohärente Phänomene untersucht. Zu diesem Zweck wird in Kapitel 2 das untersuchte Quantenfilmsystem und der Hamilton Operator, der dieses System beschreibt, vorgestellt. In Kapitel 3 werden dann die notwendigen Gleichungen angegeben, die die kohärente optische Antwort des Systems beschreiben. Insbesondere wird das Modell für die Ladungsträgerstreuung erweitert, um auch indirekte Halbleiter beschreiben zu können. Dieses erweiterte Streumodell wird dann dazu verwendet, Absorptionsspektren eines indirekten Germanium-Quantenfilms kurze Zeit nach seiner Anregung zu analysieren. In diesem Zusammenhang kann gezeigt werden, dass sich bei Anregung in der Nähe des Γ-Punktes der optische Gewinn auf eine kurze Zeitspanne von etwa 200 Femtosekunden nach der Anregung beschränkt. Danach führt die Ladungsträgerstreuung dazu, dass die Elektronen vom Γ-Punkt zum L-Punkt relaxieren. Entsprechende gemessene und numerisch berechnete Absorptionsspektren zeigen hervorragende Übereinstimmung. Mit Hilfe eines Vergleiches von numerisch berechneter Absorption für unterschiedliche Aufteilungen der Elektronen auf L-Punkt und Γ-Punkt und experimentell bestimmten Absorptionsspektren für verschiedene Zeitpunkte nach der Anregung, kann eine Streuzeit vom Γ-Punkt zum L-Punkt von etwa 140 Femtosekunden bestimmt werden.

In Kapitel 4 wird ein Modell vorgestellt, dass es erlaubt, den Einfluss der dielektrischen Umgebung auf die Quantenfilmabsorption, -reflektion und -transmission zu untersuchen. Dazu wird eine Transfermatrix-Methode genutzt, die es ermöglicht, die partiellen Reflektionen eines Hintergrundbrechungsindexprofils zu beschreiben. Die mikroskopisch

berechnete Antwort des Quantenfilms wird in diese Transfermatrix-Methode eingebaut und die so gewonnenen Spektren werden mit experimentellen Spektren verglichen. Die numerisch berechneten Daten erklären die gemessen Spektren sehr gut.

Der Einfluss der dielektrischen Umgebung auf die PL wird in Kapitel 6 untersucht. Aufgrund der Quantennatur der PL ist es im Allgemeinen nicht möglich, die dielektrische Umgebung und die Quantenfilmemission getrennt voneinander zu betrachten. In dieser Arbeit wird eine Näherung vorgestellt, die diese Trennung erlaubt, falls der Einfluss der Kopplung nicht zu groß ist. Dazu wird zuerst die PL eines Quantenfilms ohne das dielektrische Medium berechnet. Das geschieht mittels der Halbleiter-Lumineszenz-Gleichungen, die in Kapitel 5 vorgestellt werden. Die dielektrische Umgebung wird dann mit Hilfe einer strukturabhängigen Filterfunktion beschrieben. Das Spektrum der vollen Quantenfilmstruktur wird dann bestimmt, indem man die reine Quantenfilm-PL mit der Filterfunktion multipliziert. Im Regime schwacher Licht-Materie-Kopplung kann der Einfluss des stimulierten Terms durch das Einführen einer radiativen Verbreiterung simuliert werden. Dies ist bei starker Licht-Materie-Kopplung nicht mehr möglich. In diesem Fall führt der stimulierte Term zur Normal-Moden-Aufspaltung, die durch die Filterfunktionsnäherung nicht beschrieben werden kann.

In Kapitel 7 wird schließlich der Einfluss einer Mehrfachquantenfilmstruktur auf die inkohärente Emission besprochen. Im Falle niedriger Ladungsträgerdichten zeigt sich eine Unterdrückung der Emission, die durch korrelierte Prozesse hervorgerufen wird, bei denen die Kombination eines Elektron-Loch-Paares in einem Quantenfilm mit der Erzeugung eines analogen Elektron-Loch-Paares in einem anderen Quantenfilm einhergeht. Der stimulierte Term führt in Mehrfachquantenfilmstrukturen zu einer Verbreiterung des Emissionspeaks. Die Unterdrückung der Quantenemission geht einher mit einer Verlängerung der exzitonischen Lebenszeit. Ein lineares Wachstum der Lebenszeit mit steigender Quantenfilmzahl wird festgestellt. Ferner werden die größten Effekt auf die Lebenszeit von Exzitonen in Quantenfilmstrukturen mit $\lambda/2$ Abstand und bei niedrige Ladunsträgertemperaturen und -dichten gefunden. Abschließend wird gezeigt, dass sich in radiativ gekoppelten Mehrfachquantenfilmsystem durch inkohärent Emission Exzitonenkondensate aufbauen, auch wenn zu Beginn nur unkorreliertes Elektron-Loch-Plasma vorliegt.

Auch wenn mit der hier präsentierten Theorie sich bereits eine Vielzahl von Problemen konsistent beschreiben lassen, so gibt es doch einige natürliche Erweiterungen der Theorie. So werden in der hier präsentierten Theorie nur Einteilchengrößen in die Ladungsträgerstreuung einbezogen. Eine vollständinge Einbindung der Streuterme würde es erlauben, den Einfluss von unterschiedlichen Populationen und Korrelation auf die optische Antwort von Quantenfilmen zu untersuchen. Zum Beispiel wäre es möglich, den Blaushift der Exzitonenresonanz bei Anwesenheit echter Exzitonenpopulationen zu analysieren. Ausserdem könnte der Einfluss durch Anregungen unterschiedlicher Lichtstatistik untersucht werden. Die Verwendung der mikroskopischen Streuung bei der Berechnung von PL aus Quantenresonatoren ermöglicht die Untersuchung von Polaritonenkondensaten.

Eine weitere Aufgabe für die Zukunft wäre die Kopplung von SBE und SLE. Diese Kopplung würde eine Untersuchung des vollständigen Licht-Materie-Wechselwirkungs-

prozess beginnend mit der Anregung durch Licht mit einer gegebenen Quantenstatistik, über den Dephasierungsprozess bis hin zur inkohärenten Emission zu untersuchen. Eine solche Theorie würde tiefgehende Einsichten in die Natur der Lichtstatistik und der Quatenkorrelationen liefern.

Contents

1. Introduction

During the last decades, semiconductors have become increasingly important for many technological applications due to their intriguing electronic properties. As an example, the conductivity of a semiconductors rises with increasing temperature which is opposite to the observations in metals. It is possible to modify the conductivity by the selective introduction of impurities. This so called *doping* allows for designing devices with well defined conduction properties like for example diodes or transistors. The invention of latter ones has been an important step in the development of modern computers. Unfortunately, the same physical processes that allow to design the electronic characteristics make semiconductor properties very sensitive to undesired impurities such that Wolfgang Pauli called semiconductor physics "dirt physics" in the 1920s. Today, modern epitaxy techniques allow to grow high-quality semiconductor devices with growth accuracies of one single atomic monolayer and a minimum of impurities [1].

The origin of the interesting electronic properties of semiconductors is their special band structure. In contrast to conductors and similar to insulators, semiconductors have a filled valence band and an empty conduction band in the ground state. These bands are energetically separated by the band-gap energy. Compared to insulators, the band-gap energy is small (on the order of 1 eV) such that electrons can be excited from the valence band to the conduction band. The missing electrons in the valence band are often called *holes* and treated like quasi-particles that have opposite charge, spin and free-particle mass compared to the excited electrons. Depending on the structure of the semiconductor device and the environmental conditions, the electrons in the conduction band may act like the free electrons of a conductor and thus contribute to the conductivity [2].

Besides the intriguing electronic properties, semiconductor heterostructure have remarkable optical properties due to their band-gap energy that often corresponds to photon energies in the visible regime [3]. Thus, visible light may be used to excite electrons in semiconductors and the opposite process may lead to the emission of visible light. These processes are widely used in applications of particular economical importance like light-emitting diodes (LEDs) [4], laser diodes or solid state lasers [5, 6]. In the year 2006, more than 800 million laser diodes have been sold worldwide [7], making semiconductor optics a multi-billion Dollar market. Today, we find optical semiconductor devices in a multitude of applications including DVD-players, laser pointers, optical fibers, laser printers, bar-code readers, in medical apparatuses or in the laser surgery and the measurement technology.

At present, more and more electric light-bulbs and even neon lamps are replaced by LEDs that have a higher energy efficiency. On top of that, LEDs are relatively cheap in production and show a long durability. Since the emission properties of LEDs

strongly depend on the exact structure and material of the LED, a huge effort is made to find new LED structures with improved light-emission characteristics. Often, LEDs contain low dimensional heterostructures like quantum-wells (QWs) or quantum wires that are embedded inside a complicated dielectric environment. Due to their reduced dimensionality, QWs and quantum wires exhibit a strong electron confinement in one or two dimensions, respectively. Thus in these systems, the density of states is different from that of a three-dimensional semiconductor crystal such that electrons in QWs generally behave different from those in a three-dimensional crystal.

Silicon is perhaps the best known semiconductor material since it is the basis of most electronic semiconductor devices. Due to the long technological experience with that material, silicon is also the material that can be created with the highest purity. It is highly desirable to grow laser structures on a silicon basis because a laser based on silicon would establish new possibilities in combining optical and electronic properties in semiconductor devices. Unfortunately, silicon is an indirect band-gap semiconductor such that it cannot be used as the optically active region in laser structures. Moreover, even the growth of a laser on a silicon basis is very difficult because materials that could act as optically active regions introduce strain and other disturbances due their different lattice constants. Thus, the development of a laser based on silicon is extremely difficult. As a consequence, it is interesting to investigate the microscopic processes in indirect semiconductors preventing them from being applicable for laser structures. An important question in this context is whether there is a regime in which lasing from indirect semiconductors is possible. Thus, we will discuss this question in this thesis.

Apart from the intriguing electronic and light-emission properties, semiconductors heterostructure are also an excellent material in which the quantum nature of many-particle interactions may be investigated. In this context, a lot of research has been done on quasi-particles. Examples for such quasi-particles are phonons, excitons and polaritons where phonons describe the quantized lattice vibrations. Excitons are Coulomb-bound electron-hole pairs and polaritons describe a coupled photon-exciton system which appears in semiconductor cavities. Many attempts have been made to create Bose-Einstein condensates of these quasi-particles (excitons: [8–13]; polaritons: [14–17]). In the literature there is still a controversy about whether these condensates have been created and if it is possible at all to create such condensates. The reason of this disagreement is the underlying fermionic sub-structure of the excitons that makes them non-ideal bosonic particles. In this work, it will be shown that under incoherent emission conditions it is possible to create an exciton condensate in multiple-quantum-well (MQW) systems.

Another exciton property that complicates the creation of an exciton condensate and the investigation of excitons in general is that in QWs excitons with vanishing center-of-mass momentum exhibit a fast recombination on a 10-picosecond (ps) time scale. Thus, a condensate that consists of these quasi-particles vanishes on the same time scale. For this reason, it is desirable to find exciton-friendly conditions that allow for an enhanced exciton lifetime. In this work, the influence of a MQW structure on the exciton lifetime will be investigated.

The recombination of the excitons causes incoherent emission, i.e. photoluminescence (PL). For a long time, it was widely believed that exciton resonances in PL spectra

indicate the presence of excitons. This was questioned when calculations showed that an unbound electron-hole plasma leads to the same emission peaks [18, 19]. By contrast, it could be shown that terahertz absorption corresponding to transitions between different exciton states is a unique signature of excitons in the system [20–25]. However, in contrast to PL, terahertz absorption cannot distinguish between excitons with different center of mass momenta and thus terahertz cannot be used to decide whether excitons are present in the from of an condensate. Additionally, a strategy has been developed that allows to determine whether the PL originates from excitons or electron-hole plasma [18] such that the PL remains an important tool to characterize the quantum state of an excited semiconductor heterostructures.

Another interesting field of research is the excitation of semiconductors with light sources that have various quantum statistics [26]. Each quantum statistic excites a characteristic quantum state in the semiconductors. These states often have intriguing properties. As an example, light sources with a special quantum statistics are used in the field of quantum computing where a defined emission of photons [27, 28] and entanglement [29, 30] are needed.

Two examples for light sources that exhibit differing light statistics are the emission from a laser and the emission from a thermal light source. The laser emission is phase coherent which means that all photons carry the same phase. The origin of this coherence is the stimulated-emission process that causes the amplification in the optically active region of a laser. During this process, a photon induces the recombination of an electron-hole pair and at the same time the emission of a photon that carries the same phase as the original photon. Due to the phase coherence, the laser light carries a classical electric field such that a macroscopic polarization is induced when the laser pulse hits a QW.

In contrast to the laser light, the emission from a thermal light source is caused by spontaneous emission and thus is entirely incoherent. That means that each photon carries a random phase such that the macroscopic electric field vanishes. Thus, the electric field of thermal light is fully determined by its quantum fluctuations. As a consequence, thermal light does not induce a macroscopic polarization such that the excited quantum state inside the QW is dominated by the quantum-mechanical corrections, the so called correlations.

For the description of the light-matter interaction of a QW in the coherent excitation regime, the semiconductor Bloch equation (SBE) are used. The incoherent regime is described by the semiconductor luminescence equations (SLE). Both sets of equations are able to treat the Coulomb interaction and, if desired, the phonon interaction on a microscopical level beyond the Hartree-Fock approximation. Thus, both theories, SBE and SLE, are able to describe and explain a great variety of effects [31, 32]. In principle it is even possible to couple SBE and SLE. The resulting theory is able to describe interactions between coherent and incoherent processes and explains for example the secondary emission [33].

In this work, we investigate both, the coherent and the incoherent light-emission regime. Thus in Chap. 2, we define the investigated system and introduce the many-body Hamiltonian that describes consistently the light-matter interaction in the classical

and the quantum limit. In Chap. 3, we introduce the SBE that allow to compute the light-matter interaction in the coherent scenario. In this context, we review the carrier scattering in Gallium arsenide (GaAs) and extend the scattering model such that we can also describe scattering in indirect Germanium (Ge) QWs. The extended scattering model is used to investigate the absorption of a Ge QW for different time delays after the excitations. In this context, we analyze whether there is a regime in which optical gain can be realized.

In Chap. 4, we apply a transfer-matrix method to include into our calculations the influence of the dielectric environment on the optical response. It is shown how the microscopic description of the QW via the SBE can be incorporated into the transfer-matrix calculations. This coupled theory, enables us to describe reflection, transmission and absorption of a QW that is embedded inside a complicated dielectric structure.

The SLE for a MQW system are introduced in Chap. 5. It is shown how the PL is described by the SLE and that the information about the dielectric environment enter the SLE in a non-trivial manner. In Chap. 6, we derive a scheme that allows for decoupling environmental effects from the pure PL-emission properties of the QW. We describe the influence of the dielectric environment via a structure-dependent filter function. The PL of the actual QW system is obtained by multiplying this filter function and the free-space PL that describes the quantum emission into a medium with spatially constant background-refractive index. We investigate the validity of this approximation for different coupling situations. In Chap. 7, it is studied how the MQW-Bragg structure influences the PL-emission properties compared to the emission of a single QW device. The relation between the PL and the exciton lifetime is analyzed and conditions are determined that lead to a maximum lifetime enhancement. As a last feature, it is shown that the QW coupling leads to the build-up of an exciton condensate even when the QWs are initially only excited with an uncorrelated electron-hole plasma.

2. Investigated System

2.1. General setup

In this thesis, QW systems that are embedded inside a static one-dimensional stack structure will be investigated. The system may contain one ore more identical QWs with a given narrow width ΔL. The z-direction is taken along the growth axis and will also be called the "perpendicular" direction as opposed to the parallel or in-plane direction in the (x,y)-plane.

If the investigated system contains more than one QW, we introduce the spacing Δs between adjacent QWs. Usually, we will choose uniform spacings but in some cases the spacings may vary. Since we are only interested in radiative coupling effects, we assume the QW spacings to be large enough to prevent electronic coupling. This is justified e.g. for the spacings that are interesting for radiative coupling where Δs is of the order of the wavelength of visible light.

The dielectric environment is assumed to be optically inactive and may contain components like distributed Bragg mirrors (DBR), anti-reflection coatings (AR-coatings), cladding layers etc. These components are described via a frequency-dependent background refractive-index $n(\mathbf{r}, \omega)$ which is constant within each layer.

In the following discussion, we will briefly introduce the approximations that we need to describe the interacting carrier-photon system. These will lead us to the SBE and SLE describing the system in the coherent and the incoherent limit, respectively.

2.2. Hamiltonian

As starting point for the following investigations, we first present a Hamiltonian that provides the description of the carrier and the photon system as well as the light-matter coupling on a fully quantum-mechanical level. A detailed derivation of the Hamiltonian can be found in Refs. [31, 34, 35]. In this thesis, we will restrict ourselves to the description of the different parts of the Hamiltonian and introduce some basic concepts and equations that are relevant for the following discussions.

The full Hamiltonian can be divided according to

$$H = H_0 + H_F + H_C + H_D \,, \tag{2.1}$$

where H_0 and H_C describe the pure carrier part. H_0 contains the information about the free electrons in the background potential of the lattice ions while the Coulomb interaction between the carriers within one QW enters via the Coulomb Hamiltonian H_C.

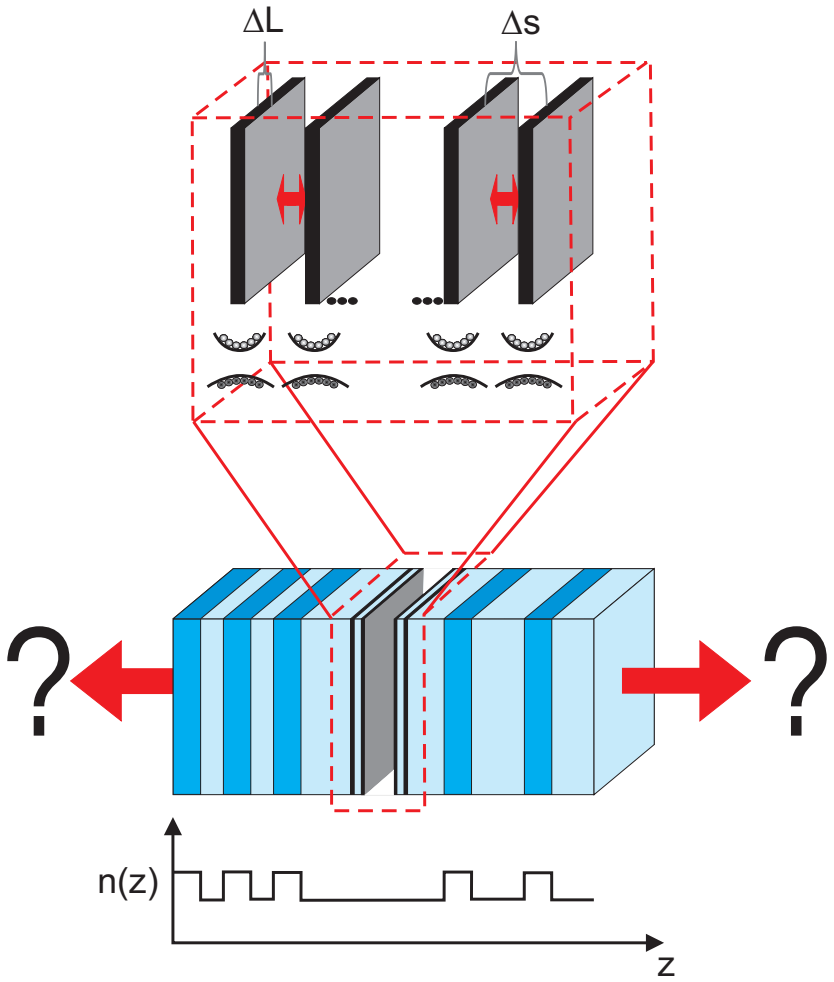

Figure 2.1.: *Schematic drawing of the investigated system:* The system consists of one or more identical QWs. The QWs have a width ΔL and a spacing Δs. For each QW, one valence band and one conduction band is taken into account as indicated by the schematic drawing of the band structure below the QWs. The QWs are radiatively coupled to each other. The MQW system is embedded inside a planar dielectric structure.

The non-interacting light field is given via H_F, and H_D describes the dipole interaction between light and matter. Lattice vibrations have been neglected as they contribute only minorly in the investigated temperature and density regimes. In the following sections, we will discuss the different parts in more detail and describe the assumptions that enter the modeling of the coupled light-matter system.

2.3. The treatment of the carrier system

Due to the quasi-two-dimensional structure of a QW, the carriers experience a strong confinement perpendicular to the QW plane similar to the particle-in-a-box problem.

The corresponding eigenfunctions in growth direction are sinusoidal and we assume them not to leak out of the QW. Therefore, the electrons are captured inside the QWs. The eigenenergies of the particle-in-the-box problem are proportional to $\Delta L^{-2} m^{-1}$, where ΔL is the width of the box and m is the mass of the confined particle. Thus, the energy differences between consecutive eigenenergies become larger for narrower QWs such that for sufficiently narrow QWs only the lowest confinement level for each band needs to be considered.

In parallel direction, the electrons are described as free particles in the background field of the lattice ions. We can therefore describe the electron via the single-particle electron wave-functions in envelope approximation [35]

$$\phi_{m,\mathbf{k},\nu}(\mathbf{r}) = \frac{1}{\sqrt{S}} \xi_{\nu,m}(z) e^{i\mathbf{k}_\parallel \cdot \mathbf{r}_\parallel} w_\nu(\mathbf{r}) \,, \tag{2.2}$$

with the QW index m, the band index ν and the electron wave-vector $\mathbf{k}_\parallel$ that implicitly contains the spin. The constant S is the normalization area. The carrier confinement enters via the confinement function $\xi_{\nu,m}$ while w_ν is the lattice-periodic Bloch-function.

We can now define the field operators $\psi_m(\mathbf{r})$ and $\psi_m^\dagger(\mathbf{r})$ that annihilate or create an electron at the position $\mathbf{r}$ in QW m. The field operators can be expanded in terms of the single-particle wave-functions. Thus, we find

$$\psi_m(\mathbf{r}) = \sum_{\mathbf{k},\nu} a_{m,\nu,\mathbf{k}_\parallel} \phi_{m,\mathbf{k},\nu}(\mathbf{r}), \qquad \psi_m^\dagger(\mathbf{r}) = \sum_{\mathbf{k},\nu} a_{m,\nu,\mathbf{k}_\parallel}^\dagger \phi_{m,\mathbf{k},\nu}^\star(\mathbf{r}) \,. \tag{2.3}$$

Since electrons are fermions, the operators $a_{m,\nu,\mathbf{k}_\parallel}$ and $a_{m,\lambda,\mathbf{k}_\parallel}^\dagger$ obey the fermionic anti-commutation relations

$$\left[a_{m,\lambda,\mathbf{k}_\parallel}, a_{m',\lambda',\mathbf{k}'_\parallel}^\dagger\right]_+ = \delta_{m,m'} \delta_{\lambda,\lambda'} \delta_{\mathbf{k}_\parallel,\mathbf{k}'_\parallel}, \tag{2.4}$$

$$\left[a_{m,\lambda,\mathbf{k}_\parallel}, a_{m',\lambda',\mathbf{k}'_\parallel}\right]_+ = \left[a_{m,\lambda,\mathbf{k}_\parallel}^\dagger, a_{m',\lambda',\mathbf{k}'_\parallel}^\dagger\right]_+ = 0 \,. \tag{2.5}$$

For optical transitions close to the fundamental bandgap, the photon momentum is usually small compared to the relevant electron momenta. Consequently, for optical transitions in direct semiconductors, only electron momenta close to the fundamental band-gap are of relevance such that we can restrict the investigations to the vicinity of the conduction and valence band minima at the Γ-point. In indirect Ge-type QWs, the conduction bands show a minimum at the L-point which is energetically below the Γ-point minimum. In these systems, the electrons experience a fast scattering from the Γ-point to the L-point. For a consistent treatment of the optical properties of Ge, we have to take the conduction band minima at both points into account.

We assume parabolic bands in the vicinity of the Γ- and L-point such that the electron dispersions resemble the dispersion of free electrons with the free electron-mass replaced by the effective masses. Due to the different effective masses of the light-hole and the heavy-hole band, the QW confinement lifts the degeneracy of the two bands at the Γ-point such that only the heavy-hole band needs to be considered. Therefore, we can restrict our calculations to a two-band situation with one valence band (v) and one

conduction band (c). In the ground state, the valence band is completely filled and the conduction band is empty.

The corresponding free-particle Hamiltonian for a direct semiconductor in two-band approximation reads

$$H_0 = \sum_{\mathbf{k}_\parallel, m} \left(\epsilon^c_{\mathbf{k}_\parallel} a^\dagger_{m,c,\mathbf{k}_\parallel} a_{m,c,\mathbf{k}_\parallel} + \epsilon^v_{\mathbf{k}_\parallel} a^\dagger_{m,v,\mathbf{k}_\parallel} a_{m,v,\mathbf{k}_\parallel} \right) . \tag{2.6}$$

It contains the single-particle energies

$$\epsilon^c_{\mathbf{k}_\parallel} = E_g + \frac{\hbar^2 \mathbf{k}_\parallel^{\,2}}{2m_c} \equiv E_g + \frac{\hbar^2 \mathbf{k}_\parallel^{\,2}}{2m_e} = \epsilon^e_{\mathbf{k}_\parallel}, \tag{2.7}$$

$$\epsilon^v_{\mathbf{k}_\parallel} = \frac{\hbar^2 \mathbf{k}_\parallel^{\,2}}{2m_v} \equiv -\frac{\hbar^2 \mathbf{k}_\parallel^{\,2}}{2m_h} = -\epsilon^h_{\mathbf{k}_\parallel}, \tag{2.8}$$

where E_g is the unrenormalized band-gap energy and m_c (m_v) is the effective electron mass in the conduction (valence) band. Alternatively, we can use electron and hole masses m_e and m_h where a hole is a missing electron in the valence band. For indirect Ge-type semiconductors, in the $\mathbf{k}_\parallel$-sum in Eq. (2.6) one needs to distinguish between electrons at the L-point and electrons at the Γ-point, where the L-point electron mass is given by m_L.

The Coulomb interaction between the carriers within one and the same QW enters via the Coulomb Hamiltonian

$$\begin{aligned} H_C = \frac{1}{2} \sum_{\mathbf{k}_\parallel, \mathbf{k}'_\parallel, \mathbf{k}''_\parallel \neq 0} V_{\mathbf{k}''_\parallel} \Big(& a^\dagger_{m,c,\mathbf{k}_\parallel + \mathbf{k}''_\parallel} a^\dagger_{m,c,\mathbf{k}'_\parallel - \mathbf{k}''_\parallel} a_{m,c,\mathbf{k}'_\parallel} a_{m,c,\mathbf{k}_\parallel} \\ & + a^\dagger_{m,v,\mathbf{k}_\parallel + \mathbf{k}''_\parallel} a^\dagger_{m,v,\mathbf{k}'_\parallel - \mathbf{k}''_\parallel} a_{m,v,\mathbf{k}'_\parallel} a_{m,v,\mathbf{k}_\parallel} \\ & + 2 a^\dagger_{m,c,\mathbf{k}_\parallel + \mathbf{k}''_\parallel} a^\dagger_{m,v,\mathbf{k}'_\parallel - \mathbf{k}''_\parallel} a_{m,v,\mathbf{k}'_\parallel} a_{m,c,\mathbf{k}_\parallel} \Big) . \end{aligned} \tag{2.9}$$

In this thesis, we use a quasi-two-dimensional Coulomb-matrix element that contains the carrier confinement in z-direction.

$$V_{\mathbf{q}_\parallel} = \frac{e^2}{2\varepsilon_0 |\mathbf{q}_\parallel|} \int g(z) g(z') e^{-\mathbf{q}_\parallel |z - z'|} dz dz' , \tag{2.10}$$

where e is the electron charge and ε_0 is the electric permeability. The confinement functions of valence-band holes $\xi_v(z)$ and conduction-band electrons $\xi_c(z)$ enter the Coulomb-matrix element via $g(z) = \xi^\star_v(z)\xi_c(z) = \xi_v(z)\xi^\star_c(z)$. For narrow QWs, $\xi_c(z)$ and $\xi_v(z)$ are identical such that the Coulomb-matrix element (2.10) becomes independent of band indices.

The first and the second term of Eq. (2.9) describe the repulsive intraband interactions between carriers in the conduction and the valence band, respectively, while the third term introduces attractive interband interactions between the electrons in the conduction band and holes in the valence band. Coulomb interaction between carriers in different QWs can be neglected due to the large spacing between the QWs that is of the order of wavelength of visible light.

2.4. Electric field

A semi-classical treatment of the electric field is often sufficient for investigations of the linear optical response of the QW system [35]. This is no longer the case when the electric field is exclusively determined by its quantum fluctuations. In particular, the quantum nature of the light-field needs to be considered when we are interested in the PL [34]. In this thesis, the aim is to investigate both the PL and the optical response. For a general description, we consequently have to use a fully quantized electric field that allows for describing the classical limit as well as the quantum nature of the light field.

For the quantization procedure, we use an approach that has been introduced e.g. in Refs. [34–36]. Thus, the electric field is expanded in the mode basis

$$E(\mathbf{r}) = \sum_{\mathbf{q}} i\mathcal{E}_{\mathbf{q}} U_{\mathbf{q}}(\mathbf{r}) B_{\mathbf{q}} + h.c.\,, \tag{2.11}$$

where $\mathcal{E}_{\mathbf{q}} = \sqrt{\frac{\hbar\omega_{\mathbf{q}}}{2\epsilon_0}}$ is the vacuum field amplitude that is fixed by the quantization process. The photon energy $\hbar\omega_{\mathbf{q}}$ belongs to the photon wave-vector $\mathbf{q}$ that implicitly includes the polarization direction. Via minimal substitution, the classical expansion coefficients $B^\dagger_{\mathbf{q}}$ and $B_{\mathbf{q}}$ become the photon creation and annihilation operators for each light mode $U_{\mathbf{q}}$. The operators obey the bosonic commutation relations

$$\left[B_{\mathbf{q}}, B^\dagger_{\mathbf{q}'}\right]_- = \delta_{\mathbf{q},\mathbf{q}'}, \tag{2.12}$$

$$\left[B_{\mathbf{q}}, B_{\mathbf{q}'}\right]_- = \left[B^\dagger_{\mathbf{q}}, B^\dagger_{\mathbf{q}'}\right]_- = 0\,. \tag{2.13}$$

The mode functions $U_{\mathbf{q}}(\mathbf{r})$ are the solutions of the Helmholtz equation

$$\left[\nabla^2 + \frac{n^2(z,\omega)\omega_q^2}{c^2}\right] U_{\mathbf{q}}(\mathbf{r}) = 0 \tag{2.14}$$

and contain the full information about the dielectric environment. The dielectric environment enters the Helmholtz equation via the frequency dependent refractive index $n(z,\omega)$ which is taken to be constant over each layer. The mode functions in that direction may be determined via their continuity conditions at the boundaries of the refractive-index profile [34, 37–39]. Parallel to the QW planes, we assume the refractive index to be constant such that the mode functions in the (x,y)-plane can be described via plane waves.

Due to the geometry of the setup, it is useful to divide the photon wave-vector into an in-plane component $\mathbf{q}_\parallel$ and a component perpendicular to the QW plane $q_\perp$. The three-dimensional photon wave-vector $\mathbf{q} = (\mathbf{q}_\parallel, q_\perp)$ therefore includes information about the angle of incidence as well as the frequency of the light ω_q with $q = \left|\sqrt{\mathbf{q}_\parallel{}^2 + q_\perp^2}\right|$. A more detailed discussion of the dielectric environment and its influence on the light-matter coupling will be given in Chaps. 4 and 6 (see also Ref. [36]).

The corresponding free-light-field Hamiltonian can be expressed in terms of photon creation and annihilation operators,

$$H_F = \sum_{\mathbf{q}} \hbar\omega_q \Big(B^\dagger_{\mathbf{q}} B_{\mathbf{q}} + \frac{1}{2} \Big) \,. \tag{2.15}$$

The light-matter interaction is included in dipole approximation via the dipole Hamiltonian

$$\begin{aligned} H_D \;=\; - \sum_{q_\perp, \mathbf{q}_\parallel, \mathbf{k}_\parallel} \Big(& i\mathcal{E}_{\mathbf{q}} u_{\mathbf{q},m} d_{cv}(\mathbf{q}_\parallel) a^\dagger_{m,c,\mathbf{k}_\parallel+\mathbf{q}_\parallel} a_{m,v,\mathbf{k}_\parallel} B_{\mathbf{q}} \\ & + i\mathcal{E}_{\mathbf{q}} u_{\mathbf{q},m} d_{cv}(\mathbf{q}_\parallel) a^\dagger_{m,v,\mathbf{k}_\parallel} a_{m,c,\mathbf{k}_\parallel-\mathbf{q}_\parallel} B_{\mathbf{q}} \Big) + h.c. \,, \end{aligned} \tag{2.16}$$

where intra-band contributions that are off-resonant for optical excitations have been neglected. The strength of the light-matter coupling is determined by the vacuum field amplitude $\mathcal{E}_{\mathbf{q}}$, the dipole matrix element between valence and conduction band $d_{cv}(\mathbf{q}_\parallel)$ and

$$u_{\mathbf{q},m} = \int dz g_m(z) U_{\mathbf{q}}(z) \,, \tag{2.17}$$

which is the overlap integral between the mode function $U_{\mathbf{q}}(z)$ and the square of the confinement function of the mth QW $g_m(z) = |\xi_m|^2$. Since the confinement function is spatially very narrow compared to the mode function, it can be approximated by a delta distribution such that only the mode function at the QW position applies $u_{\mathbf{q},m} \approx U_{\mathbf{q},m}(z_{QW})$.

2.5. Heisenberg's equation of motion and hierarchy problem

In order to describe the dynamics of the light-matter interaction of a semiconductor heterostructure, we first have to determine the equations of motion of the single photon and carrier operators. We can then derive the time evolution of all relevant expectation values via the dynamics of combinations of these operators.

The time evolution of operators can be determined via Heisenberg's equation of motion. Therefore, we have to calculate the commutator between a general operator $\hat{O}$ and the Hamiltonian introduced in Eq. (2.1),

$$i\hbar \frac{\partial}{\partial t} \hat{O} = \Big[\hat{O}, H \Big]_- \,. \tag{2.18}$$

As shown in Ref. [34], the Coulomb interaction couples expectation values containing combinations of N carrier operators (N-point quantities) to expectation values containing $N+2$ carrier operators. The light-matter interaction couples combinations of N carrier operators to combinations of one photon and N carrier operators. Since the creation or absorption of photons with momentum $\hbar\mathbf{q}_\parallel$ results in a momentum change of

electrons according to $a^\dagger_{\mathbf{k}_\parallel} a_{\mathbf{k}_\parallel+\mathbf{q}_\parallel}$, photon operators are formally equivalent to two carrier operators. Consequently, both interactions couple expectation values containing N carrier operators to expectation values of operator combinations corresponding to $N+2$ carrier operators. The dynamics of these $N+2$-point quantities is then in turn coupled to $N+4$-point quantities and so on such that we end up with an infinite hierarchy of coupled equations of motion.

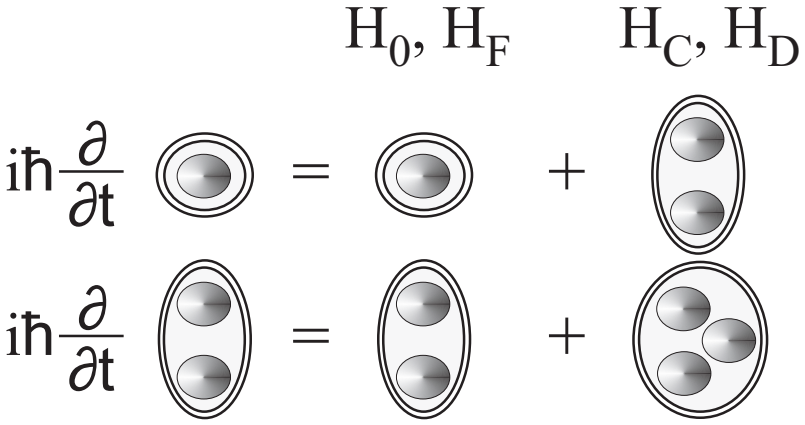

Figure 2.2.: *Schematic visualization of the hierarchy problem:* The Coulomb interaction and the light-matter interaction couple single-particle quantities to two-particle quantities such that the equation of motion for the two-particle quantities is needed to describe the dynamics of the single-particle quantities. In turn, the two-particle quantities are coupled to three-particle quantities and so on. We end up with a hierarchy of infinitely many coupled equations of motion.

Formally, we can write

$$i\hbar\frac{\partial}{\partial t}\langle O_N\rangle = T[\langle O_N\rangle] + V[\langle O_{N+1}\rangle] \tag{2.19}$$

where $\langle O_N\rangle$ denotes a generic N-particle expectation value corresponding to a $2N$-point quantity. The shortcut T indicates the single-particle part of the Hamiltonian containing the free carriers and the free field part. All many-particle interactions that couple to $(N+1)$-particle expectation values are described by the abbreviation V.

In order to close the set of equations on a controllable level, a systematic truncation scheme is needed. One possible approach to deal with the hierarchy problem is the cluster-expansion formalism [20, 40, 41] where we factorize N-particle quantities into all consistent combinations of independent single-particle quantities (singlets), correlated 2-particle quantities (doublets), correlated 3-particle quantities (triplets) and so on.

$$\langle O_2\rangle = \langle O_2\rangle_S + \Delta\langle O_2\rangle \tag{2.20}$$

where the subscript S denotes the singlet part (i.e. Hartree-Fock part) and the Δ indicates the purely correlated part. Analogously, three-particle quantities are factorized

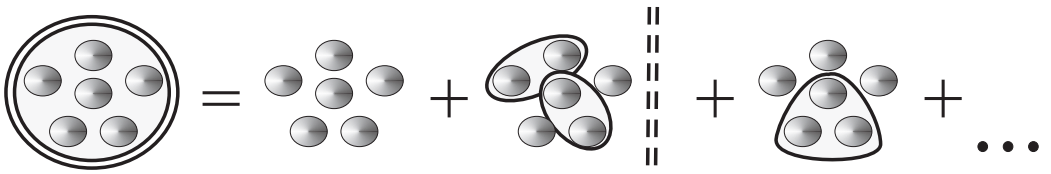

Figure 2.3.: *Diagrammatic presentation of the Cluster Expansion:*An N-particle expectation value may be decomposed into terms containing at most single-particle quantities (singlets), terms containing at most two-particle correlations (doublets), terms containing at most three-particle correlations (triplets) and so on, up to the full N-particle correlation. In this thesis, we fully include the singlets and doublets. The correlated three-particle quantities are treated on an approximative level such that we end up with a closed set of equations that contain at most two-particle quantities.

via

$$\langle O_3 \rangle = \langle O_3 \rangle_S + \langle O_1 \rangle_S \Delta \langle O_2 \rangle + \Delta \langle O_3 \rangle \,. \tag{2.21}$$

In the following, we compute the equations of motion in singlet-doublet approximation which means setting up the equations of motions for all expectation values containing up to two-particle quantities. The occurring triplets are factorized via the cluster-expansion mechanism into singlets, doublets, and the purely correlated three-particle quantities. The correlated three-particle quantities are either neglected or approximated by simple expression such that we end up with a closed set of equations which at most contains two-particle quantities.

3. Coherent excitations and semiconductor Bloch equations

In the first part of this thesis, we want to investigate a QW system in the coherent excitation regime. This regime is typically reached when a laser pulse excites the QW resonantly within the spectral region of interest. Due to the displacement of the electrons, the transverse electric field of the laser leads to the build-up of coherent interband polarization such that all microscopical transitions carry the same phase.

The polarization in turn interacts with the external electric field and with the internal electric field that is induced by the polarization itself. This interaction leads to the creation of uncorrelated electrons and holes. The created carriers undergo scattering processes which cause dephasing of the coherent polarization and lead to the build up of correlations and populations.

Once the coherent polarization has decayed, the system enters the incoherent regime where the expectation values of the electric field and the polarization are zero and the system is dominated exclusively by quantum fluctuations. The incoherent regime will be investigated in the second part of this thesis. For now, we want to concentrate on situations where the coherent polarization is still present and investigate the optical response of QWs consisting of direct and indirect semiconductors under different conditions.

In order to describe the optical response, in Sec. 3.1 the relevant quantities are introduced and it is defined how the microscopical polarization and the absorption are related. In Sec. 3.2, the equation of motion for the coherent polarization is presented and in Sec. 3.3, we will introduce the approximations for the treatment of the carrier scattering in direct GaAs-type QWs. The scattering theory will then be extended to also describe indirect Ge-type semiconductors in Sec. 3.4.

As an example for the influence of the scattering in direct semiconductors, we will review the concept of excitation induced dephasing (EID) [42–45] in Sec. 3.5. The insights which we gain in Sec. 3.5 will guide us to Sec. 3.6, where modifications of the scattering effects due to the indirect band-structure are investigated.

3.1. Absorption and susceptibility

A very efficient experiment to investigate the optical response of a QW system uses two consecutive laser pulses. The first pulse is usually spectrally broad and prepares the system. The second pulse is usually weak and overlaps with the spectral region of interest and probes the system after a certain time delay. The ratio of the measured

transmission spectra with and without the pump pulse defines the optical response of the system [35, 46–48].

In order to explain such experiments theoretically, we define the macroscopic polarization $P(\omega)$ induced by the probe pulse $E(\omega)$. The optical response of the QW is then given by the linear susceptibility

$$\chi(\omega) = \frac{P(\omega)}{\varepsilon_0 E(\omega)}\,. \tag{3.1}$$

The imaginary part of the linear susceptibility is directly related to the absorption while the real part indicates changes of the refractive index [31, 35].

By formally solving the wave equation

$$\left[\frac{\partial^2}{\partial z^2} - \frac{n^2(z)}{c^2}\frac{\partial^2}{\partial t^2}\right]\langle E(z,t)\rangle = \mu_0 g(z)\frac{\partial^2}{\partial t^2}P\,, \tag{3.2}$$

one can derive the relation between true absorption and susceptibility as

$$\alpha(\omega) \equiv 1 - |\mathcal{R}(\omega)|^2 - |\mathcal{T}(\omega)|^2 = \frac{2Im\left[\xi(\omega)\right]}{1 + |\xi(\omega)|^2 + 2Im\left[\xi(\omega)\right]}\,, \tag{3.3}$$

where we have defined

$$\xi(\omega) = \frac{\omega}{n(\omega)c}\chi(\omega)\,. \tag{3.4}$$

The quantities $\mathcal{R}$ and $\mathcal{T}$ are the reflection and transmission coefficients of the sample [31].

In order to connect the macroscopically measured quantities and the microscopic description of the quantum system, we express the macroscopic polarization in terms of the microscopic polarization $p_{\mathbf{k}_\parallel} = \langle a^\dagger_{v,\mathbf{k}_\parallel} a_{c,\mathbf{k}_\parallel}\rangle$ according to

$$P(\omega) = \frac{d_{cv}}{S}\sum_{\mathbf{k}_\parallel} p_{\mathbf{k}_\parallel}(\omega)\,, \tag{3.5}$$

where S is the normalization area. The frequency dependence of the polarization can be derived via Fourier transformation if the time dependence of the polarization is known. As a consequence, the knowledge of the probe pulse and the dynamics of the microscopic polarization yields the linear response of the QW system. Thus, in the next section we introduce the SBE that allow us to calculate the desired dynamics.

3.2. Semiconductor Bloch equations

As we are interested in the optical response, we can treat the probe pulse classically such that the electric field is given by its expectation value $E = \langle E\rangle$. Thus, as a starting point for our theoretical description, we use the Hamiltonian (2.1) and define the classical transverse electric field of the probe pulse via

$$\langle E_{\mathbf{q}_\parallel}\rangle \equiv \frac{d_{c,v}}{S}\int d^3r\, g(z)E(\mathbf{r})e^{i\mathbf{q}_\parallel\mathbf{r}_\parallel} = \sum_{q_\perp} i\mathcal{E}_{\mathbf{q}} u_{\mathbf{q}} d_{cv}(\mathbf{q}_\parallel)\left(\langle B_{\mathbf{q}_\parallel,q_\perp}\rangle + \langle B^\dagger_{-\mathbf{q}_\parallel,q_\perp}\rangle\right)\,. \tag{3.6}$$

For narrow QWs, the square of the confinement functions may be approximated by $g(z) = \delta(z)$ such that only the electric field at the QW position contributes. We use Heisenberg's equation of motion and the cluster-expansion truncation in singlet-doublet approximation to determine the dynamics of the coherent polarization. The result reads [31]

$$\begin{aligned} i\hbar\frac{\partial}{\partial t}p_{\mathbf{k}_\parallel} &= \tilde{\epsilon}_{\mathbf{k}_\parallel} p_{\mathbf{k}_\parallel} \\ &- \left(1 - f^e_{\mathbf{k}_\parallel} - f^h_{\mathbf{k}_\parallel}\right)\left[\langle E_0\rangle + \sum_{\mathbf{k}'_\parallel} V_{\mathbf{k}'_\parallel - \mathbf{k}_\parallel} p_{\mathbf{k}'_\parallel}\right] \\ &+ \sum_{\lambda,\mathbf{k}'_\parallel,\mathbf{q}_\parallel} V_q \left[c^{\mathbf{q}_\parallel,\mathbf{k}'_\parallel,\mathbf{k}_\parallel}_{v,\lambda,\lambda,c} - \left(c^{\mathbf{q}_\parallel,\mathbf{k}'_\parallel,\mathbf{k}_\parallel}_{c,\lambda,\lambda,v}\right)^\star\right] \end{aligned} \tag{3.7}$$

where quantum-optical two-particle correlations of the form $\Delta\langle Ea^\dagger a\rangle$ have been neglected. The neglect of the two-particle correlations is justified since the quantum-optical corrections are small compared to the electric field of the probe pulse. The electron and hole distributions

$$f^e_{\mathbf{k}_\parallel} = \langle a^\dagger_{c,\mathbf{k}_\parallel} a_{c,\mathbf{k}_\parallel}\rangle\,, \tag{3.8}$$

$$f^h_{\mathbf{k}_\parallel} = 1 - \langle a^\dagger_{v,\mathbf{k}_\parallel} a_{v,\mathbf{k}_\parallel}\rangle\,, \tag{3.9}$$

enter the Coulomb-renormalized single-particle energies

$$\tilde{\epsilon}_{\mathbf{k}_\parallel,\mathbf{q}_\parallel} = \epsilon^e_{\mathbf{k}_\parallel} + \epsilon^h_{\mathbf{k}_\parallel} - \sum_{\mathbf{k}'_\parallel} V_{\mathbf{k}_\parallel - \mathbf{k}'_\parallel}\left(f^e_{\mathbf{k}'_\parallel} + f^h_{\mathbf{k}'_\parallel}\right) \tag{3.10}$$

as well as the phase-space-filling factor $\left(1 - f^e_{\mathbf{k}_\parallel} - f^h_{\mathbf{k}_\parallel}\right)$ that describes Pauli-blocking effects if electrons and/or holes are present. The phase-space filling acts as a prefactor for the generalized Rabi-frequency

$$\langle E_0\rangle + \sum_{\mathbf{k}'_\parallel} V_{\mathbf{k}'_\parallel - \mathbf{k}_\parallel} p_{\mathbf{k}'_\parallel} \tag{3.11}$$

that contains the Coulomb renormalization of the electric field leading to excitonic resonances in the absorption spectra. In the low density regime, the phase-space-filling factor is close to unity. When the carrier densities are increased, it becomes smaller such that it reaches zero at the transparency point and eventually becomes negative in the gain regime. Negative values of the phase-space-filling factor effectively change the sign with which the Coulomb interaction enters the SBE such that the excitonic resonances vanish for carrier densities beyond the transparency point and bound exciton states cease to exist.

The scattering of polarization is introduced by coherent carrier correlations $c^{\mathbf{q}_\parallel,\mathbf{k}'_\parallel,\mathbf{k}_\parallel}_{v,\lambda,\lambda,c}$, and $c^{\mathbf{q}_\parallel,\mathbf{k}'_\parallel,\mathbf{k}_\parallel}_{c,\lambda,\lambda,v}$ where λ may either be c or v and

$$c^{\mathbf{q}_\parallel,\mathbf{k}'_\parallel,\mathbf{k}_\parallel}_{\nu,\lambda,\lambda',\nu'} = \Delta\langle a^\dagger_{\nu,\mathbf{k}_\parallel} a^\dagger_{\lambda,\mathbf{k}'_\parallel} a_{\lambda',\mathbf{k}'_\parallel+\mathbf{q}_\parallel} a_{\nu',\mathbf{k}_\parallel-\mathbf{q}_\parallel}\rangle\,. \tag{3.12}$$

The equations of motion for the carriers are given by

$$\hbar\frac{\partial}{\partial t}f^{e}_{\mathbf{k}_\parallel} = 2\mathrm{Im}\left[\mathrm{p}_{\mathbf{k}_\parallel}\left(\langle \mathrm{E}_0\rangle + \sum_{\mathbf{k}'_\parallel}\mathrm{V}_{\mathbf{k}'_\parallel-\mathbf{k}_\parallel}\mathrm{p}_{\mathbf{k}'_\parallel}\right) + \sum_{\lambda,\mathbf{k}'_\parallel,\mathbf{q}_\parallel}\mathrm{V_q c}^{\mathbf{q}_\parallel,\mathbf{k}'_\parallel,\mathbf{k}_\parallel}_{\mathrm{c},\lambda,\lambda,\mathrm{c}}\right], \tag{3.13}$$

$$\hbar\frac{\partial}{\partial t}f^{h}_{\mathbf{k}_\parallel} = 2\mathrm{Im}\left[\mathrm{p}_{\mathbf{k}_\parallel}\left(\langle \mathrm{E}_0\rangle + \sum_{\mathbf{k}'_\parallel}\mathrm{V}_{\mathbf{k}'_\parallel-\mathbf{k}_\parallel}\mathrm{p}_{\mathbf{k}'_\parallel}\right) - \sum_{\lambda,\mathbf{k}'_\parallel,\mathbf{q}_\parallel}\mathrm{V_q c}^{\mathbf{q}_\parallel,\mathbf{k}'_\parallel,\mathbf{k}_\parallel}_{\mathrm{v},\lambda,\lambda,\mathrm{v}}\right]. \tag{3.14}$$

Again, we have neglected the quantum-optical two-particle correlations.

The dominant scattering contributions to the carrier dynamics are the carrier-carrier correlations $c_{\lambda,\lambda,\lambda,\lambda}$ and correlations of the form $c_{\lambda,\bar{\lambda},\bar{\lambda},\lambda}$ describing true exciton contributions. The bar indicates the opposite band index, $\bar{v}=c$ and $\bar{c}=v$.

In the absence of incoherent correlations, the carrier distributions are only driven if coherent polarization is present. Consequently, the coherent laser pulse does not directly create electron and hole populations but first creates polarization. In a second step, the polarization interacts with the renormalized laser field and leads to a build up of populations.

3.3. Treatment of the carrier scattering

In analogy to the procedure for the coherent polarization, we can use Heisenberg's equation of motion and the subsequent application of the cluster-expansion truncation to find the dynamics of the correlation terms

$$\begin{aligned} i\hbar\frac{\partial}{\partial t}c^{\mathbf{q}_\parallel,\mathbf{k}'_\parallel,\mathbf{k}_\parallel}_{\nu,\lambda,\lambda,\bar{\nu}} &= \left(\varepsilon^{\bar{\nu}}_{\mathbf{k}_\parallel-\mathbf{q}_\parallel}+\varepsilon^{\lambda}_{\mathbf{k}'_\parallel+\mathbf{q}_\parallel}-\varepsilon^{\lambda}_{\mathbf{k}'_\parallel}-\varepsilon^{\nu}_{\mathbf{k}_\parallel}\right)c^{\mathbf{q}_\parallel,\mathbf{k}'_\parallel,\mathbf{k}_\parallel}_{\nu,\lambda,\lambda,\bar{\nu}} \\ &+ S^{\mathbf{q}_\parallel,\mathbf{k}'_\parallel,\mathbf{k}_\parallel}_{\nu,\lambda,\lambda,\bar{\nu}} + \left[D^{\mathbf{q}_\parallel,\mathbf{k}'_\parallel,\mathbf{k}_\parallel}_{\nu,\lambda,\lambda,\bar{\nu}}\right]_{\mathrm{coh}} + \left[D^{\mathbf{q}_\parallel,\mathbf{k}'_\parallel,\mathbf{k}_\parallel}_{\nu,\lambda,\lambda,\bar{\nu}}\right]_{\mathrm{inc}} + \left[c^{\mathbf{q}_\parallel,\mathbf{k}'_\parallel,\mathbf{k}_\parallel}_{\nu,\lambda,\lambda,\bar{\nu}}\right]_{\mathrm{T}}, \end{aligned} \tag{3.15}$$

where quantum-optical contributions have been neglected. The renormalized single-particle energies are

$$\varepsilon^{\lambda}_{\mathbf{k}_\parallel} = \epsilon^{\lambda}_{\mathbf{k}_\parallel} - \sum_{\mathbf{k}'_\parallel}V_{\mathbf{k}'_\parallel-\mathbf{k}_\parallel}\langle a^{\dagger}_{\lambda,\mathbf{k}'_\parallel}a_{\lambda,\mathbf{k}'_\parallel}\rangle. \tag{3.16}$$

The coherent doublet term $[D^{\mathbf{q}_\parallel,\mathbf{k}'_\parallel,\mathbf{k}_\parallel}_{\nu,\lambda,\lambda,\bar{\nu}}]_{\mathrm{coh}}$ includes coherent correlations of the form $c_{\nu,\lambda,\lambda,\bar{\nu}}$, while the incoherent doublet term $[D^{\mathbf{q}_\parallel,\mathbf{k}'_\parallel,\mathbf{k}_\parallel}_{\nu,\lambda,\lambda,\bar{\nu}}]_{\mathrm{inc}}$ contains the carrier-carrier correlations $c_{\lambda,\lambda,\lambda,\lambda}$ as well as couplings to true exciton populations $c_{\lambda,\bar{\lambda},\lambda,\bar{\lambda}}$. Triplet correlations that enter the equation are abbreviated by the term $\left[c^{\mathbf{q}_\parallel,\mathbf{k}'_\parallel,\mathbf{k}_\parallel}_{\nu,\lambda,\lambda,\bar{\nu}}\right]_{\mathrm{T}}$.

The singlet contributions are summarized in $S^{\mathbf{q}_\parallel,\mathbf{k}'_\parallel,\mathbf{k}_\parallel}_{\nu,\lambda,\lambda,\bar{\nu}}$ where we have only included terms that are linear in the polarization due to the weak probe pulse. The explicit form of all four singlet terms corresponding to the possible band-index combinations is

structurally very similar. As an example

$$\begin{aligned} S_{v,v,v,c}^{\mathbf{q}_\parallel,\mathbf{k}'_\parallel,\mathbf{k}_\parallel} &= V_{\mathbf{j}_\parallel}\Big[p_{\mathbf{k}_\parallel-\mathbf{q}_\parallel}\left(f^h_{\mathbf{k}_\parallel}f^h_{\mathbf{k}'_\parallel}\bar{f}^h_{\mathbf{k}'_\parallel+\mathbf{q}_\parallel}+\bar{f}^h_{\mathbf{k}_\parallel}\bar{f}^h_{\mathbf{k}'_\parallel}f^h_{\mathbf{k}'_\parallel+\mathbf{q}_\parallel}\right) \\ &\quad - p_{\mathbf{k}'_\parallel}\left(f^h_{\mathbf{k}_\parallel}f^e_{\mathbf{k}_\parallel-\mathbf{q}_\parallel}\bar{f}^h_{\mathbf{k}'_\parallel+\mathbf{q}_\parallel}+\bar{f}^h_{\mathbf{k}_\parallel}\bar{f}^e_{\mathbf{k}_\parallel-\mathbf{q}_\parallel}f^h_{\mathbf{k}'_\parallel+\mathbf{q}_\parallel}\right)\Big] \\ &\quad + V_{\mathbf{q}_\parallel}\Big[p_{\mathbf{k}_\parallel}\left(f^h_{\mathbf{k}'_\parallel}f^e_{\mathbf{k}_\parallel-\mathbf{q}_\parallel}\bar{f}^h_{\mathbf{k}'_\parallel+\mathbf{q}_\parallel}+\bar{f}^h_{\mathbf{k}'_\parallel}\bar{f}^e_{\mathbf{k}_\parallel-\mathbf{q}_\parallel}f^h_{\mathbf{k}'_\parallel+\mathbf{q}_\parallel}\right) \\ &\quad - p_{\mathbf{k}_\parallel-\mathbf{q}_\parallel}\left(f^h_{\mathbf{k}_\parallel}f^h_{\mathbf{k}'_\parallel}\bar{f}^h_{\mathbf{k}'_\parallel+\mathbf{q}_\parallel}+\bar{f}^h_{\mathbf{k}_\parallel}\bar{f}^h_{\mathbf{k}'_\parallel}f^h_{\mathbf{k}'_\parallel+\mathbf{q}_\parallel}\right)\Big]\,. \end{aligned} \tag{3.17}$$

is listed to indicate the general structure. The other singlets together with the explicit form of the doublets can be found e.g. in [31]. In Eq. (3.17), we have used the abbreviations $\bar{f}^{e/h}_{\mathbf{k}_\parallel}=\left(1-f^{e/h}_{\mathbf{k}_\parallel}\right)$ and $\mathbf{j}_\parallel=\mathbf{k}'_\parallel+\mathbf{q}_\parallel-\mathbf{k}_\parallel$. The singlet term acts as source to the correlations and leads to the build-up of correlations as soon as carriers and polarization are present.

In order to determine the full dynamics of the coherent correlations, one has to set up the equations of motion for the carrier-carrier correlations as well as for the true excitons. The numerical evaluation of the resulting set of equations is computationally very demanding and exceeds current computer powers. As a consequence, simplifications are needed that are computationally feasible but keep the essence of the carrier-scattering processes. We therefore review the approximations performed in Ref. [43].

We assume a weak probe pulse and a sufficiently long time delay between pump and probe such that it is a good approximation to assume that the carriers are close to thermal equilibrium. In this limit, the pump pulse has already decayed and does not directly influence the system at the probe time. Therefore, we may describe the carriers via quasi-stationary Fermi-Dirac distributions for a given carrier temperature and density such that we can omit the carrier dynamics (3.13) and (3.14). Different pump pulses enter the description via different carrier densities and temperatures.

Additionally, at elevated carrier temperatures and densities, we can assume that carrier-carrier correlations as well as the true exciton correlations are minor corrections and may be neglected as well [18]. As a consequence, the term $\left[D^{\mathbf{q}_\parallel,\mathbf{k}'_\parallel,\mathbf{k}_\parallel}_{\nu,\lambda,\lambda,\bar{\nu}}\right]_{\text{inc}}$ in Eq. (3.15) does not contribute. We can omit the coherent correlations $\left[D^{\mathbf{q}_\parallel,\mathbf{k}'_\parallel,\mathbf{k}_\parallel}_{\nu,\lambda,\lambda,\bar{\nu}}\right]_{\text{coh}}$ assuming that their dephasing is on a faster time scale than it takes to build up other quasi-particles.

The triplet contributions $\left[c^{\mathbf{q}_\parallel,\mathbf{k}'_\parallel,\mathbf{k}_\parallel}_{\nu,\lambda,\lambda,\bar{\nu}}\right]_{\text{T}}$ introduce dephasing, screening and energy renormalization effects to the correlation (3.15). The energy renormalizations in the correlation equation affect the absorption only minimally and can be neglected. Screening effects are included in our model by replacing the unscreened Coulomb-matrix elements in the singlet contribution $S^{\mathbf{q}_\parallel,\mathbf{k}'_\parallel,\mathbf{k}_\parallel}_{\nu,\lambda,\lambda,\bar{\nu}}$ by its screened counterparts. To model screening, we use the static Lindhardt approximation [31, 35]:

$$W_{\mathbf{k}_\parallel}=\frac{V_{\mathbf{k}_\parallel}}{1-V_{\mathbf{k}_\parallel}L_{\mathbf{k}_\parallel}} \qquad L_{\mathbf{k}_\parallel}=\sum_{\mathbf{k}'_\parallel,\alpha=e,h}\frac{f^\alpha_{\mathbf{k}'_\parallel-\mathbf{k}_\parallel}-f^\alpha_{\mathbf{k}'_\parallel}}{\epsilon^\alpha_{\mathbf{k}'_\parallel-\mathbf{k}_\parallel}-\epsilon^\alpha_{\mathbf{k}'_\parallel}}\,. \tag{3.18}$$

The dephasing of the correlation is modeled by applying a density-dependent dephasing constant $\left[c^{\mathbf{q}_\parallel,\mathbf{k}'_\parallel,\mathbf{k}_\parallel}_{\nu,\lambda,\lambda,\bar{\nu}}\right]_T\Big|_{\text{dephasing}} \approx -i\delta c^{\mathbf{q}_\parallel,\mathbf{k}'_\parallel,\mathbf{k}_\parallel}_{\nu,\lambda,\lambda,\bar{\nu}}$. Inserting all approximations for Eq. (3.15), we are left with

$$i\hbar\frac{\partial}{\partial t}c^{\mathbf{q}_\parallel,\mathbf{k}'_\parallel,\mathbf{k}_\parallel}_{\nu,\lambda,\lambda,\bar{\nu}} = \left(\varepsilon^{\bar{\nu}}_{\mathbf{k}_\parallel-\mathbf{q}_\parallel}+\varepsilon^{\lambda}_{\mathbf{k}'_\parallel+\mathbf{q}_\parallel}-\varepsilon^{\lambda}_{\mathbf{k}'_\parallel}-\varepsilon^{\nu}_{\mathbf{k}_\parallel}-i\delta\right)c^{\mathbf{q}_\parallel,\mathbf{k}'_\parallel,\mathbf{k}_\parallel}_{\nu,\lambda,\lambda,\bar{\nu}}+S^{\mathbf{q}_\parallel,\mathbf{k}'_\parallel,\mathbf{k}_\parallel}_{\nu,\lambda,\lambda,\bar{\nu}}\,, \tag{3.19}$$

where the single-particle-source term $S^{\mathbf{q}_\parallel,\mathbf{k}'_\parallel,\mathbf{k}_\parallel}_{\nu,\lambda,\lambda,\bar{\nu}}$ now contains the screened Coulomb-matrix element in static Lindhardt approximation.

We can now perform a Markov approximation (App. B) and formally solve Eq. (3.19). In the resulting equation, the energy denominator has the Lorentzian form $i/(E+i\delta)$ and leads to real and imaginary contributions where the imaginary contributions of the terms correspond to the principle value of the energy denominator. The real part of the Lorentzian describes the singular $\delta(E)$-contribution that is additionally broadened by the dephasing constant $i\delta$. In the limit $i\delta \mapsto 0$, the principle value vanishes such that the Lorentzian is determined by the $\delta(E)$ part. For finite broadenings $i\delta$, the principle value is also finite and cannot be neglected. However, the summations over $\mathbf{k}'_\parallel$ and $\mathbf{q}_\parallel$ in Eq. (3.7) lead to the cancellation of most contributions from the principle value due to its odd symmetry with respect to the energy singularities. Thus, we will neglect the principle value in our calculations. We are left with the real part of the Lorentzian such that the closed expression for the scattering reads

$$\begin{aligned}
&\sum_{\lambda,\mathbf{k}'_\parallel,\mathbf{q}_\parallel} V_{\mathbf{q}_\parallel}\left[c^{\mathbf{q}_\parallel,\mathbf{k}'_\parallel,\mathbf{k}_\parallel}_{v,\lambda,\lambda,c}-\left(c^{\mathbf{q}_\parallel,\mathbf{k}'_\parallel,\mathbf{k}_\parallel}_{c,\lambda,\lambda,v}\right)^\star\right]\Big|_{\text{2ndBorn}} = \\
&\quad i\sum_{\substack{\mathbf{q}_\parallel\neq\mathbf{k}_\parallel\\ \mathbf{k}'_\parallel\neq\mathbf{q}_\parallel}}\mathrm{Re}\left(\frac{\mathrm{i}V_{\mathbf{k}_\parallel-\mathbf{q}_\parallel}}{\hbar\omega_\mathrm{S}-(\varepsilon^\mathrm{e}_{\mathbf{k}_\parallel}-\varepsilon^\mathrm{h}_{\mathbf{j}_\parallel}+\varepsilon^\mathrm{h}_{\mathbf{k}'_\parallel}+\varepsilon^\mathrm{h}_{\mathbf{q}_\parallel})+\mathrm{i}\delta}\right)\times \\
&\qquad\Big\{W_{\mathbf{k}_\parallel-\mathbf{q}_\parallel}\left[\bar{f}^h_{\mathbf{k}'_\parallel}f^h_{\mathbf{j}_\parallel}\bar{f}^e_{\mathbf{k}_\parallel}+f^h_{\mathbf{k}'_\parallel}\bar{f}^h_{\mathbf{j}_\parallel}f^e_{\mathbf{k}_\parallel}\right]p_{\mathbf{q}_\parallel} \\
&\qquad\quad-(W_{\mathbf{k}_\parallel-\mathbf{q}_\parallel}-W_{\mathbf{k}_\parallel-\mathbf{k}'_\parallel})\left[\bar{f}^h_{\mathbf{j}_\parallel}f^h_{\mathbf{k}'_\parallel}f^h_{\mathbf{q}_\parallel}+f^h_{\mathbf{j}_\parallel}\bar{f}^h_{\mathbf{k}'_\parallel}\bar{f}^h_{\mathbf{q}_\parallel}\right]p_{\mathbf{k}_\parallel} \\
&\qquad\quad-W_{\mathbf{k}_\parallel-\mathbf{k}'_\parallel}\left[\bar{f}^h_{\mathbf{q}_\parallel}f^h_{\mathbf{j}_\parallel}\bar{f}^e_{\mathbf{k}_\parallel}+f^h_{\mathbf{q}_\parallel}\bar{f}^h_{\mathbf{j}_\parallel}f^e_{\mathbf{k}_\parallel}\right]p_{\mathbf{k}'_\parallel}\Big\} \\
+\quad i\sum_{\substack{\mathbf{q}_\parallel\neq\mathbf{k}_\parallel\\ \mathbf{k}'_\parallel\neq\mathbf{q}_\parallel}}&\mathrm{Re}\left(\frac{\mathrm{i}V_{\mathbf{k}_\parallel-\mathbf{q}_\parallel}}{\hbar\omega_\mathrm{S}+(-\varepsilon^\mathrm{h}_{\mathbf{k}_\parallel}+\varepsilon^\mathrm{e}_{\mathbf{j}_\parallel}-\varepsilon^\mathrm{e}_{\mathbf{k}'_\parallel}-\varepsilon^\mathrm{e}_{\mathbf{q}_\parallel})+\mathrm{i}\delta}\right)\times \\
&\qquad\Big\{W_{\mathbf{k}_\parallel-\mathbf{q}_\parallel}\left[f^e_{\mathbf{k}'_\parallel}\bar{f}^e_{\mathbf{j}_\parallel}f^h_{\mathbf{k}_\parallel}+\bar{f}^e_{\mathbf{k}'_\parallel}f^e_{\mathbf{j}_\parallel}\bar{f}^h_{\mathbf{k}_\parallel}\right]p_{\mathbf{k}_\parallel} \\
&\qquad\quad-(W_{\mathbf{k}_\parallel-\mathbf{q}_\parallel}-W_{\mathbf{k}_\parallel-\mathbf{k}'_\parallel})\left[f^e_{\mathbf{j}_\parallel}\bar{f}^e_{\mathbf{k}'_\parallel}\bar{f}^e_{\mathbf{q}_\parallel}+\bar{f}^e_{\mathbf{j}_\parallel}f^e_{\mathbf{k}'_\parallel}f^e_{\mathbf{q}_\parallel}\right]p_{\mathbf{k}_\parallel} \\
&\qquad\quad-W_{\mathbf{k}_\parallel-\mathbf{k}'_\parallel}\left[f^e_{\mathbf{q}_\parallel}\bar{f}^e_{\mathbf{j}_\parallel}f^h_{\mathbf{k}_\parallel}+\bar{f}^e_{\mathbf{q}_\parallel}f^e_{\mathbf{j}_\parallel}\bar{f}^h_{\mathbf{k}_\parallel}\right]p_{\mathbf{k}'_\parallel}\Big\}
\end{aligned}$$

$$- \quad \left(\mathbf{q}_\parallel \leftrightarrow \mathbf{k}_\parallel\right) . \tag{3.20}$$

Equation (3.20) yields the steady state solution for the correlation contributions in the polarization equation (3.7). We can express this solution via a complex and $\mathbf{k}_\parallel$-dependent scattering term $\sum_{\mathbf{k}'_\parallel} \Gamma_{\mathbf{k}_\parallel,\mathbf{k}'_\parallel} p_{\mathbf{k}'_\parallel}$ such the polarization dynamics (3.7) reads

$$\begin{aligned} i\hbar\frac{\partial}{\partial t} p_{\mathbf{k}_\parallel} &= \tilde{\epsilon}_{\mathbf{k}_\parallel} p_{\mathbf{k}_\parallel} + \sum_{\mathbf{k}'_\parallel} \Gamma_{\mathbf{k}_\parallel,\mathbf{k}'_\parallel} p_{\mathbf{k}'_\parallel} \\ &- \left(1 - f^e_{\mathbf{k}_\parallel} - f^h_{\mathbf{k}_\parallel}\right) \left[\langle E_0\rangle + \sum_{\mathbf{k}'_\parallel} V_{\mathbf{k}'_\parallel - \mathbf{k}_\parallel} p_{\mathbf{k}'_\parallel}\right] . \end{aligned} \tag{3.21}$$

The scattering term introduces additional band-gap renormalizations that compensate Hartree-Fock shifts at elevated carrier densities as well as density dependent dephasing that lead to a broadening of the exciton resonance. Similar expressions for the carrier scattering without the frequency dependence of the energy denominator have been derived in Refs. [32, 35, 43, 44].

3.4. Scattering in indirect semiconductors

So far, we have concentrated on the description of the carrier scattering in direct GaAs-type semiconductors. Now, we want to extend our model such that we can also describe indirect semiconductors. As an example, we choose Ge as the QW material. The conduction band of Ge has its absolute energy minimum at the L-point while it shows a local minimum at the Γ-point. The shape of the valence band is similar to that of GaAs. A schematic picture of the band structure of Ge and GaAs is shown in Fig. 3.1.

Due to the conduction-band minimum at the L-point, the electrons in Ge that are optically excited close to the direct band gap experience a fast scattering from the Γ-point to the L-point. In contrast to the electrons, the holes scatter to the Γ-point. Thus, we have to take into account L-point and Γ-point carrier-contributions. For simplicity, we assume the conduction band to be parabolic in the vicinity of the two relevant points with effective masses m_e and m_L for Γ-point and L-point, respectively.

For optical dipole transitions, momentum conservation of the parallel component of the wave vectors applies. Therefore, the absorption of a photon with momentum $\hbar\mathbf{q}_\parallel$ directly corresponds to a change of the carrier momentum of the excited electron from $\hbar\mathbf{k}_\parallel \to \hbar(\mathbf{k}_\parallel + \mathbf{q}_\parallel)$. Since the photon momenta for optical transitions in Ge and GaAs are small compared to the relevant electron momenta and we assume excitations close to the direct band gap, only polarizations that are in the vicinity of the Γ-point have to be evaluated. As a consequence, the electron wave-vectors in the phase-space-filling factor as well as those in the single-particle energies in Eq. (3.7) have to be close to the Γ-point. In the Coulomb sums contributing to the renormalized Rabi-frequency and the energy renormalizations (3.10), we can neglect such terms where the wave vector $\mathbf{k}'_\parallel$ is close to the L-point. In these cases, the argument of the Coulomb-matrix element

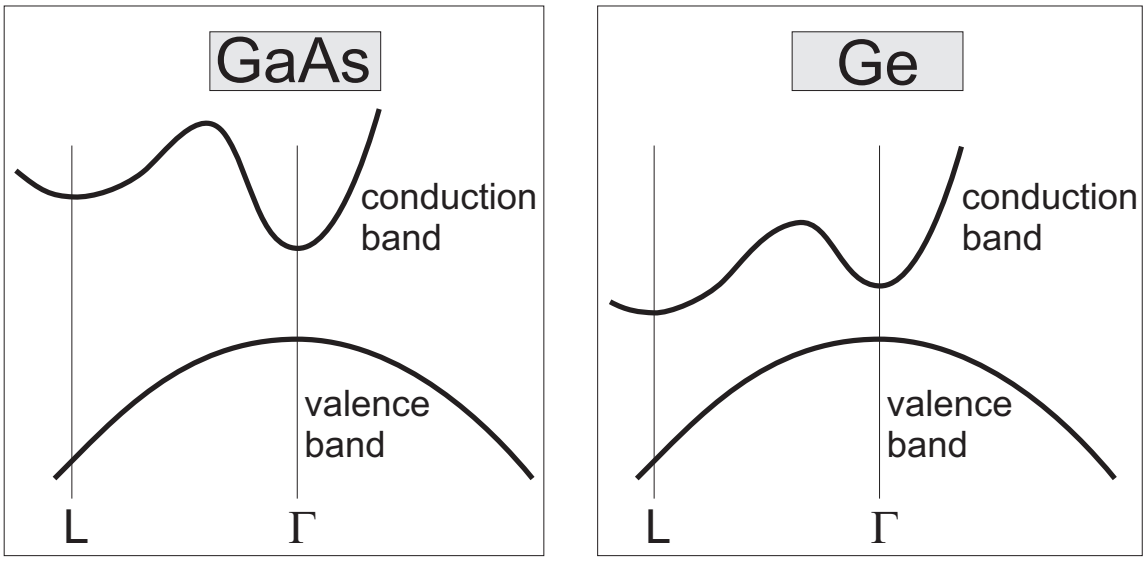

Figure 3.1.: *Sketch of the band structure of GaAs (left) and Ge (right).* GaAs shows a direct gap at the Γ-point while Ge exhibits the minimum of the first conduction band in the L-point and is therefore indirect.

becomes very large and consequently the Coulomb-matrix element itself is vanishingly small. The wave vector $\mathbf{q}_\parallel$ corresponds to photon momenta and thus is small. Hence, the only place where electron momenta close to the L-point enter the calculation is the sum over $\mathbf{k}'_\parallel$ in the scattering contributions.

In order to trace the different electron contributions, we divide $\sum_{\lambda,\mathbf{k}'_\parallel,\mathbf{q}_\parallel}$ in Eq. (3.7) into $\sum_{\lambda,\tilde{\mathbf{k}}_\parallel,\mathbf{q}_\parallel}$ and $\sum_{\lambda,\mathbf{l}_\parallel,\mathbf{q}_\parallel}$, where $\mathbf{l}_\parallel$ includes all electron momenta in the vicinity of the L-point while *vparak* contains the other carrier momenta that are close to the Γ-point.

The contribution $\sum_{\lambda,\tilde{\mathbf{k}}_\parallel,\mathbf{q}_\parallel}$ is treated on a 2nd-Born level as discussed in Sec. 3.3. For consistency reasons, we treat the L-point electrons on the same level of approximation as the electrons at the Γ-point. Consequently, we set up the equation of motion for $\sum_{\lambda,\mathbf{l}_\parallel,\mathbf{q}_\parallel} c^{\mathbf{q}_\parallel,\mathbf{l}_\parallel,\mathbf{k}_\parallel}_{v,\lambda,\lambda,c}$ in singlet-doublet approximation and perform the same steps as for the Γ-point electrons. Executing these steps, we keep in mind that there are no holes at the L-point and that Coulomb-matrix elements with arguments that consist of differences between L-point and Γ-point wave-vectors are vanishingly small. The result of this procedure reads

$$\sum_{\mathbf{l}_\parallel,\mathbf{q}_\parallel} V_{\mathbf{q}_\parallel} \left[c^{\mathbf{q}_\parallel,\mathbf{l}_\parallel,\mathbf{k}_\parallel}_{v,c,c,c} - \left(c^{\mathbf{q}_\parallel,\mathbf{l}_\parallel,\mathbf{k}_\parallel}_{c,c,c,v} \right)^\star \right] \Bigg|_{2ndBorn} =$$

$$i \sum_{\substack{\mathbf{q}_\parallel \neq \mathbf{k}_\parallel \\ \mathbf{l}'_\parallel \neq \mathbf{q}_\parallel}} \mathrm{Re} \left(\frac{i V_{\mathbf{k}_\parallel - \mathbf{q}_\parallel}}{\hbar\omega_\mathrm{S} + (-\varepsilon^h_{\mathbf{k}_\parallel} + \varepsilon^e_{\tilde{\mathbf{j}}_\parallel} - \varepsilon^e_{\mathbf{l}'_\parallel} - \varepsilon^e_{\mathbf{q}_\parallel}) + i\delta} \right) \times$$

$$\left\{\tilde{W}_{\mathbf{k}_\parallel-\mathbf{q}_\parallel}\left[f^e_{\mathbf{l}_\parallel}\bar{f}^e_{\tilde{\mathbf{j}}_\parallel}f^h_{\mathbf{k}_\parallel}+\bar{f}^e_{\mathbf{l}_\parallel}f^e_{\tilde{\mathbf{j}}_\parallel}\bar{f}^h_{\mathbf{k}_\parallel}\right]p_{\mathbf{k}_\parallel}-\tilde{W}_{\mathbf{k}_\parallel-\mathbf{q}_\parallel}\left[f^e_{\mathbf{j}_\parallel}\bar{f}^e_{\mathbf{l}_\parallel}\bar{f}^e_{\mathbf{q}_\parallel}+\bar{f}^e_{\tilde{\mathbf{j}}_\parallel}f^e_{\mathbf{l}_\parallel}f^e_{\mathbf{q}_\parallel}\right]p_{\mathbf{k}_\parallel}\right\}$$
$$-\left(\mathbf{q}_\parallel\leftrightarrow\mathbf{k}_\parallel\right), \tag{3.22}$$

where $\tilde{\mathbf{j}}=\mathbf{l}_\parallel+\mathbf{q}_\parallel-\mathbf{k}_{\parallel\parallel}$ is of the same order of magnitude as $\mathbf{l}_\parallel$ and, thus, corresponds to wave vectors in the vicinity of the L-point. For the computation of the Fermi distributions for the L-point electrons, the four-fold degeneracy of the conduction band is taken into account.

Similar to the expression in the scattering term, we can separate the Lindhardt sum (3.18) into the sums $\sum_{\mathbf{l}'_\parallel}$ and $\sum_{\mathbf{k}'_\parallel}$ that contain electron momenta close to the L-point and the Γ-point, respectively. The Lindhardt screened Coulomb-matrix element in Eq. (3.22) is given by

$$\tilde{W}_{\mathbf{k}_\parallel}=\frac{V_{\mathbf{k}_\parallel}}{1-V_{\mathbf{k}_\parallel}\tilde{L}_{\mathbf{k}_\parallel}}\qquad\qquad \tilde{L}_{\mathbf{k}_\parallel}=\sum_{\mathbf{k}'_\parallel,\alpha=e,h}\frac{f^\alpha_{\mathbf{k}'_\parallel-\mathbf{k}_\parallel}-f^\alpha_{\mathbf{k}'_\parallel}}{\epsilon^\alpha_{\mathbf{k}'_\parallel-\mathbf{k}_\parallel}-\epsilon^\alpha_{\mathbf{k}'_\parallel}}+\sum_{\mathbf{l}'_\parallel}\frac{f^e_{\mathbf{l}'_\parallel-\mathbf{k}_\parallel}-f^e_{\mathbf{l}'_\parallel}}{\epsilon^e_{\mathbf{l}'_\parallel-\mathbf{k}_\parallel}-\epsilon^e_{\mathbf{l}'_\parallel}}. \tag{3.23}$$

3.5. Excitation induced dephasing

Before we start investigating the scattering effects in Ge QWs, we analyze how different carrier densities influence the optical response of a direct semiconductor QW. For simplicity, we study a GaAs QW embedded inside a structure that has the same refractive index as the QW itself such that no reflections inside the sample structure occur. We assume that the pump pulse excites the carriers with an energy slightly above the fundamental band gap (Fig. 3.2a). Due to the direct band gap of GaAs, the electrons and holes scatter toward the Γ-point on a fast femtosecond (fs) time scale (Fig. 3.2b). Therefore, we can assume that only carrier populations at the Γ-point are present at the time when the probe pulse tests the system such that Eq. (3.22) can be omitted and the screening is described by Eq. (3.18). For the numerical evaluations, we use a lattice temperature of $T = 77$ K. A phenomenological background dephasing of $\gamma_{bg} = 0.05E_B$ is added to the dephasing introduced by the carrier-carrier scattering, simulating the carrier-phonon scattering that is not explicitly treated in this work.

In Fig. 3.3a, we present the linear absorption spectra for a sequence of carrier densities corresponding to different pump intensities. We analyze the carrier densities 1×10^9 cm^{-2} (red line), 2×10^{10} cm^{-2} (blue line), 5×10^{10} cm^{-2} (green line), 1×10^{11} cm^{-2} (magenta line), and 2×10^{11} cm^{-2} (black line). The corresponding sums of electron and hole distributions are shown in Fig. 3.3b using the same color code as in Fig. 3.3a.

At the lowest carrier density, we find a well pronounced 1s-exciton resonance and a weak 2s-resonance. The 2s resonance is clearly stronger broadened than the 1s resonance. From pure radiative decay of the polarization, we would have expected the opposite effect, as the radiative lifetime of 2s excitons is longer than that of 1s excitons. As a consequence, the purely radiative broadening of the 2s resonance is smaller than the radiative broadening of the 1s resonance [31]. The strong broadening of the 2s and higher resonances observed in Fig. 3.3a, is a typical signature of the carrier scattering.

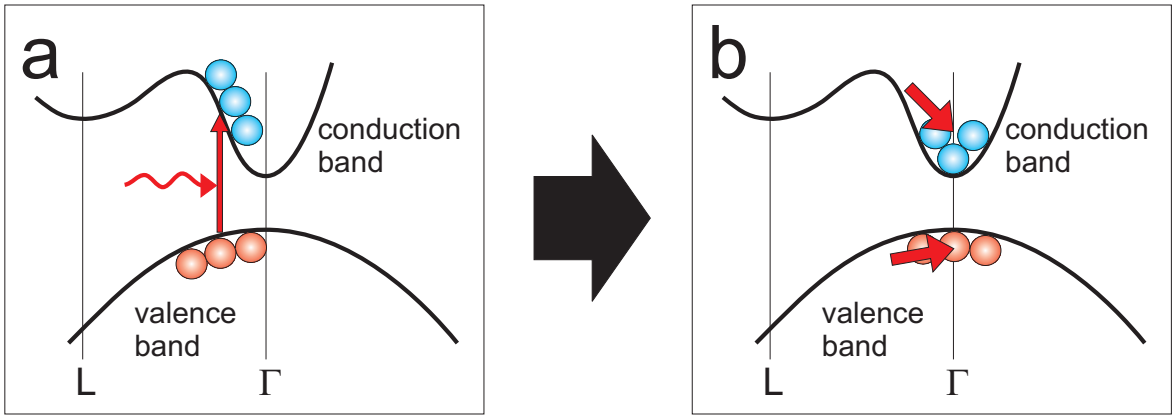

Figure 3.2.: *Sketch of the excitation and subsequent scattering toward the Γ-point in GaAs: Frame a:* A laser pulse optically excites a GaAs QW such that electrons (blue dots) are created in the conduction band and holes (red dots) are created in the valence band. *Frame b:* Fast scattering processes on a fs time-scale relax the carriers toward the Γ-point.

The peak width of the 1s resonance at a carrier density of 1×10^9 cm^{-2} is mainly determined by the homogeneous broadening that we have introduced due to the electron-phonon scattering whereas the 2s resonance is broadened by carrier scattering. For increasing carrier densities, the exciton resonances show stronger broadening indicating an increase of the carrier-scattering strength. The scattering leads to the bleaching of the 2s resonance at already 1×10^{10} cm^{-2}. For even higher carrier densities, phase-space filling effects and the increasing dephasing due to carrier scattering eventually lead to the bleaching of the 1s resonance. Thus, at 1×10^{11} cm^{-2} the 1s resonance shows a HWHM of 1.4 meV and at 2×10^{11} cm^{-2} no pronounced 1s resonance is visible any more.

Calculations that treat the carrier scattering on a lower theory level, e.g. Hartree-Fock calculations, exhibit the same peak broadening for all resonances. On top, these calculations lead to pronounced shifts of the 1s resonance for increasing carrier densities [32]. These shifts cannot be observed in experiments. They originate from the band-gap renormalizations (3.10) and phase-space filling effects that cannot be compensated in Hartree-Fock calculations.

In our 2nd-Born treatment of the carrier scattering, the scattering shows density-dependent dephasing and additional band-gap renormalizations that compensate the Hartree-Fock shifts. Consequently in GaAs QWs, the 1s resonance remains stable when the carrier density is increased. This behavior is in excellent agreement with experiments [43].

In frames Fig. 3.3c and 3.3d, we show what happens if the carrier density is increased further. The curves for 2×10^{11} cm^{-2} (black lines) are replotted to these two frames and graphs for the carrier densities 3×10^{11} cm^{-2} (red lines), 4×10^{11} cm^{-2} (blue lines), and 5×10^{11} cm^{-2} (green lines) are added.

The sum of electron and hole distributions is close to unity for 3×10^{11} cm^{-2}. Conse-

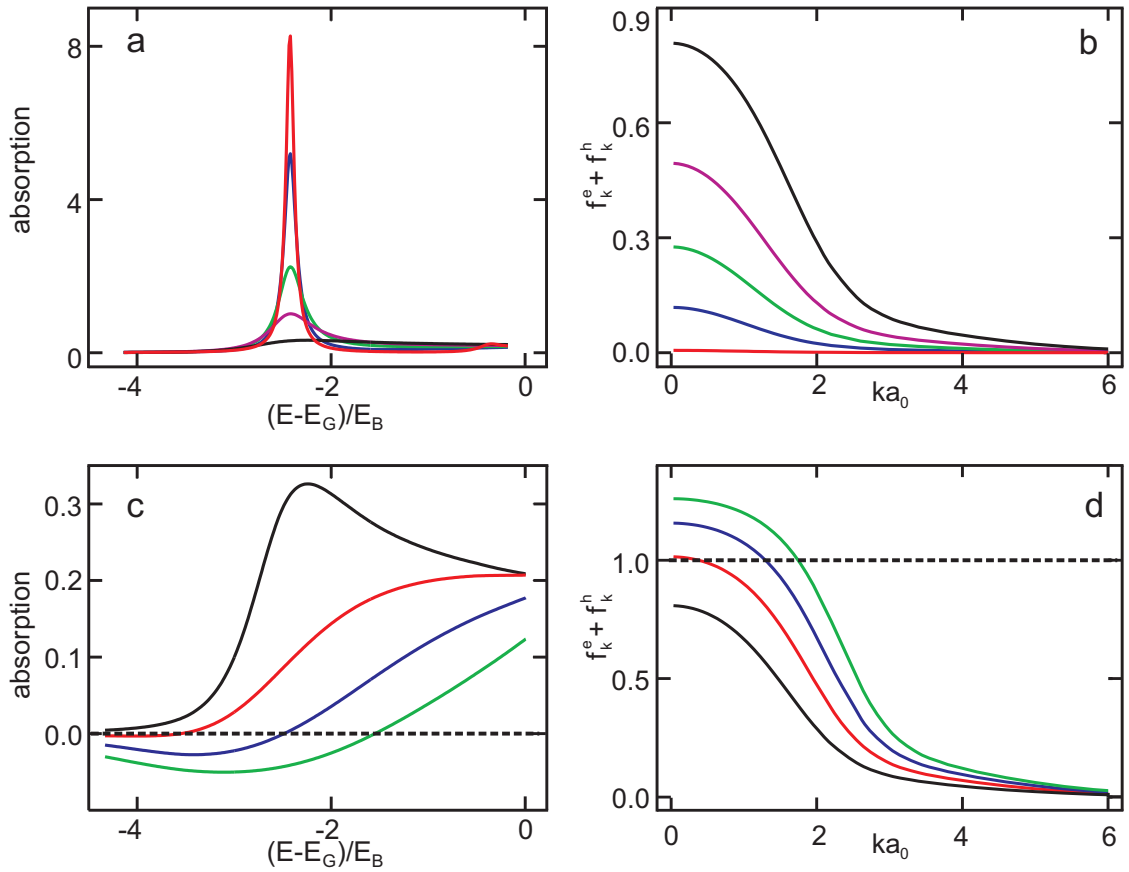

Figure 3.3.: *Excitation induced dephasing (frames a and b) and gain (frames c and d):* In frame a and c, the absorption spectra for different carrier densities are shown. We depict in frame a the densities 1×10^9 cm^{-2} (red line), 2×10^{10} cm^{-2} (blue line), 5×10^{10} cm^{-2} (green line) and 1×10^{11} cm^{-2} (magenta line). The black lines in frames a and c correspond to 2×10^{11} cm^{-2}. The other densities shown in frame c are 3×10^{11} cm^{-2} (red line), 4×10^{11} cm^{-2} (blue line), and 5×10^{11} cm^{-2} (green line). The sum of electron and hole distributions corresponding to the respective densities is depicted in frames b and d. As guide for the eye zero in frame c and unity in frame d is marked by a dashed line. All calculations have been performed at $T = 77\ K$ and a phenomenological background dephasing constant of $\gamma_{bg} = 0.05\ E_B$ due to electron-phonon interaction has been used.

quently, the corresponding phase-space-filling factor is close to zero such that the exciton resonances become fully bleached and bound exciton states cease to exist. This behavior is also known as the Mott transition [49, 50]. Increasing the carrier densities to even higher values, we recover negative phase-space fillings and consequently negative absorption indicating optical gain [6, 51].

3.6. Absorption in indirect semiconductors

In the previous section, we have investigated the absorption in a direct GaAs-type QW. We have found that direct semiconductors exhibit optical gain for sufficiently large carrier densities due to a population inversion at the Γ-point. For low carrier densities the 1s-peak position is independent of the carrier density.

In contrast to GaAs, Ge is an indirect semiconductor with the absolute minimum of the conduction band located at the L-point. Therefore, the electrons in Ge undergo a relaxation toward the L-point even when the excitation process takes place energetically in the vicinity of the direct band gap at the Γ-point. For sufficiently long times after the pump, the majority of the electrons will be located at the L-point while the holes have relaxed to the Γ-point (see Figs. 3.4a and 3.4c). Thus, electrons and holes are separated in k-space such that population inversion and gain cannot be obtained. This feature makes it practically impossible to use Ge as an optically active material in laser structures or amplifiers.

However, shortly after the excitation when the relaxation process toward the L-point is not yet completed, a certain amount of electrons is still located at the Γ-point such that for strong excitation conditions population inversion could be reached for some fs (Fig. 3.4b). Thus, in this section, we will investigate how the absorption develops shortly after the excitation has taken place. In this context, we show that for strong excitation conditions Ge QWs may exhibit transient gain for time scales on the order of 200 fs.

As a starting point for this investigation, we briefly discuss an experiment where the time-resolved optical response of a Si-Ge sample is measured. The sample consists of 50 Ge QWs that are embedded into a Si substrate. The sample is excited by a very strong (about 1×10^{18} photons cm^{-2}) 80 fs-pulse that is energetically centered at the heavy-hole continuum at 0.905 eV, about 30 meV above the fundamental band edge. The excitation intensity corresponds to more than 100 times the intensity needed to create gain in GaAs. As a consequence of the strong excitation, one obtains Pauli blocking effects such that only a relative small fraction of the photons is converted into electron populations.

The measured absorption spectra in the vicinity of the direct band-gap for different time delays after the exciting pump pulse are shown in Fig. 3.5b. The black line corresponds to the linear absorption in the zero-density limit and shows a pronounced exciton resonance at 878 meV.

During and shortly after the excitation, the resonance is bleached and the sample shows gain for about 200 fs. The spectrum for the maximum gain is shown as a red line. After the maximum gain is reached, the exciton resonance starts to recover as is visible from the light blue and green curves that show the absorption at 0.05 and 0.15 ps after the gain peaking. Several hundred fs after the excitation, the carrier distributions reach a steady state and thus the absorption remains unchanged for many ns. The dark blue curve shows the corresponding steady-state spectrum.

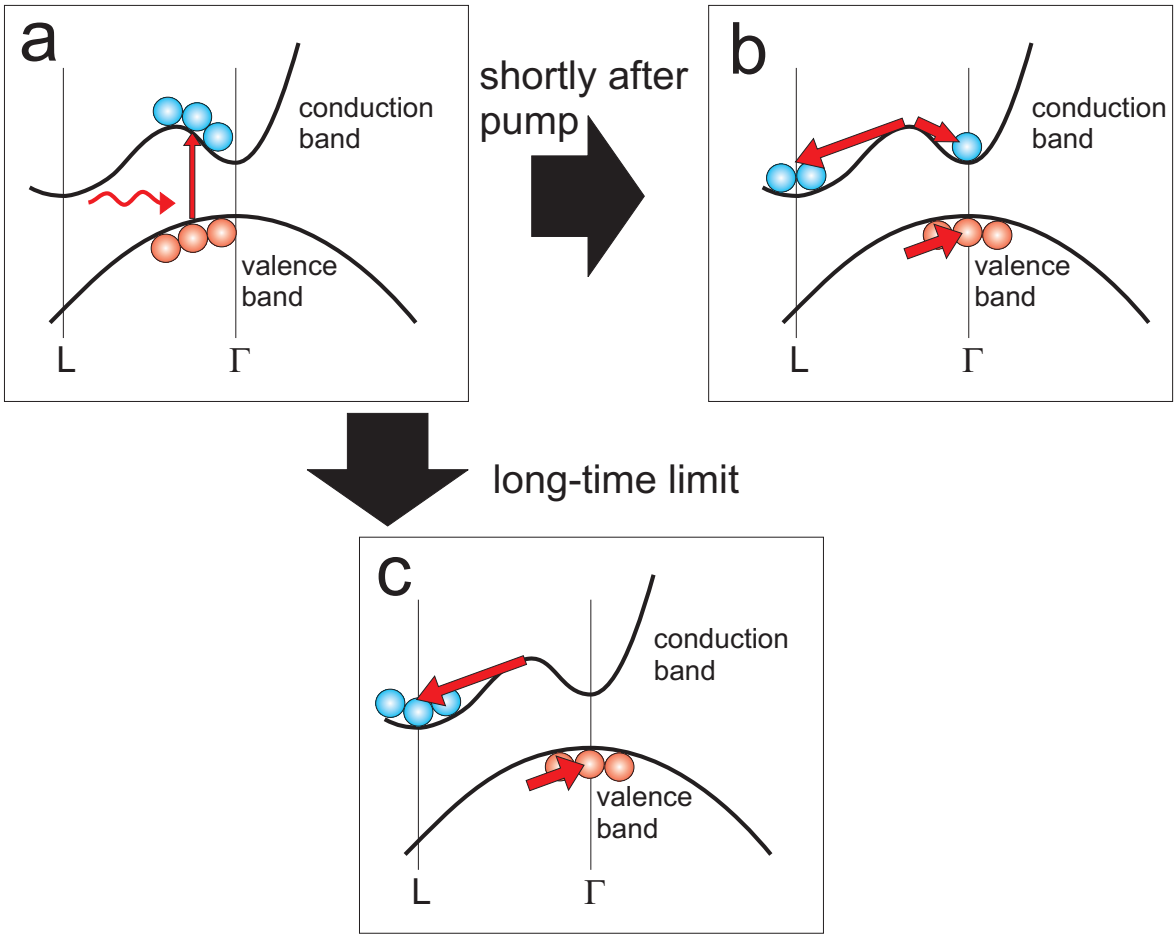

Figure 3.4.: *Sketch of the excitation and subsequent scattering in Ge: Frame a:* A laser pulse optically excites a Ge QW such that electrons (blue dots) are created in the conduction band and holes (red dots) are created in the valence band. *Frame b:* Shortly after the pump has excited the system, electron populations may be found at the Γ-point and L-point. *Frame c:* In the long time limit, all electrons have relaxed to the L-point and holes to the Γ-point such that electrons and holes are separated in k-space.

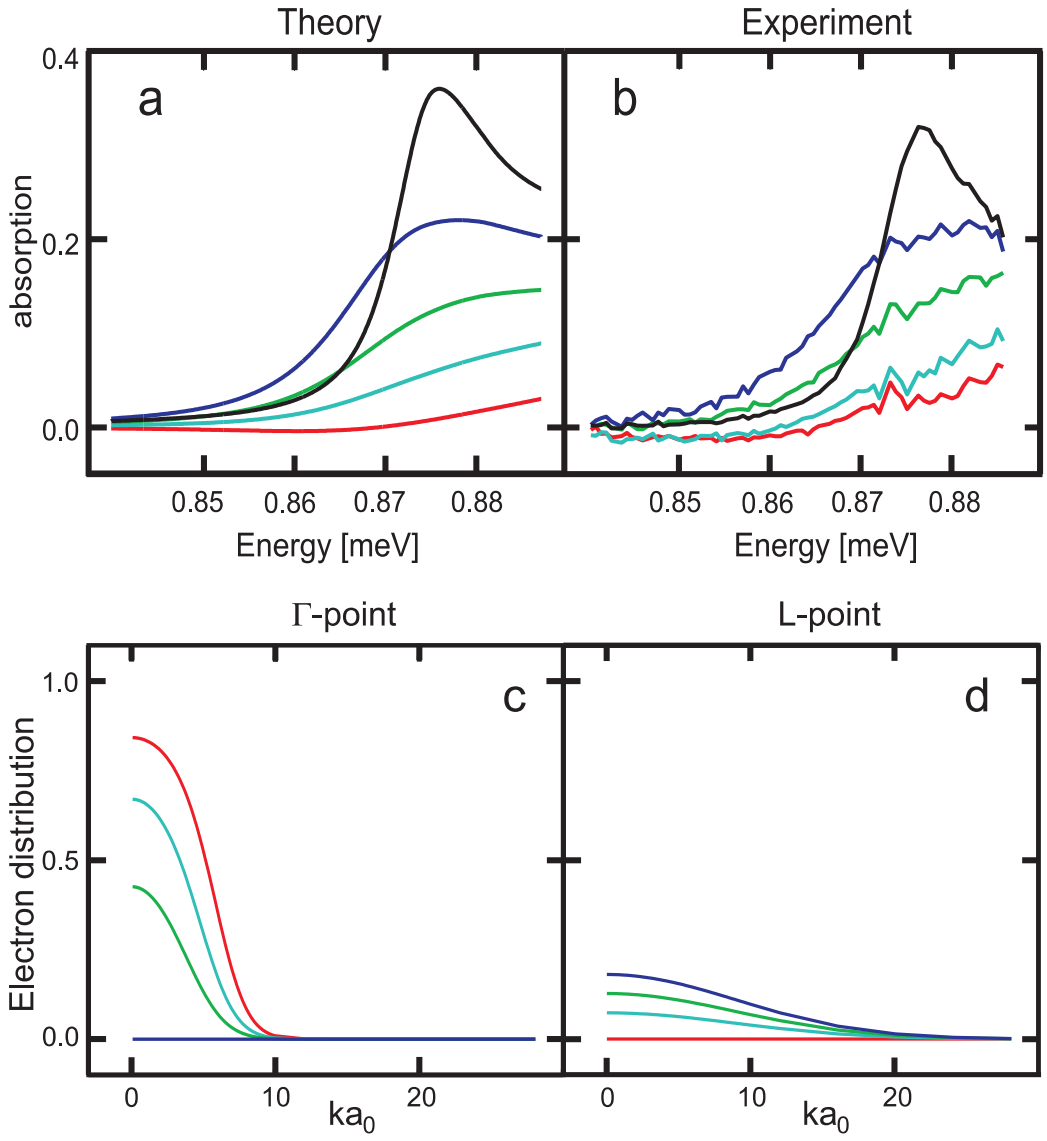

Figure 3.5.: *Absorption in Ge; experiment vs. theory:* Frame a shows the numerically simulated absorption in Ge for different electron fractions at the L-point. The different curves correspond to 0% (red),40% (light blue),70% (green) and 100% L-point fraction (dark blue). The calculations have been performed for $T = 300K$ and a total carrier density of $8 \times 10^{11} cm^{-2}$. Frame b shows the absorption spectra measured from a Ge QW for different time delays after the pump pulse. The curves correspond to time delays of 0.0 ps (red), 0.05 ps (light blue), 0.15 ps (green) and 1.6 ps (dark blue) time delay after the maximum gain. In both frames the black line shows the linear absorption in the zero density limit. In frame c (d), the corresponding electron distributions at the Γ-point (L-point) are plotted. Note that the L-point is four-fold degenerate such that the electron distributions at the L-point have to be multiplied by a factor of four.

In order to explain these observations, we concentrate on the pure QW-emission process and neglect reflections inside the sample. We treat the carrier scattering in 2nd-Born approximation according to Eqs. (3.20) and (3.22).

To illustrate that the theory describes the basic features of the scattering in Fig. 3.5a, we show the numerical results in comparison to the experimental measurements in frame b. For our numerical simulations, we use $T = 300$ K and a total electron density of 8×10^{12} cm^{-2} that is divided into an L-point fraction and a Γ-point fraction. The black line depicts the linear absorption of the Ge QW in the zero-density limit.

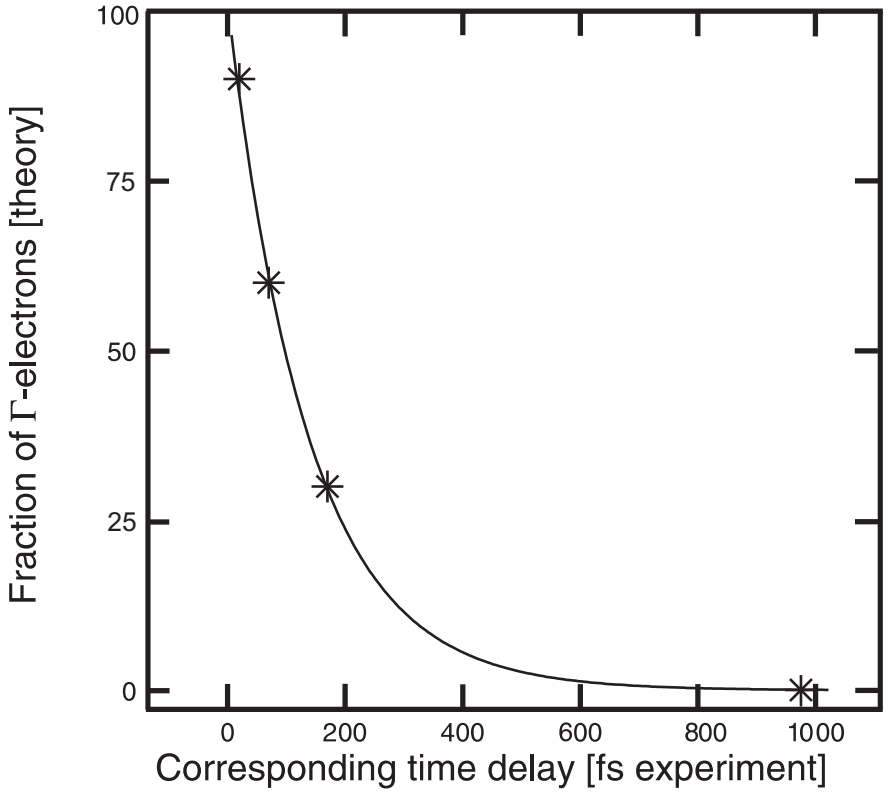

Figure 3.6.: Γ-*to-L scattering:* Corresponding Γ-point fractions and delay times derived by a peak shape comparison between experiment and theory. The solid line shows an exponential fit where the resulting decay time is $\tau = 140$ fs.

Since the laser pulse excites carriers in the vicinity of the Γ-point only, we assume that in the beginning all electrons are concentrated there. The red curve shows the corresponding numerically evaluated optical response. As time proceeds, the electrons are scattered from the Γ-point to the L-point. Thus, the electron population at the Γ-point decreases. As a consequence, the phase-space-filling factor grows as time goes on. The gain vanishes as soon as the value of the phase-space filling at $\mathbf{k}_{\parallel} = 0$ exceeds zero. For even larger L-point electron fraction, the exciton resonance recovers. The curves corresponding to fractions of 40% and 70% of the electrons at the L-point are shown as light blue and green lines, respectively.

In the long-time limit, all electrons have reached the L-point leaving an empty con-

duction band at the Γ-point. The dark blue line shows the corresponding absorption spectrum. If we compare the final spectrum to the linear absorption, we note that the exciton resonance has not fully recovered. This feature can be explained by two effects: a) The holes have remained at the Γ-point and thus contribute to the phase-space filling at all times leading to a partial resonance bleaching. b) Even at long times after the excitation, electrons at the L-point and holes still contribute to the carrier-scattering and lead to a dephasing of the exciton resonance.

The electron distributions corresponding to the different amount of electrons at the Γ-point and the L-point are shown in Figs. 3.5c and 3.5d, respectively. Note, that the L-point is four-fold degenerate such that the L-point distributions have to be multiplied by four to obtain the total amount of electrons in that point.

A peak-shape comparison between experimental and numerical absorption spectra allows us to relate the delay times between pump and probe pulses to the fractions of electrons at the Γ-point. The corresponding results can be found in Fig. 3.6 where we show the Γ-point fraction of the electrons (black stars) as a function of time delay. Additionally, we plot an exponential fit indicated as a black line. From the fit function we can determine a Γ-to-L-scattering time of $\tau = 140$ fs.

The Γ-to-L scattering-time is expected to be strongly dependent on the number of excited carriers. Generally, a larger amount of carriers should lead to a stronger carrier scattering such that the Γ-to-L scattering time becomes faster and the time for which gain can be observed becomes shorter. This effect speaks clearly against the application of Ge QWs as an amplifier material.

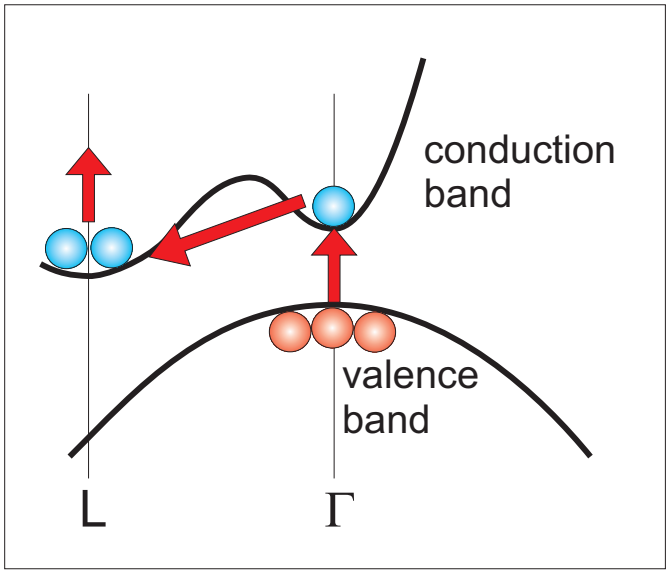

Figure 3.7.: *Absorption due to L-point electrons:* L-point electrons can contribute to the absorption and thus may inhibit optical gain.

In order to increase the timespan for which gain is observed, one could think of using continious-wave pumping such that electron populations at the Γ-point are always

present. Unfortunately, this concept does not work [52]. For long pump pulses, a significant amount of electrons scatters to the L-point while the excitation is still in progress. These L-point electrons can absorb photons from the pump pulse such that they are excited into continuum states of the substrate (Fig. 3.7). Thus, L-point electrons lead to a spectrally broad absorption signature in the optical response spectra. With increasing L-point electron population, this absorption becomes stronger such that the gain eventually vanishes, even when the excitation process is still in progress and electrons are present at the Γ-point. As a consequence, the duration for which gain is observed is limited to roughly the Γ-to-L scattering-time even for long pump pulses. If a Ge QW is positioned inside a cavity or a MQW system of Ge QWs is present, the electrons at the L-point may also act as absorbers for the photons that are emitted from the QWs due to the recombination processes. Thus, in such systems gain cannot be observed as soon as a sufficient electron distribution at the L-point is present. As a consequence, Ge QWs cannot be used as optically active region in laser structures.

4. Influence of the dielectric environment

So far, we have investigated the influence of carrier-carrier scattering on the absorption spectra of either direct or indirect semiconductors. In this analysis, we have neglected effects of the dielectric environment, which is often a good approximation when the dielectric environment is optically inactive and the investigated structure does not contain a cavity.

However, many realistic QW-samples are embedded inside a complicated dielectric environment. It may include e.g. cap layers to protect oxidation-sensitive regions of the sample from the air or AR-coatings that allow for minimal reflection at the air-sample surface. Other components may be used to reduce the strain between two neighboring layers of different materials resulting from their different lattice constants. Such components are, for example, superlattices and gradient-concentration layers that mediate between two materials via a concentration gradient of the neighboring materials. If an enhanced coupling between the light-field and the QW is desired, the structure may contain one DBR to form a VECSEL or even two DBRs in the case of a VCSEL.

All these different components lead to steps in the refractive-index profile and therefore to partial reflections inside the structure. As a consequence, the measured reflection and transmission from the complete heterostructure depend on the dielectric configuration. The spectra can for example show Fabry-Perot oscillations [53] or modifications of the exciton peak due to a changed radiative lifetime of excitations resulting from the modified coupling strength between the carriers and the light field [54–57].

In the regime of enhanced light-matter coupling that can be realized when the QW is placed inside a VCSEL, we may even obtain normal-mode splitting [32, 43]. Consequently, the dielectric environment can crucially change the reflection and transmission. Thus, if we are interested in these quantities and want to compare the numerical simulations of QW devices against the experimental results, we have to take into account the exact dielectric environment.

In the following section, we will briefly introduce a systematic transfer-matrix method that allows for computing the mode functions as well as the reflection and transmission through the sample as discussed in Ref. [37]. In Sec. 4.2, we show how to include the microscopic description of a QW in the coherent limit (see Chap. 3) into the transfer-matrix method. Finally, in Sec. 4.3, we compare the numerical results observed from the transfer-matrix method with experimental absorption spectra measured by a pump-probe experiment.

4.1. Treatment of the dielectric environment

Device components like superlattices, AR-coatings or cap-layers may be modeled via a stack of regions with spatially constant refractive index. As a suitable basis for computing the reflection and transmission at the boundaries, we choose the mode basis and defines the (counter-) propagating mode $U_{+\mathbf{q}}$ ($U_{-\mathbf{q}}$) which corresponds to a light pulse that originally propagates from the left (right) to the right (left) and which is partially reflected and transmitted at the boundaries of the dielectric structure. Within the regions of spatially constant refractive-index, Eq. (2.14) shows that the mode functions are plane waves describing light that propagates freely to either the left or the right.

To visualize this situation, we present in Fig. 4.1 a step-function refractive-index profile, indicated as the shaded area. The dashed (solid) line shows the (counter-) propagating mode. At the boundary, the light is split according to reflection R^- (R^+) and transmission T^- (T^+) coefficients corresponding to the light that arrives at the boundary from the left (right). In front of the boundary, the mode functions are consequently superpositions of the incoming and the reflected mode such that the (counter)-propagating mode shows oscillations (right) left of the boundary.

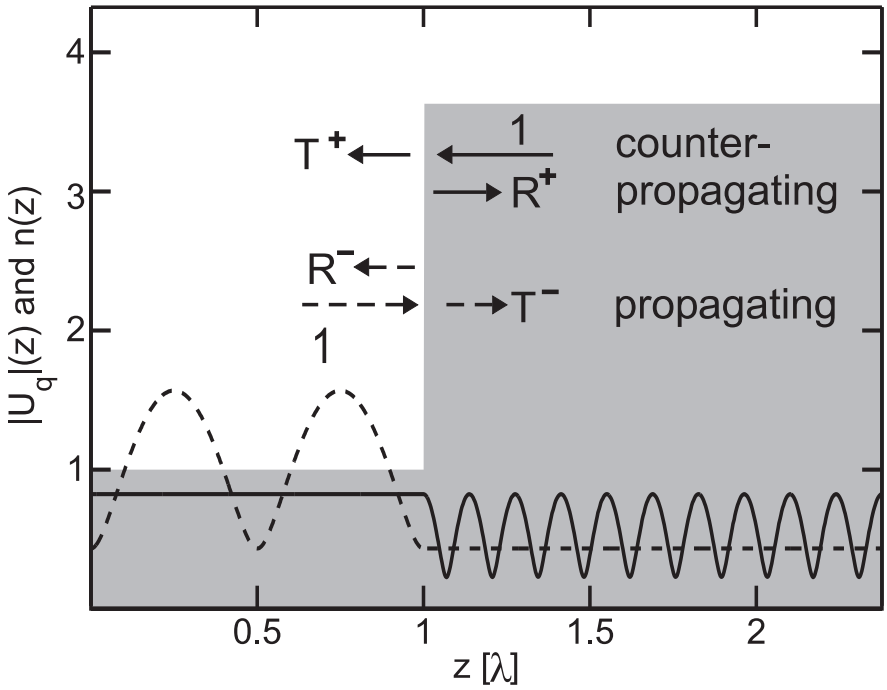

Figure 4.1.: The background-refractive-index profile is shown as a gray shaded area. The dashed and the solid lines depict the propagating and the counter-propagating modes which are resonant to the exciton-1s energy, respectively. The dashed (solid) arrows indicate that the (counter-)propagating mode consists of the incident plane wave with amplitude 1. Reflection and transmission coefficients are R^- (R^+) and T^-(T^+), respectively.

The most general ansatz for the mode functions in a region j is

$$U_q^j(z) = A_j e^{iq_j(z-z_j)} + B_j e^{-iq_j(z-z_j)}\,, \tag{4.1}$$

where A_j and B_j are the coefficients in the respective regions and $q_j = \sqrt{n_j^2(\omega)\mathbf{q}^2 - \mathbf{q}_\parallel}$ is the corresponding photon wave-vector in z-direction with refractive index $n_j(\omega)$.

From the given refractive indices, we can compute the reflection and transmission coefficients at the boundary between regions j and $j+1$ via the continuity condition of the mode functions and their space derivatives. We find

$$\mathsf{T}_j^+ = \frac{2q_{j+1}}{q_j + q_{j+1}}\,, \qquad \mathsf{T}_j^- = \frac{2q_j}{q_j + q_{j+1}}\,, \tag{4.2}$$

$$\mathsf{R}_j^+ = \frac{q_{j+1} - q_j}{q_j + q_{j+1}}\,, \qquad \mathsf{R}_j^- = \frac{q_j - q_{j+1}}{q_j + q_{j+1}}\,. \tag{4.3}$$

These coefficients can be used to relate the mode functions in neighboring regions via

$$\begin{pmatrix} A_{j+1} \\ B_{j+1} \end{pmatrix} = \mathsf{M}_j \cdot \begin{pmatrix} A_j \\ B_j \end{pmatrix}\,, \tag{4.4}$$

where M_j is the transfer matrix defined by

$$\mathsf{M}_j = \frac{1}{\mathsf{T}_j^+} \begin{pmatrix} \left(\mathsf{T}_j^+\mathsf{T}_j^- - \mathsf{R}_j^+\mathsf{R}_j^-\right) e^{ik_j(z_{j+1}-z_j)} & \mathsf{R}_j^+ e^{-ik_j(z_{j+1}-z_j)} \\ -\mathsf{R}_j^- e^{ik_j(z_{j+1}-z_j)} & e^{-ik_j(z_{j+1}-z_j)} \end{pmatrix}\,. \tag{4.5}$$

In structures with multiple layers, we apply Eq. (4.4) iteratively. Consequently, we can express the coefficients of the mode function in region j by those in the first region via the matrix equation

$$\begin{pmatrix} A_{j+1} \\ B_{j+1} \end{pmatrix} = \mathsf{M}_j\mathsf{M}_{j-1}...\mathsf{M}_1 \begin{pmatrix} A_1 \\ B_1 \end{pmatrix} \equiv \mathcal{M}_j \begin{pmatrix} A_1 \\ B_1 \end{pmatrix}\,. \tag{4.6}$$

The product matrix $\mathcal{M}_j$ describes the collective reflection and transmission through the entire stack consisting of the first j layers of the device also including multiple reflections within the sample structure. In analogy to Eq. (4.5), we can therefore define collective reflection and transmission coefficients $\mathcal{R}^+$,$\mathcal{R}^-$,$\mathcal{T}^+$, and $\mathcal{T}^-$ for the first j layers as

$$\mathcal{R}_{j+1}^- = \mathcal{R}_j^- + \frac{\mathsf{R}_{j+1}^-\mathcal{T}_j^-\mathcal{T}_j^+ e^{2ik_j(z_{j+1}-z_j)}}{1 - \mathsf{R}_{j+1}^-\mathcal{R}_j^+ e^{2ik_j(z_{j+1}-z_j)}}, \tag{4.7}$$

$$\mathcal{R}_{j+1}^+ = \mathcal{R}_{j+1}^+ + \frac{\mathcal{R}_j^+\mathcal{T}_{j+1}^+\mathcal{T}_{j+1}^- e^{2ik_j(z_{j+1}-z_j)}}{1 - \mathsf{R}_{j+1}^-\mathcal{R}_j^+ e^{2ik_j(z_{j+1}-z_j)}}, \tag{4.8}$$

$$\mathcal{T}_{j+1}^- = \frac{\mathcal{T}_j^-\mathsf{T}_{j+1}^- e^{ik_j(z_{j+1}-z_j)}}{1 - \mathsf{R}_{j+1}^-\mathcal{R}_j^+ e^{2ik_j(z_{j+1}-z_j)}}, \tag{4.9}$$

$$\mathcal{T}_{j+1}^+ = \frac{\mathsf{T}_{j+1}^+\mathcal{T}_j^+ e^{ik_j(z_{j+1}-z_j)}}{1 - \mathsf{R}_{j+1}^-\mathcal{R}_j^+ e^{2ik_j(z_{j+1}-z_j)}}\,. \tag{4.10}$$

The collective transfer matrix may then be determined via

$$\mathcal{M}_j = \frac{1}{T_{j+1}^-} \begin{pmatrix} \mathcal{T}_{j+1}^+\mathcal{T}_{j+1}^- - \mathcal{R}_{j+1}^+\mathcal{R}_{j+1}^- & \mathcal{R}_{j+1}^+ \\ -\mathcal{R}_{j+1}^- & 1 \end{pmatrix}\,. \tag{4.11}$$

4.2. Coupling between the quantum well and the dielectric structure

So far, our transfer matrix includes only the reflections and transmissions inside the sample structure due to a certain background-refractive-index profile. As a next step, we will show how the coupling of a QW to its dielectric environment can be modeled.

In principle, the dielectric environment can be coupled to the QW by expanding the electric field in terms of mode functions. The electric field is then dynamically described via an equation of motion for the photon creation and annihilation operators. This mode expansion has to be used for incoherent light fields because in that limit the electric field is determined exclusively by its quantum fluctuations such that a consistent quantum-mechanical treatment of the light field is essential.

In the coherent limit, we can describe the light field classically such that an alternative method to the mode expansion can be used. We describe the optical response of the QW microscopically via the SBE as already discussed in Chap. 3. The optical response of the QW can then be expressed in terms of reflection, transmission and absorption coefficients according to [31]

$$R(\omega) = \frac{i\xi(\omega)}{1-i\xi(\omega)}, \tag{4.12}$$

$$T(\omega) = \frac{1}{1-i\xi(\omega)}, \tag{4.13}$$

where $\xi(\omega)$ is defined by Eq. (3.4) and the absorption is given in Eq. (3.3). Thus, we may treat the QW like a separate layer of the refractive-index profile with its own transfer matrix M_{QW}. We neglect variations in the refractive index between QW and its adjacent layers. This assumption is no restriction to the structure because the refractive-index change may be included in the usual transfer-matrix calculation sketched above in Sec. 4.1.

Inserting Eqs. (4.12) and (4.13) into Eq. (4.5), we can define the QW transfer matrix as

$$\mathsf{M}_{QW} = \begin{pmatrix} 1+i\xi & i\xi \\ -i\xi & 1-i\xi \end{pmatrix}. \tag{4.14}$$

This definition contains the self-consistent light-matter coupling due to the coupling of the macroscopic polarization P to the wave equation (3.2) via Eq. (3.4) (see also [31]). As a consequence, radiative broadening effects are fully included.

Transmission and reflection through a dielectric structure that includes a QW between regions $k-1$ and $k+1$ can be described by the matrix product

$$\mathcal{M}_j = \mathsf{M}_j\mathsf{M}_{j-1}...\mathsf{M}_{k+1}\mathsf{M}_{QW}\mathsf{M}_{k-1}...\mathsf{M}_1 \tag{4.15}$$

Analogously, MQW samples can be simulated by simply putting multiple QW transfer matrices at the respective positions of the matrix product. The inclusion of the QWs into the system leads to a finite linear absorption according to Eq. (3.3) while in the absence of any QWs, the transfer-matrix method ensures that reflection plus transmission yields unity as long as the dielectric environment is optically inactive.

4.3. Comparison between experiment and theory

Using the developed model for the coupling between the QWs and the dielectric environment, we can compare the numerical simulations against experiments. Thus, we present in this section measured and computed absorption, transmission and reflection of the structure that is shown in the Fig. 4.2a.

The investigated structure is relatively complicated and contains several buffer layers and two superlattices as well as an AR-coating. The active region consists of ten 10 nm wide GaAs QWs that are separated by 10 nm layers of $Al_{0.3}Ga_{0.7}As$. A tick layer of GaAs provides bulk absorption which is included in our model via a complex refractive index in the respective region. The solid (dashed) line shows the (counter-)propagating mode resonant to the 1s-exciton energy.

Frame 4.2b shows a comparison between measured and computed absorption. The black line in indicates the experimental absorption. The red (blue) line shows the result if the frequency dependence of the background refractive-index is neglected (included). The corresponding figures for reflection and transmission are depicted in the bottom frames 4.2c and 4.2d, respectively. The color code of the curves in these two frames is the same as for the absorption.

We find an absorption peak at 1.5 eV that corresponds to the bulk absorption while the peak at 1.55 eV shows the heavy-hole 1s-resonance. The experimental data indicate also a third absorption peak at slightly higher energies. This peak corresponds to the light hole which is not included in our investigations due to the restrictions of our theory to two-band situations. Apart from the absorption peak, the light hole introduces a continuum absorption which is simulated via a phenomenological frequency dependent absorption function.

The reflection spectrum is dominated by Fabry-Perot fringes. The energy period of these fringes can be related to the propagation time of the light through the complete sample. Therefore, the energy period of the Fabry-Perot fringes directly depends on the background refractive-indices that are used to model the sample structure. A comparison between the experimental and the numerical data in Fig. 4.2c shows that too large Fabry-Perot periods are observed when the frequency dependence of the background refractive-index is neglected. The inclusion of the frequency dependence is needed to predict the energy period of the Fabry-Perot fringes for a wide energy range.

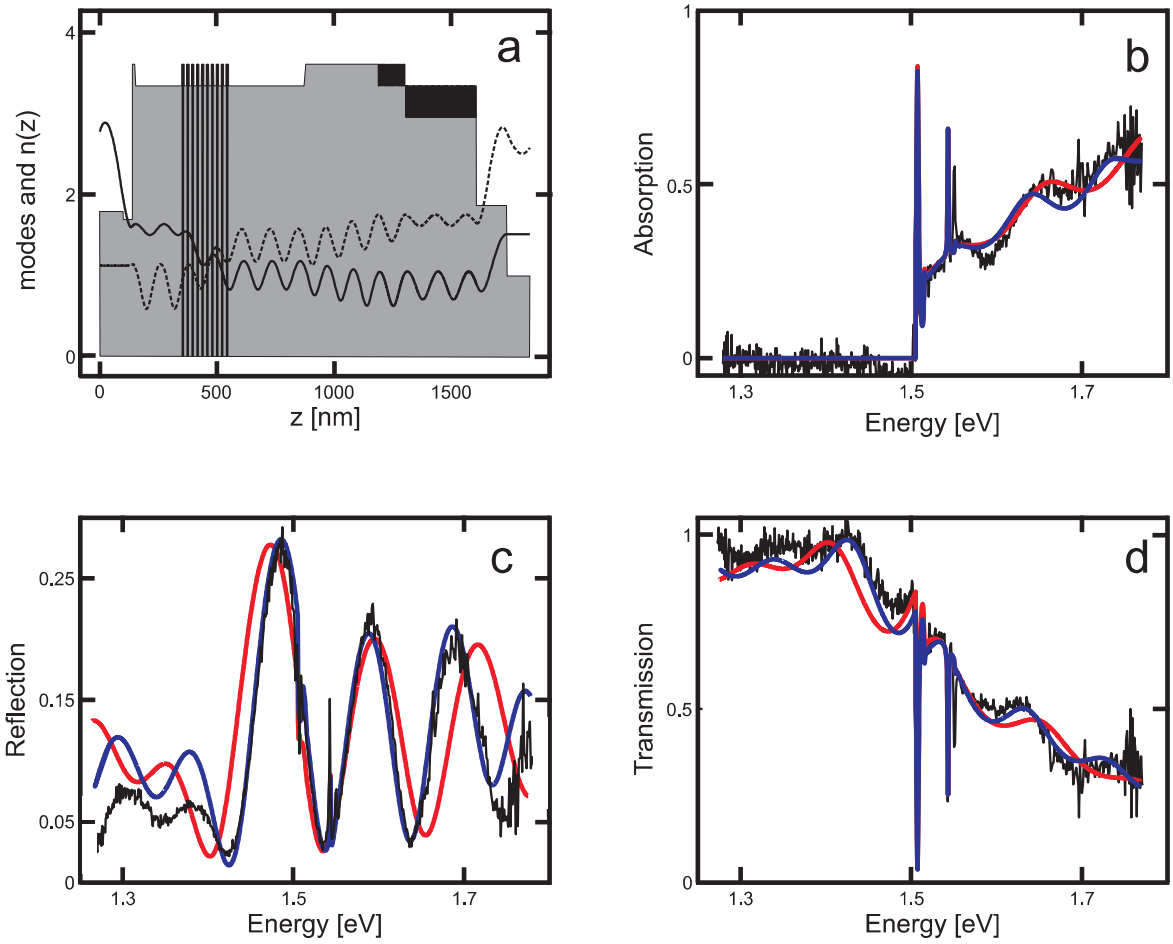

Figure 4.2.: *Reflection, transmission and absorption of a QW-heterostructure in the coherent limit:* The investigated structure is indicated in frame a as shaded area. The solid (dashed) line shows the (counter-)propagating mode that is resonant with the exciton 1s energy. Frames b,c, and d show absorption, reflection, and transmission as a function of energy. In these three frames, the black line depicts the experimental data while the red and the blue line indicate the respective numerically simulated quantities. The blue line corresponds to the calculation that includes the frequency dependence of the refractive index. The red curve is obtained if the frequency dependence is neglected. *The experiments have been performed in the group of Steve Cundiff at Jila, Boulder.*

5. Photoluminescence and semiconductor luminescence equations

5.1. Entirely incoherent conditions

So far, we have investigated the linear response of a QW in the coherent light-matter-interaction regime. In this context, we have extended the treatment of the carrier-scattering to describe the absorption of indirect Ge-type QWs. We have applied the extended scattering theory to compare the density-dependent absorption between a GaAs and a Ge QW. Additionally, we have investigated how the dielectric environment influences the optical response.

In this chapter, we will concentrate on incoherent situations where all coherent quantities like the coherent polarization $\langle p_{\mathbf{k}_\parallel} \rangle$ and the classical electric field $\langle E \rangle \propto \langle B \rangle$ have decayed. Beyond the classical limit, we even demand the absence of any phase coherences implying that quantities of the form $\Delta\langle [B_q^\dagger]^m B_q^n \rangle$ are zero when $m \neq n$. Note that this condition excludes squeezing at $t = 0$ because squeezing is related to quantities of the form $\Delta\langle B_q B_q \rangle$.

The incoherent limit can, for example, be reached if the excitation happens high above the band edge and the carriers have to scatter down to the Γ-point for emission at the exciton resonances [57–60]. The carrier scattering as discussed in Chap. 3 and the phonon scattering [35, 61–64] in conjunction with the finite radiative lifetime of carrier excitations [32, 65] leads to the loss of phase coherences on a ps time-scale. At the same time, the scattering processes build up incoherent correlations and carrier populations. The incoherent dynamics takes place on a ns time scale, i.e. is much slower than the coherent dynamics. After the coherences have vanished, the light field is exclusively described by its quantum fluctuations. A typical example for light that exhibits this statistic is thermal light.

Other methods that allows for reaching the incoherent regime are injection pumping via an electric current or, more exotically, the direct excitation via an incoherent light source, e.g., by the emission from an exciton condensate [31, 66]. Both procedures lead to a build up of incoherent correlations without the intermediate step of first creating a coherent polarization.

5.2. Semiconductor luminescence equations

Perhaps the simplest example of purely non-classical light is the PL which is proportional to the rate of the correlated photon number

$$I^{PL}_{\mathbf{q}_\parallel,q_\perp} = \frac{\partial}{\partial t}\Delta\langle B^\dagger_{\mathbf{q}_\parallel,q_\perp} B_{\mathbf{q}_\parallel,q_\perp}\rangle\,. \tag{5.1}$$

Again, we determine the dynamics by applying Heisenberg's equation of motion and the cluster-expansion-truncation scheme. Applying this scheme, we demand that all coherent quantities are zero. We keep track of the QW index m since we are also interested in the radiative coupling between the QWs in the incoherent regime. With these assumptions, the equation of motion for the correlated photon number reads [31, 34]

$$\begin{aligned} i\hbar\frac{\partial}{\partial t}\Delta\langle B^\dagger_{\mathbf{q}_\parallel,q_\perp} B_{\mathbf{q}_\parallel',q_\perp'}\rangle &= (\hbar\omega_{q'} - \hbar\omega_q)\,\Delta\langle B^\dagger_{\mathbf{q}_\parallel,q_\perp} B_{\mathbf{q}_\parallel',q_\perp'}\rangle \\ &\quad + i\sum_{m,\mathbf{k}_\parallel} \mathcal{F}^\star_{m,\mathbf{q}_\parallel',q_\perp'}\,\Pi^{\mathbf{k}_\parallel,m}_{\mathbf{q}_\parallel,q_\perp} \\ &\quad + i\sum_{m,\mathbf{k}_\parallel} \mathcal{F}_{m,\mathbf{q}_\parallel,q_\perp}\left(\Pi^{\mathbf{k}_\parallel,m}_{\mathbf{q}_\parallel',q_\perp'}\right)^\star \end{aligned} \tag{5.2}$$

where the first line describes the propagation of the light field. The second and third lines introduce the light-matter coupling via the photon-assisted polarizations

$$\Pi^{\mathbf{k}_\parallel,m}_{\mathbf{q}_\parallel,q_\perp} \equiv \Delta\langle B^\dagger_{\mathbf{q}_\parallel,q_\perp} a^\dagger_{m,v,\mathbf{k}_\parallel} a_{m,c,\mathbf{k}_\parallel+\mathbf{q}_\parallel}\rangle\,, \tag{5.3}$$

which describe correlated processes where an electron-hole pair with center-of-mass momentum $\hbar\mathbf{q}_\parallel$ in QW m is annihilated while a photon with the same momentum is created. The coupling strength is abbreviated by the expression $\mathcal{F}_{m,\mathbf{q}_\parallel,q_\perp} \equiv d_{cv}\mathcal{E}_q U_{\mathbf{q},m}(QW)$.

The dynamics of the photon-assisted polarizations is given by

$$\begin{aligned} i\hbar\frac{\partial}{\partial t}\Pi^{\mathbf{k}_\parallel,m}_{\mathbf{q}_\parallel,q_\perp} &= \left(\tilde{\epsilon}^m_{\mathbf{k}_\parallel,\mathbf{q}_\parallel} - \hbar\omega_{\mathbf{q}_\parallel}\right)\Pi^{\mathbf{k}_\parallel,m}_{\mathbf{q}_\parallel,q_\perp} \\ &- (1 - f^{e,m}_{\mathbf{k}_\parallel+\mathbf{q}_\parallel} - f^{h,m}_{\mathbf{k}_\parallel})\sum_{\mathbf{k}_\parallel'} V_{\mathbf{k}_\parallel-\mathbf{k}_\parallel'}\Pi^{\mathbf{k}_\parallel',m}_{\mathbf{q}_\parallel,q_\perp} \\ &+ i\Omega^{RC}_m(\mathbf{k}_\parallel,\mathbf{q}_\parallel,q_\perp) - (1 - f^{e,m}_{\mathbf{k}_\parallel+\mathbf{q}_\parallel} - f^{h,m}_{\mathbf{k}_\parallel})\Delta\langle B^\dagger_{\mathbf{q}_\parallel,q_\perp} B_{\mathbf{q}_\parallel\Sigma_m}\rangle \\ &+ \mathcal{F}_{m,\mathbf{q}_\parallel,q_\perp}\Omega^{SE}_m(\mathbf{k}_\parallel,\mathbf{q}_\parallel) + i\hbar\frac{\partial}{\partial t}\Pi^{\mathbf{k}_\parallel,m}_{\mathbf{q}_\parallel,q_\perp}|_{scatt}, \end{aligned} \tag{5.4}$$

with the Coulomb renormalized single-particle energies

$$\tilde{\epsilon}^m_{\mathbf{k}_\parallel,\mathbf{q}_\parallel} = \epsilon^e_{m,\mathbf{k}_\parallel+\mathbf{q}_\parallel} + \epsilon^h_{m,\mathbf{k}_\parallel} - \sum_{\mathbf{k}_\parallel'} V_{\mathbf{k}_\parallel-\mathbf{k}_\parallel'}\left(f^{e,m}_{\mathbf{k}_\parallel'+\mathbf{q}_\parallel} + f^{h,m}_{\mathbf{k}_\parallel'}\right). \tag{5.5}$$

The equation is structurally similar to the polarization equation (3.7). As discussed there, the Coulomb interaction appears in the Coulomb sum $\sum_{\mathbf{k}_\parallel'} V_{\mathbf{k}_\parallel-\mathbf{k}_\parallel'} \Pi^{\mathbf{k}_\parallel',m}_{\mathbf{q}_\parallel,q_\perp}$ and provides excitonic resonances [35] (see also Appendix A).

The electron and hole distributions of QW m

$$f^{e,m}_{\mathbf{k}_\parallel} = \langle a^\dagger_{m,c,\mathbf{k}_\parallel} a_{m,c,\mathbf{k}_\parallel} \rangle \,, \tag{5.6}$$

$$f^{h,m}_{\mathbf{k}_\parallel} = 1 - \langle a^\dagger_{m,v,\mathbf{k}_\parallel} a_{m,v,\mathbf{k}_\parallel} \rangle \,, \tag{5.7}$$

enter the photon-assisted polarization via the phase-space-filling factor $(1 - f^{e,m}_{\mathbf{k}_\parallel} - f^{h,m}_{\mathbf{k}_\parallel})$ and the spontaneous-emission source

$$\Omega^{SE}_m(\mathbf{k}_\parallel, \mathbf{q}_\parallel) = f^{e,m}_{\mathbf{k}_\parallel+\mathbf{q}_\parallel} f^{h,m}_{\mathbf{k}_\parallel} + \sum_{\mathbf{l}_\parallel} c^{\mathbf{q}_\parallel,\mathbf{k}_\parallel,\mathbf{l}_\parallel}_{X\, m,m} \,. \tag{5.8}$$

The electron-hole plasma $f^e f^h$ acts as a source to the photon-assisted polarization whenever carriers are present. Additionally, the spontaneous-emission source contains the truly correlated electron-hole pairs

$$c^{\mathbf{q}_\parallel,\mathbf{k}_\parallel',\mathbf{k}_\parallel}_{X\, m',m} = \Delta\langle a^\dagger_{m,c,\mathbf{k}_\parallel} a^\dagger_{m',v,\mathbf{k}_\parallel'} a_{m',c,\mathbf{k}_\parallel'+\mathbf{q}_\parallel} a_{m,v,\mathbf{k}_\parallel-\mathbf{q}_\parallel} \rangle \tag{5.9}$$

with equal QW indices $m = m'$. The correlated electron-hole pairs can describe correlated plasma as well as exciton populations in QW m [31]. Due to the structure of the spontaneous emission, both contributions, the exciton population as well as the single-particle electron-hole plasma, can fundamentally be the origin of excitonic luminescence [18, 19, 34, 67, 68]. It can be shown that the PL is dominated by the uncorrelated electron-hole plasma especially at high carrier temperatures and densities while for low carrier temperatures and low to medium carrier densities the PL is dominated by the recombination of true excitons [18, 19]. As a consequence, luminescence from the exciton resonances is not a unique signature for exciton populations in the system.

Electron-hole correlations between different QWs $m \neq m'$ enter via the recombination correlation which is given by

$$\Omega^{RC}_m(\mathbf{k}_\parallel, \mathbf{q}_\parallel, q_\perp) = \sum_{m' \neq m} \mathcal{F}_{m',\mathbf{q}_\parallel,q_\perp} \sum_{\mathbf{l}_\parallel} c^{\mathbf{q}_\parallel,\mathbf{k}_\parallel,\mathbf{l}_\parallel}_{X\, m,m'} \,. \tag{5.10}$$

The MQW coupling is further modified by the stimulated contribution

$$\Delta\langle B^\dagger_{\mathbf{q}_\parallel,q_\perp} B_{\mathbf{q}_\parallel \Sigma_m} \rangle \,, \tag{5.11}$$

where the collective photon operator $B_{\mathbf{q}_\parallel,\Sigma_m} = \sum_{q_\perp'} i\mathcal{F}_{m,\mathbf{q}_\parallel,q_\perp'} B_{\mathbf{q}_\parallel,q_\perp'}$ includes all photons with in-plane momentum $\mathbf{q}_\parallel$ coupling to QW m. The stimulated term provides the coupling between different light modes and defines how the photon correlations couple to the photon-assisted polarization. In the weak light-matter-coupling regime, the stimulated term leads to a radiative decay of excitations and spectrally broadens the excitonic peak

[55, 69] while in the strong-coupling regime, it is responsible for normal mode-splitting effects [32, 43, 70, 71]. For incoherent excitation, the stimulated term acts as a driving source for the photon-assisted polarization. The scattering contributions due to higher order correlations and phonon interaction are abbreviated in the term $\Pi^{\mathbf{k}_\parallel,m}_{\mathbf{q}_\parallel,q_\perp}|_{scatt}$.

We set up the equation of motion for the two-particle correlation c_X and neglect Coulomb-induced contributions that are proportional to $f^e - f^h$. This is justified for low carrier densities when these contributions are much smaller than the dominant Coulomb contributions that are proportional to phase-space filling $(1 - f^e - f^h)$. This approximation is often referred to as *main-sum approximation* [64, 72]. Applying the main-sum approximation, the equation of motion for the two-particle correlation c_X is given by

$$\begin{aligned}
i\hbar\frac{\partial}{\partial t}c^{\mathbf{q}_\parallel,\mathbf{k}_\parallel',\mathbf{k}_\parallel}_{X\,m',m} &= \epsilon^{\mathbf{q}_\parallel,\mathbf{k}_\parallel',\mathbf{k}_\parallel}_{m',m}\, c^{\mathbf{q}_\parallel,\mathbf{k}_\parallel',\mathbf{k}_\parallel}_{X\,m',m} + S^{\mathbf{q}_\parallel,\mathbf{k}_\parallel',\mathbf{k}_\parallel}_{X\,m',m} \\
&- (1 - f^{e,m'}_{\mathbf{k}_\parallel'+\mathbf{q}_\parallel} - f^{h,m'}_{\mathbf{k}_\parallel'}) \sum_{\mathbf{l}_\parallel\neq\mathbf{k}_\parallel'} V_{\mathbf{l}_\parallel-\mathbf{k}_\parallel'} c^{\mathbf{q}_\parallel,\mathbf{l}_\parallel,\mathbf{k}_\parallel}_{X\,m',m} \\
&+ (1 - f^{e,m}_{\mathbf{k}_\parallel} - f^{h,m}_{\mathbf{k}_\parallel-\mathbf{q}_\parallel}) \sum_{\mathbf{l}_\parallel\neq\mathbf{k}_\parallel} V_{\mathbf{l}_\parallel-\mathbf{k}_\parallel} c^{\mathbf{q}_\parallel,\mathbf{k}_\parallel',\mathbf{l}_\parallel}_{X\,m',m} \\
&- (1 - f^{e,m'}_{\mathbf{k}_\parallel'+\mathbf{q}_\parallel} - f^{h,m'}_{\mathbf{k}_\parallel'}) \sum_{q_\perp'} i\mathcal{F}_{m',\mathbf{q}_\parallel',q_\perp'} \left(\Pi^{\mathbf{k}_\parallel,m}_{\mathbf{q}_\parallel,q_\perp'}\right)^\star \\
&- (1 - f^{e,m}_{\mathbf{k}_\parallel} - f^{h,m}_{\mathbf{k}_\parallel-\mathbf{q}_\parallel}) \sum_{q_\perp'} i\mathcal{F}^\star_{m,\mathbf{q}_\parallel',q_\perp'} \Pi^{\mathbf{k}_\parallel',m'}_{\mathbf{q}_\parallel,q_\perp'} \\
&+ i\hbar\frac{\partial}{\partial t}c^{\mathbf{q}_\parallel,\mathbf{k}_\parallel',\mathbf{k}_\parallel}_{X\,m',m}|_{scatt}
\end{aligned} \tag{5.12}$$

with the renormalized electron-hole pair energy

$$\epsilon^{\mathbf{q}_\parallel,\mathbf{k}_\parallel',\mathbf{k}_\parallel}_{m',m} = \tilde{\epsilon}^{m}_{\mathbf{k}_\parallel-\mathbf{q}_\parallel,\mathbf{q}_\parallel} - \tilde{\epsilon}^{m'}_{\mathbf{k}_\parallel',\mathbf{q}_\parallel}, \tag{5.13}$$

and the single-particle-scattering source

$$\begin{aligned}
S^{\mathbf{q}_\parallel,\mathbf{k}_\parallel',\mathbf{k}_\parallel}_{X\,m',m} &= \delta_{m,m'} V_{\mathbf{k}_\parallel'+\mathbf{q}_\parallel-\mathbf{k}_\parallel} \\
&\times\Big[f^{e,m}_{\mathbf{k}_\parallel'+\mathbf{q}_\parallel} f^{h,m}_{\mathbf{k}_\parallel'}(1 - f^{e,m}_{\mathbf{k}_\parallel})(1 - f^{h,m}_{\mathbf{k}_\parallel-\mathbf{q}_\parallel}) \\
&- f^{e,m}_{\mathbf{k}_\parallel} f^{h,m}_{\mathbf{k}_\parallel-\mathbf{q}_\parallel}(1 - f^{e,m}_{\mathbf{k}_\parallel'+\mathbf{q}_\parallel})(1 - f^{h,m)}_{\mathbf{k}_\parallel'})\Big] .
\end{aligned} \tag{5.14}$$

This source term exists only for equal QW indices and resembles Coulomb scattering within one and the same QW between different $\mathbf{k}_\parallel$-states. A transformation of Eq. (5.12) into the exciton basis shows that the S_X term does not create a diagonal exciton population but introduces correlations between different exciton states [31, 67].

Excitonic pair-state resonances are introduced by the Coulomb sums in the second and third line of Eq. (5.12). Additionally, the spontaneous recombination of correlated electron-hole pairs is described by the terms containing Π when $m = m'$. For $m \neq m'$, these terms correlate electron-hole pairs in different QWs due to photon-mediated

recombination and excitation of electron-hole pairs. The scattering due to higher order correlations is given by $c_{X\,m',m}^{\mathbf{q}_\parallel,\mathbf{k}_\parallel{}',\mathbf{k}_\parallel}|_{scatt}$.

In order to close the set of equations, we have to set up the equations of motion for the electron and hole distributions,

$$\begin{aligned} i\hbar\frac{d}{dt}f_{\mathbf{k}_\parallel+\mathbf{q}_\parallel}^{e,m} &= \sum_{\mathbf{q}_\parallel,q_\perp} i\Big(\mathcal{F}_{m,\mathbf{q}_\parallel,q_\perp}\left(\Pi_{\mathbf{q}_\parallel,q_\perp}^{\mathbf{k}_\parallel,m}\right)^\star + \mathcal{F}_{m,\mathbf{q}_\parallel,q_\perp}^\star\Pi_{\mathbf{q}_\parallel,q_\perp}^{\mathbf{k}_\parallel,m}\Big) \\ &+ i\hbar\frac{d}{dt}f_{\mathbf{k}_\parallel+\mathbf{q}_\parallel}^{e,m}|_{scatt} \qquad (5.15) \\ i\hbar\frac{d}{dt}f_{\mathbf{k}_\parallel}^{h,m} &= \sum_{\mathbf{q}_\parallel,q_\perp} i\Big(\mathcal{F}_{m,\mathbf{q}_\parallel,q_\perp}\left(\Pi_{\mathbf{q}_\parallel,q_\perp}^{\mathbf{k}_\parallel,m}\right)^\star + \mathcal{F}_{m,\mathbf{q}_\parallel,q_\perp}^\star\Pi_{\mathbf{q}_\parallel,q_\perp}^{\mathbf{k}_\parallel,m}\Big) \\ &+ i\hbar\frac{d}{dt}f_{\mathbf{k}_\parallel}^{h,m}|_{scatt}\ . \qquad (5.16) \end{aligned}$$

The electron and hole distributions are mainly driven by the collective sum over the photon-assisted polarization processes. The scattering due to higher order correlations is contained in $f_{\mathbf{k}_\parallel}^{h/e,m}|_{scatt}$. These terms are responsible for a relaxation of the carrier distribution toward thermal equilibrium.

5.3. Exciton number

The SLE allow us to study the number of excitons with vanishing center-of-mass momentum $\mathbf{q}_\parallel = 0$. Therefore, we introduce the transformation

$$\Delta N_{\nu,\lambda}^{m,m'} = \sum_{\mathbf{k}_\parallel,\mathbf{k}_\parallel{}'} \phi_\nu^L(\mathbf{k}_\parallel)\Big[\phi_\lambda^L(\mathbf{k}_\parallel{}')\Big]^\star c_{X\,m',m}^{0,\mathbf{k}_\parallel{}',\mathbf{k}_\parallel} \qquad (5.17)$$

$$c_{X\,m',m}^{0,\mathbf{k}_\parallel{}',\mathbf{k}_\parallel} = \sum_{\nu,\lambda}\Delta N_{\nu,\lambda}^{m,m'}\Big[\phi_\nu^R(\mathbf{k}_\parallel)\Big]^\star\phi_\lambda^R(\mathbf{k}_\parallel{}') \qquad (5.18)$$

where $\Delta N_{\lambda,\lambda}^{m,m}$ indicates the number of excitons at state λ in QW m. The same quantity with unequal indices $m \neq m'$ or/and $\lambda \neq \nu$ describes plasma correlations between electron-hole pairs in different QWs or/and different states. The transformation is mediated via the left- and right-handed exciton eigenfunctions $\phi_\nu^L(\mathbf{k}_\parallel)$ and $\phi_\nu^R(\mathbf{k}_\parallel)$ [35, 66](see also Appendix A).

5.4. Treatment of the scattering

The scattering contributions in Eqs. (5.4), (5.12), (5.15), and (5.16) lead to energy renormalizations as well as dephasing and screening effects. Unfortunately, the general structure of these terms is relatively complicated [31] and the inclusion of their full dynamics would be numerically very time consuming. Therefore, it is desirable to find an ansatz that allows us to include the scattering on an approximative level while the essential features of the scattering are included.

The electron-electron as well as the electron-phonon scattering relax the carrier distributions toward thermal equilibrium on a fs time scale. Besides the fast scattering dynamics, the spontaneous emission leads to a slow nanosecond (ns) decay of the carriers. In the investigated time regime of some ps, both effects contribute only weakly such that we can neglect the carrier dynamics (5.15) and (5.16) and assume a quasi equilibrium with fixed carrier densities. The fast equilibration is taken into account by using quasi-stationary Fermi distributions for a given carrier density and temperature.

The structure of Eqs. (5.2), (5.4), (5.12), (5.15), and (5.16) shows that the carrier dynamics is the only place where different in-plane momenta $\mathbf{q}_\parallel$ are coupled. In the limit of thermal equilibrium, the scattering terms can be considered not to produce a $\mathbf{q}_\parallel$-dependent coupling. In this situation, the coupling between different $\mathbf{q}_\parallel$ in Eqs. (5.2), (5.4) and (5.12) can be ignored. Consequently, the principal coupling effects among the QWs and between the QWs and the dielectric environment can be understood by concentrating on the emission perpendicular to the QW planes, i.e. $\mathbf{q}_\parallel = 0$. Under these conditions, $\Pi_{\mathbf{q}_\parallel,q_\perp}$ depends on $\mathbf{q}_\parallel$ mainly via the angle between the QW and the light field. Thus, we can assume that the emission angle enters the SLE only via an appropriate geometrical factor.

In our numerical evaluations, the steady-state luminescence is consequently proportional to the flux of the photon number into the normal direction,

$$I_{PL}(\omega = c|q_\perp|) = \frac{\partial}{\partial t}\Delta\langle B^\dagger_{0,q_\perp} B_{0,q_\perp}\rangle \ . \tag{5.19}$$

In the limit of quasi-stationary carrier distributions, we can simplify the scattering contributions in Eqs. (5.4) and (5.12). The easiest possible approximation is to introduce a constant dephasing γ. This works nicely in the case of the photon-assisted polarization for low to moderate carrier densities such that we can approximate the scattering term in Eq. (5.4) by

$$i\hbar\frac{\partial}{\partial t}\Pi^{\mathbf{k}_\parallel,m}_{\mathbf{q}_\parallel,q_\perp}|_{scatt} = -i\gamma\Pi^{\mathbf{k}_\parallel,m}_{\mathbf{q}_\parallel,q_\perp} \ . \tag{5.20}$$

For high carrier densities, the homogeneous dephasing would lead to Hartree-Fock shifts of the exciton resonances which are not seen experimentally. Thus, the scattering has to be treated on a higher level. One could for example treat the scattering on a 2nd-Born level as we have already discussed for the coherent polarization in Sec. 3.5. However, we restrict our investigations in the incoherent regime to sufficiently low carrier densities such that we may use the approximation (5.20).

The scattering term in the c_X-correlation cannot be treated via dephasing-rate approximations since a simple dephasing constant would lead to a decay of the exciton populations. More specifically, in an exciton basis, we have to distinguish between complex transition amplitudes $\Delta N^{m,m'}_{\nu,\lambda}$ for $\nu \neq \lambda$ or $m \neq m'$ and real-valued populations $\Delta N^{m,m}_{\nu,\nu}$. Since the latter do not carry a phase, they are insensitive to dephasing. They can only decay non-radiatively (not considered here) or via spontaneous emission of a photon which is included in Eq. (5.12). Therefore, we introduce a scattering term

$$i\hbar\frac{\partial}{\partial t}c^{0,\mathbf{k}_\parallel{}',\mathbf{k}_\parallel}_{X\ m',m}|_{scatt} \quad = \quad -2i\gamma c^{0,\mathbf{k}_\parallel{}',\mathbf{k}_\parallel}_{X\ m',m}$$

$$+ \quad 2i\gamma\delta_{m,m'} \sum_{\lambda} \Delta N^{m,m'}_{\lambda,\lambda} \phi^R_\nu(\mathbf{k}_\parallel) \left[\phi^R_\lambda(\mathbf{k}_\parallel{}')\right]^\star , \tag{5.21}$$

which assures that only the off-diagonal correlations are dephased and the diagonal exciton populations remain unaffected.

In addition to the dephasing effects, carrier-carrier scattering also leads to an effective plasma screening. For that purpose, we use Lindhardt screening in single-plasmon-pole approximation [35] such that the bare Coulomb matrix elements in Eqs. (5.4) and (5.12) become screened by the additional factor

$$\frac{1}{\varepsilon(\mathbf{k}_\parallel)} = 1 + \frac{\omega_{pl}^2}{(\omega + i\delta)^2 - \omega_q^2}, \tag{5.22}$$

where ω_{pl} is the plasma-frequency and ω_q is the effective plasmon frequency. For consistency reasons, we have to add the Coulomb-hole selfenergy term

$$\Delta\epsilon_G = \sum_{\mathbf{k}_\parallel} (W_{\mathbf{k}_\parallel} - V_{\mathbf{k}_\parallel}) \tag{5.23}$$

to the Coulomb renomalization of the single-particle energies (5.5).

In the following chapters, we investigate the PL of a MQW system inside a complicated dielectric structure, i.e. we want to determine the changes to the detected PL induced by the dielectric environment and how the PL in a MQW device differs from that of a single-QW device. Since we want to investigate these effects separately, we have to divide the environmental influence from the MQW coupling.

This distinction is not trivial because the quantum description of the light field demands a quantum treatment of the detector. Additionally, the structure of the SLE is such that the dielectric environment enters the SLE in multiple places. Consequently in Chap. 6, we will introduce transformations for the single-QW SLE that allow us to treat the dielectric environment and the QW PL separately.

After the influence of the dielectric environment on the PL is understood, we investigate in Chap. 7 the radiative QW coupling in MQW Bragg-structures. We concentrate on clarifying how the quantum emission is changed by the MQW structure, which processes are responsible for these changes, and what the implications for the exciton lifetimes are.

6. Effects of the dielectric environment on the quantum-well luminescence

In Chap. 4, we have discussed that the dielectric environment may lead to strong modifications of the transmission and reflection spectra of a QW in the coherent limit. The same applies for the incoherent limit when the classical electric field is zero. The dielectric structure may induce Fabry-Perot oscillations [53] and modify the coupling strength between light mode and QW [32].

From atomic systems, we know that the radiative environment may lead to a reduction or an enhancement of the spontaneous emission [73–79]. Analogously, the modification of the coupling strength between light mode and QW leads to enhanced or reduced radiative lifetimes of excitations in the QW device [80, 81].

The differing radiative lifetimes directly imply a change in the emission behavior of the QW such that the PL spectra will show modifications in their radiative broadening [54–57]. In the strong coupling regime, we even expect crucial changes of the spectral shape due to normal-mode splitting [32, 43, 71, 82, 83]. All these effects depend on the precise dielectric structure and typically vary with the emission direction.

The information about the dielectric environment is already contained in the SLE via the mode functions that enter the SLE in several places due to the explicit quantum treatment of the light field. As a result, the photonic environment influences the SLE and thus the QW emission in a non-trivial manner. In particular, even a small change in the dielectric background formally implies that the full SLE must be solved again to resolve the emission properties of the new configuration.

Unfortunately, the numerical solution of SLE is computationally very tedious, especially if the dynamics of the scattering contributions is included. This makes device simulations for sample design purposes very inefficient and time consuming. Consequently, it is clearly desirable to separate the pure QW emission, corresponding to the emission into free space, from the influence of the dielectric environment.

To this aim, the basic idea is to multiply the free-space PL with a filter function that depends on the dielectric environment to obtain the actual PL. This filter-function approach allows us to solve the numerically demanding SLE only once for free-space emission. Different device structures may then be simulated via different filter functions that are numerically easy to compute.

The concept of decoupling the environment and the emission problem has already been shown to work for atomic dipoles and approaches using Fermi's golden rule [78, 79]. However, it is not a priori clear how to apply this filter function approximation to compute PL which is obtained as the result of a fully microscopical theory.

In order to concentrate on the pure effects of the photonic environment, we neglect QW-QW coupling and study single-QW PL. We assume elevated carrier densities and temperatures resulting in hardly any excitons existing in our system. Under these conditions, we can neglect the coupling to the c_X correlations and investigate pure plasma PL. Additionally, we do not need to take into account the exact expression of the microscopic Coulomb scattering since the structure of the coupling between QW and dielectric environment is not influenced by the scattering. Thus, we can simulate different scattering strengths via different homogeneous broadenings.

6.1. Transformed semiconductor luminescence equations

Most of the results in the following sections 6.1-6.5 are published in Ref. [84] such that we will keep the argumentation close to that paper.

With the approximations mentioned above, all information about the dielectric-background geometry is contained in the mode functions which appear in the SLE structure via $\mathcal{F}_{\mathbf{q}_\parallel,q_\perp}$ in the spontaneous emission source Ω^{SE}, the stimulated contribution to Eq. (5.4), and the coupling of the single-photon correlations to the photon-assisted polarizations in Eq. (5.2). As a result, the photonic environment influences the SLE and, thus, the QW emission in a non-trivial manner. In particular, even small changes in the dielectric background imply that the full SLE have to be solved again to resolve the emission properties of the new configuration. In order to decouple the material aspects from the light-matter coupling, we condense the $\mathcal{F}_{\mathbf{q}_\parallel,q_\perp}$ contributions into one term by introducing the transformation

$$B^\dagger_{\mathbf{q}_\parallel,q_\perp} = \mathcal{F}_{\mathbf{q}_\parallel,q_\perp} b^\dagger_{\mathbf{q}_\parallel,q_\perp} \,. \tag{6.1}$$

The correlated photon number and the photon-assisted polarization then become

$$\Delta\langle B^\dagger_{\mathbf{q}_\parallel,q_\perp} B_{\mathbf{q}_\parallel{}',q'_\perp}\rangle = \mathcal{F}_{\mathbf{q}_\parallel,q_\perp}\left(\mathcal{F}_{\mathbf{q}_\parallel{}',q'_\perp}\right)^\star \Delta\langle b^\dagger_{\mathbf{q}_\parallel,q_\perp} b_{\mathbf{q}_\parallel{}',q'_\perp}\rangle\,, \tag{6.2}$$

$$\Pi^{\mathbf{k}_\parallel}_{\mathbf{q}_\parallel,q_\perp} = \mathcal{F}_{\mathbf{q}_\parallel,q_\perp}\pi^{\mathbf{k}_\parallel}_{\mathbf{q}_\parallel,q_\perp} \equiv \mathcal{F}_{\mathbf{q}_\parallel,q_\perp}\Delta\langle b^\dagger_{\mathbf{q}_\parallel,q_\perp} a^\dagger_{v,\mathbf{k}_\parallel} a_{c,\mathbf{k}_\parallel+\mathbf{q}_\parallel}\rangle \,. \tag{6.3}$$

We transfer Eqs. (5.2) and (5.4) into the new variables and end up with the transformed SLE given by

$$\begin{aligned} i\hbar\frac{\partial}{\partial t}\Delta\langle b^\dagger_{\mathbf{q}_\parallel,q_\perp} b_{\mathbf{q}_\parallel{}',q'_\perp}\rangle &= \left(\hbar\omega_{q'} - \hbar\omega_q\right)\Delta\langle b^\dagger_{\mathbf{q}_\parallel,q_\perp} b_{\mathbf{q}_\parallel{}',q'_\perp}\rangle \\ &\quad + i\sum_{\mathbf{k}_\parallel}\pi^{\mathbf{k}_\parallel}_{\mathbf{q}_\parallel,q_\perp} + i\sum_{\mathbf{k}_\parallel}\left(\pi^{\mathbf{k}_\parallel}_{\mathbf{q}_\parallel{}',q'_\perp}\right)^\star \end{aligned} \tag{6.4}$$

$$\begin{aligned} i\hbar\frac{\partial}{\partial t}\pi^{\mathbf{k}_\parallel}_{\mathbf{q}_\parallel,q_\perp} &= \left(\tilde{\epsilon}_{\mathbf{k}_\parallel,\mathbf{q}_\parallel} - \hbar\omega_{\mathbf{q}_\parallel}\right)\pi^{\mathbf{k}_\parallel}_{\mathbf{q}_\parallel,q_\perp} \\ &\quad - \left(1 - f^e_{\mathbf{k}_\parallel+\mathbf{q}_\parallel} - f^h_{\mathbf{k}_\parallel}\right)\sum_{\mathbf{k}_\parallel{}'} V_{\mathbf{k}_\parallel-\mathbf{k}_\parallel{}'}\pi^{\mathbf{k}_\parallel{}'}_{\mathbf{q}_\parallel,q_\perp} + i\Omega^{SE}(\mathbf{k}_\parallel,\mathbf{q}_\parallel) \end{aligned}$$

$$
\begin{aligned}
&- \quad (1 - f^e_{\mathbf{k}_\parallel+\mathbf{q}_\parallel} - f^h_{\mathbf{k}_\parallel}) \sum_{q'_\perp} i \left|\mathcal{F}_{\mathbf{q}_\parallel,q'_\perp}\right|^2 \Delta\langle b^\dagger_{\mathbf{q}_\parallel,q_\perp} b_{\mathbf{q}_\parallel,q'_\perp}\rangle \\
&+ \quad i\hbar \frac{\partial}{\partial t} \pi^{\mathbf{k}_\parallel}_{\mathbf{q}_\parallel,q_\perp}\big|_{\text{scatt}} \,. \qquad (6.5)
\end{aligned}
$$

The transformation isolates the $\mathcal{F}_{\mathbf{q}_\parallel,q_\perp}$ contribution which thus appears only in the stimulated term. Apart from this term, Eqs. (6.4) and (6.5) have the structure of the SLE for a single QW in free space. If the stimulated term can be neglected, Eq. (6.2) introduces a simple relation between the PL into free-space and the PL into an arbitrary dielectric environment.

6.2. Detection operator and filter function approximation for a single quantum-well system

As we have already seen in the discussion of the coherent polarization, a QW inside a dielectric structure couples to both, the propagating and the counter-propagating modes. The coupling strength is directly related to the absolute square of the mode function at the QW position. Therefore, the exact position of the QW has a strong influence on the detected PL. In order to determine the coupling strength, we may use the transfer-matrix method discussed in Chap. 4. This method yields the full information about the mode functions as well as about the reflection and the transmission coefficients.

The coupling of the detector to the light field is introduced by detector modes which are plane waves for a detector located outside the sample. A comparison of the detector modes and the light mode basis shows that a detector left of the sample measures the reflected part of the propagating mode plus the transmitted part of the counter-propagating mode. Analogously, the detector right of the structure detects the transmitted part of the propagating mode plus the reflected part of the counter-propagating mode. The proper detector operators are consequently given by [34]

$$
\begin{aligned}
d^L_{\mathbf{q}} &= \mathcal{R}^-_{\mathbf{q}} B_{+\mathbf{q}} + \sqrt{\frac{q_{z_L}}{q_{z_R}}} \mathcal{T}^+_{\mathbf{q}} B_{-\mathbf{q}} \\
&= \mathcal{R}^-_{\mathbf{q}} \left(\mathcal{F}_{+\mathbf{q}}\right)^\star b_{+\mathbf{q}} + \sqrt{\frac{q_{z_L}}{q_{z_R}}} \mathcal{T}^+_{\mathbf{q}} \left(\mathcal{F}_{-\mathbf{q}}\right)^\star b_{-\mathbf{q}} \,, \qquad (6.6)
\end{aligned}
$$

with $q_{z_j} = \sqrt{n_j^2 \mathbf{q}^2 - \mathbf{q}_\parallel{}^2}$ where q_{z_j} is the photon momentum on the left ($j = L$) or right ($j = R$) of the sample. The information concerning the QW position is contained in $\mathcal{F}_{\mathbf{q}}$. The respective detection operator for a detection right of the sample is given by

$$
\begin{aligned}
d^R_{\mathbf{q}} &= \sqrt{\frac{q_{z_R}}{q_{z_L}}} \mathcal{T}^-_{\mathbf{q}} B_{+\mathbf{q}} + \mathcal{R}^+_{\mathbf{q}} B_{-\mathbf{q}} \\
&= \sqrt{\frac{q_{z_R}}{q_{z_L}}} \mathcal{T}^-_{\mathbf{q}} \left(\mathcal{F}_{+\mathbf{q}}\right)^\star b_{+\mathbf{q}} + \mathcal{R}^+_{\mathbf{q}} \left(\mathcal{F}_{-\mathbf{q}}\right)^\star b_{-\mathbf{q}} \,. \qquad (6.7)
\end{aligned}
$$

The detected intensities therefore read

$$\begin{aligned}
\langle d^\dagger_{\mathbf{q}} d_{\mathbf{q}}\rangle_L &= |\mathcal{R}^-_{\mathbf{q}}|^2\,|\mathcal{F}_{+\mathbf{q}}|^2\,\Delta\langle b^\dagger_{+\mathbf{q}} b_{+\mathbf{q}}\rangle + \frac{q_{z_L}}{q_{z_R}}|\mathcal{T}^+_{\mathbf{q}}|^2\,|\mathcal{F}_{-\mathbf{q}}|^2\,\Delta\langle b^\dagger_{-\mathbf{q}} b_{-\mathbf{q}}\rangle \\
&+ \sqrt{\frac{q_{z_L}}{q_{z_R}}}\Big[(\mathcal{R}^-_{\mathbf{q}})^\star\mathcal{T}^+_{\mathbf{q}}\mathcal{F}_{+\mathbf{q}}\,(\mathcal{F}_{-\mathbf{q}})^\star\,\Delta\langle b^\dagger_{+\mathbf{q}} b_{-\mathbf{q}}\rangle \\
&+ \mathcal{R}^-_{\mathbf{q}}(\mathcal{T}^+_{\mathbf{q}})^\star\mathcal{F}_{-\mathbf{q}}\,(\mathcal{F}_{+\mathbf{q}})^\star\,\Delta\langle b^\dagger_{-\mathbf{q}} b_{+\mathbf{q}}\rangle\Big] \qquad (6.8)\\
\langle d^\dagger_{\mathbf{q}} d_{\mathbf{q}}\rangle_R &= \frac{q_{z_R}}{q_{z_L}}|\mathcal{T}^-_{\mathbf{q}}|^2\,|\mathcal{F}_{+\mathbf{q}}|^2\,\Delta\langle b^\dagger_{+\mathbf{q}} b_{+\mathbf{q}}\rangle + |\mathcal{R}^+_{\mathbf{q}}|^2\,|\mathcal{F}_{-\mathbf{q}}|^2\,\Delta\langle b^\dagger_{-\mathbf{q}} b_{-\mathbf{q}}\rangle \\
&+ \sqrt{\frac{q_{z_R}}{q_{z_L}}}\Big[(\mathcal{T}^-_{\mathbf{q}})^\star\mathcal{R}^+_{\mathbf{q}}\mathcal{F}_{+\mathbf{q}}\,(\mathcal{F}_{-\mathbf{q}})^\star\,\Delta\langle b^\dagger_{+\mathbf{q}} b_{-\mathbf{q}}\rangle \\
&+ \mathcal{T}^-_{\mathbf{q}}(\mathcal{R}^+_{\mathbf{q}})^\star\mathcal{F}_{-\mathbf{q}}\,(\mathcal{F}_{+\mathbf{q}})^\star\,\Delta\langle b^\dagger_{-\mathbf{q}} b_{+\mathbf{q}}\rangle\Big]\ . \qquad (6.9)
\end{aligned}$$

If the stimulated contribution has a negligible effect on the PL, Eqs. (6.4) and (6.5) imply that $\Delta\langle b^\dagger_{\pm\mathbf{q}} b_{\pm\mathbf{q}}\rangle \equiv \Delta\langle b^\dagger_{\mathbf{q}} b_{\mathbf{q}}\rangle$ does not depend on the propagation direction such that the detected PL can be calculated via

$$\langle d^\dagger_{\mathbf{q}} d_{\mathbf{q}}\rangle_L \equiv F^L_{\mathbf{q}}\Delta\langle b^\dagger_{\mathbf{q}} b_{\mathbf{q}}\rangle \qquad\qquad \langle d^\dagger_{\mathbf{q}} d_{\mathbf{q}}\rangle_R \equiv F^R_{\mathbf{q}}\Delta\langle b^\dagger_{\mathbf{q}} b_{\mathbf{q}}\rangle\ , \qquad (6.10)$$

as the product of the free-space PL $\Delta\langle b^\dagger_{\mathbf{q}} b_{\mathbf{q}}\rangle$ and the filter function

$$\begin{aligned}
F^L_{\mathbf{q}} &= |\mathcal{R}^-_{\mathbf{q}}|^2\,|\mathcal{F}_{+\mathbf{q}}|^2 + \frac{q_{z_L}}{q_{z_R}}|\mathcal{T}^+_{\mathbf{q}}|^2\,|\mathcal{F}_{-\mathbf{q}}|^2 \\
&+ \sqrt{\frac{q_{z_L}}{q_{z_R}}}\Big[(\mathcal{R}^-_{\mathbf{q}})^\star\mathcal{T}^+_{\mathbf{q}}\mathcal{F}_{+\mathbf{q}}\,(\mathcal{F}_{-\mathbf{q}})^\star + \mathcal{R}^-_{\mathbf{q}}(\mathcal{T}^+_{\mathbf{q}})^\star\mathcal{F}_{-\mathbf{q}}\,(\mathcal{F}_{+\mathbf{q}})^\star\Big] \qquad (6.11)\\
F^R_{\mathbf{q}} &= \frac{q_{z_R}}{q_{z_L}}|\mathcal{T}^-_{\mathbf{q}}|^2\,|\mathcal{F}_{+\mathbf{q}}|^2 + |\mathcal{R}^+_{\mathbf{q}}|^2\,|\mathcal{F}_{-\mathbf{q}}|^2 \\
&+ \sqrt{\frac{q_{z_R}}{q_{z_L}}}\Big[(\mathcal{T}^-_{\mathbf{q}})^\star\mathcal{R}^+_{\mathbf{q}}\mathcal{F}_{+\mathbf{q}}\,(\mathcal{F}_{-\mathbf{q}})^\star + \mathcal{T}^-_{\mathbf{q}}(\mathcal{R}^+_{\mathbf{q}})^\star\mathcal{F}_{-\mathbf{q}}\,(\mathcal{F}_{+\mathbf{q}})^\star\Big]\ . \qquad (6.12)
\end{aligned}$$

6.3. Applicability of the filter function

When the stimulated contribution $\sum_{q'_\perp} i|\mathcal{F}_{\mathbf{q}_\parallel,q_\perp}|^2\Delta\langle b^\dagger_{\mathbf{q}_\parallel,q_\perp} b_{\mathbf{q}_\parallel,q'_\perp}\rangle$ is relatively weak, its dominant effect is a radiative broadening of the excitonic resonance. The corresponding decay constant Γ_{rad} can be obtained by inserting the formal solution of Eq. (5.2) into Eq. (5.4). In a medium with homogeneous refractive index, the exciton 1s-resonance constitutes the strongest contribution to the spectrum. In the absence of phonon and carrier scattering, the broadening of the 1s resonance is dominated by the radiative decay of the 1s-state. Thus, we can simplify the expression of the radiative decay constant Γ_{rad} to its 1s contribution, [31, 55, 85]

$$\Gamma_{rad} = \frac{d^2_{cv}\,|\phi_{1s}(0)|^2\,|U_{q_{1s}}|^2}{2\varepsilon_0} q_{1s}\ , \qquad (6.13)$$

where q_{1s} is the absolute value of the photon wave vector corresponding to the 1s-exciton energy and $\phi_{1s}(0)$ is the exciton-wave function at $\mathbf{r} = 0$. For a homogeneous material, $|U_{q_{1s}}|^2 = \frac{1}{n}$.

In the following numerical analysis, we investigate how the stimulated contribution influences the PL spectra and identify the conditions under which the filter-function approximation, Eq. (6.10), may be used. We assume that an 8 nm wide QW is positioned inside the same dielectric environment as was introduced in Fig. 4.1. We vary the QW position to change the coupling strength between the mode function and the QW. Additionally, different homogeneous broadenings γ are used corresponding to different excitation conditions and different scattering strengths [43]. We investigate the steady-state PL for carrier densities between $1\times10^{10}\,\mathrm{cm}^{-2}$ and $1\times10^{12}\,\mathrm{cm}^{-2}$ for a temperature of 77 K. In this parameter range, most of the PL originates from the uncorrelated electron-hole plasma whereas significant exciton populations are not expected [18].

Figure 6.1 presents two situations where the QW is either placed into the minimum (Fig. 6.1a) or the maximum (Fig. 6.1b) of the counter-propagating modes. The (counter)-propagating mode is given as a dashed (solid) line, the black vertical line indicates the QW position and the shaded area shows the refractive-index profile. Frames c–f show the PL spectra obtained via the filter function, Eq. (6.10), together with the free-space PL that is used as an input (dashed line) and the spectra computed with the full SLE (shaded area). Figures 6.1c–6.1d display a situation where the dephasing constant $\gamma = 0.21\,\mathrm{meV}$ is of a similar size as the radiative decay constant in GaAs, $\Gamma_{rad} = 0.05\,\mathrm{meV}$. The corresponding PL spectra for $\gamma = 2.1\,\mathrm{meV} \gg \Gamma_{\mathrm{rad}}$ are presented in frames Fig. 6.1e and Fig. 6.1f.

As long as γ is much larger than Γ_{rad}, the homogeneous broadening dominates the peak width such that it is a very good approximation to neglect the stimulated contribution. In that limit, the filter-function approximation excellently agrees with the full SLE computation as a comparison between the dashed lines and shaded areas in frames 6.1e and 6.1f shows.

When γ and Γ_{rad} are of similar size or when Γ_{rad} is larger than γ, the radiative broadening significantly contributes to the peak width such that the stimulated contribution cannot be neglected and the filter-function approximation leads to an underestimation of the peak width (6.1c-d). In this limit, the filter function approximation needs to be extended.

The basic idea is to find a quantitative estimate for the radiative broadening based solely on the photonic eigenmodes. Once such an estimate is known, we can simply add it to the homogeneous broadening of the free-space calculation. In this way, we find a modified free-space spectrum which, together with the filter function, yields an improved PL spectrum. According to Eq. (6.13), the radiative broadening depends on the dielectric environment of the QW via the factor $|U_{q_{1s}}|^2$. Thus, we can use the mode functions at the exciton frequency to relate the radiative broadening of the actual structure Γ_{rad}^{actual} to the known radiative broadening in free space $\Gamma_{rad}^{free}(n=1)$ via

$$\Gamma_{rad}^{actual} = \Gamma_{rad}^{free}(n=1)\frac{|U_{+\mathbf{q}}|^2 + |U_{-\mathbf{q}}|^2}{2}\,. \tag{6.14}$$

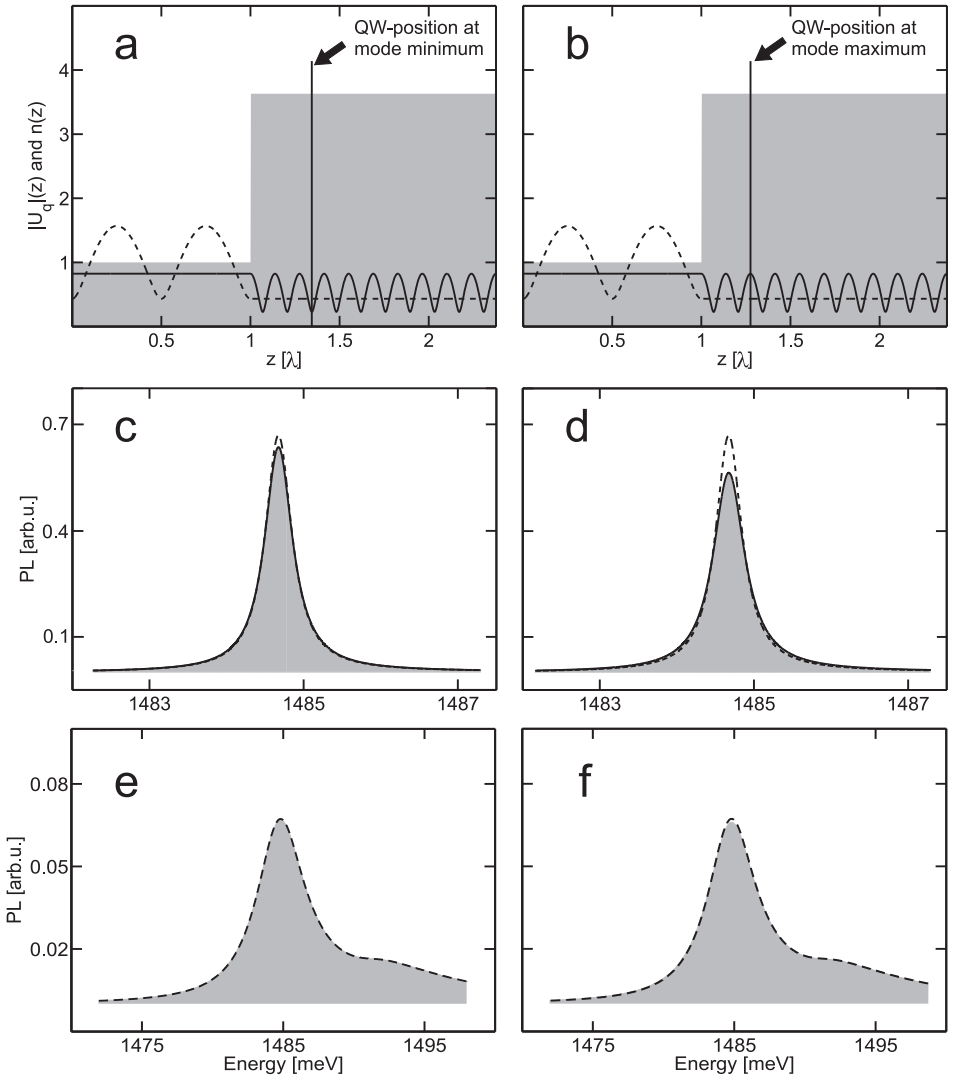

Figure 6.1.: PL spectra of a QW positioned either in the mode minimum (left column) or mode maximum (right column). Frames a and b show the refractive index profile as a shaded area while the (counter-)propagating mode is shown as dashed (solid) line. The QW position is indicated by the vertical line. Frames c and d show the PL spectra corresponding to the QW positions depicted in a and b for a homogeneous broadening of $\gamma = 0.21\,\mathrm{meV}$ and a radiative broadening of $\Gamma_{rad} = 0.084\,\mathrm{meV}$. The shaded area shows the result of the full SLE-calculation. The dashed line is the product of the filter function and the free-space PL. The solid black line is obtained by multiplying the filter function with the free-space PL where an adjusted homogeneous dephasing constant is used. Frames e and f show the same comparison when the homogeneous broadening is $\gamma = 2.1\,\mathrm{meV}$ and therefore much larger than the radiative broadening.

The plus and the minus sign in Eq. (6.14) indicate the propagating and counter-propagating modes. In order to include Γ_{rad}^{actual} into the free-space PL, it is not necessary to redo the full SLE calculation. Instead, we can use the convolution

$$\tilde{I}_{free}^{PL}(\omega) = \frac{1}{\pi} \int I_{free}^{PL}(\omega') \frac{\left(\Gamma_{rad}^{actual}\right)^2}{\left(\hbar\omega' - E_{1s}\right)^2 + \left(\Gamma_{rad}^{actual}\right)^2} d\omega' \,, \tag{6.15}$$

where $\tilde{I}_{free}^{PL}(\omega)$ is the adjusted free-space PL and E_{1s} is the energy at the exciton 1s-resonance. We find improved PL spectra if we multiply the adjusted free-space PL and the filter function. The improved PL spectra via that extended filter-function approach are presented as solid lines in frames 6.1c and 6.1d. They excellently agree with the full SLE calculation even for small γ.

6.4. Angular dependence

So far, we have analyzed the quantum emission perpendicular to the QW plane. Now, we want to extend our numerical investigations to finite angles. In Figs. 6.2 and 6.3, we discuss results for the structure shown in Fig. 6.3a. The system basically consists of a GaAs-barrier with an embedded QW. To the right of the barrier we add an AR-coating layer and assume vacuum outside the sample.

We present the corresponding PL perpendicular to the QW plane and at an emission angle of 80° in Figs. 6.2a and 6.2b, respectively. The shaded area shows the PL spectrum computed using the full SLE. The dashed lines indicate the free-space PL perpendicular to the QW plane divided by the refractive index of GaAs ($n = 3.63$). This result corresponds to the spectrum expected for a QW in a homogeneous GaAs structure. The free-space spectrum is computed without radiative broadening. The solid lines show the result computed via the filter functions, i.e., the vacuum free-space PL perpendicular to the QW plane times the angle-dependent filter-function. In the right frame, for better visibility of the spectral shape, we have multiplied by a factor of four the curves showing the full SLE spectrum as well as curve which is obtained from the filter-function approximation. The computed filter functions are presented in the insets of the two frames.

In Fig. 6.2b, we find strong modifications of the peak shape with respect to the free-space case for large angles, i.e., the PL spectrum even shows multiple peaks while the free-space result suggests only one peak. In contrast, the perpendicular emission spectrum does not show a multi-peak structure. The differences originate from the anti-reflection coating in the dielectric structure that is designed to inhibit reflections at the right boundary for perpendicular emission. In our case, the AR-coating layer must have a refractive index of $\sqrt{n_{GaAs}}$, were n_{GaAs} is the background refractive-index of GaAs. The width of the layer has to be $\lambda/4$ to show perfect reflection inhibition. For perpendicular incidence, the light path through the AR-coating layer is exactly $\lambda/4$. In that case, the dielectric structure becomes similar to the step-function refractive index

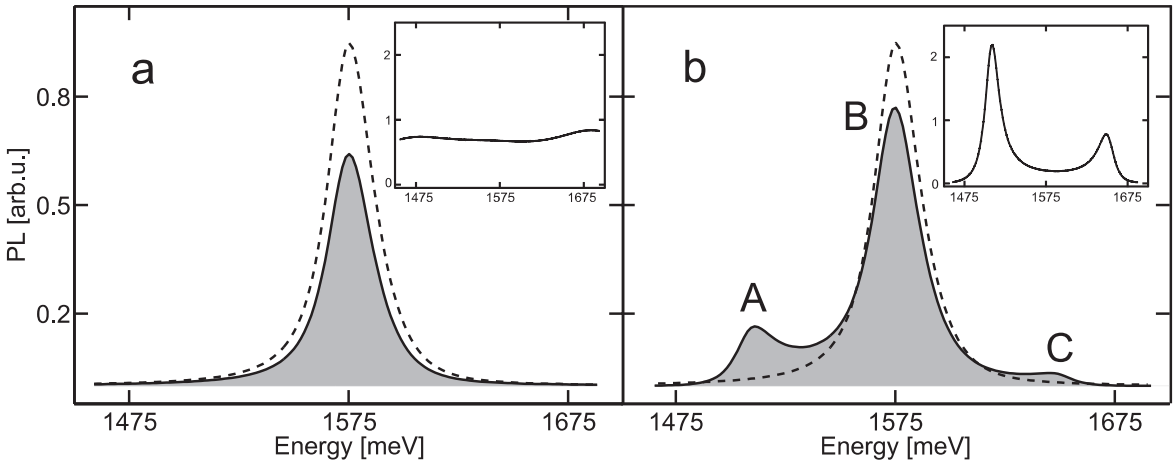

Figure 6.2.: PL spectra for the structure depicted in Fig. 6.3a. Frame a shows the PL perpendicular to the QW plane while frame b shows the spectra at an angle of 80°. The shaded areas indicate the full SLE PL while the dashed lines indicate the free-space PL perpendicular to the QW plane without the radiative broadening. The solid lines can be obtained by multiplying the filter functions with the free-space PL. In the bottom subfigure, the shaded area and the solid line are multiplied by a factor of four for better visibility of the spectral shape. The three peak maxima are labeled via the letters A,B and C for the subsequent discussion. The insets in both frames indicate the computed filter functions.

profile discussed in Fig. 6.1 and the filter function is nearly frequency independent due to the absence of any special periodicities in the vicinity of the exciton resonance.

At an incident angle ϕ, the light path through the AR-coating layer increases by a factor of $cos^{-1}\phi$ due to the geometry. Thus, for large angles, the AR-coating does not provide the special periodicity needed to inhibit the reflection and the AR-coating acts as a normal step in the refractive-index profile.

In order to explain the spectral shape in Fig. 6.2b, we first analyze the mode functions corresponding to the energy of the local PL-maxima A and C as well as to the overall PL-maximum B. Therefore in Fig. 6.3a and 6.3b, we compare propagating and counter-propagating modes. We indicate the mode functions corresponding to the frequency B as solid lines while the mode functions for the frequency A are shown as a dashed lines. The mode functions corresponding to the energy C are similar to case A. In general, one finds that the mode functions at frequency A show much stronger oscillations inside the structure than the modes corresponding to B. The origin of that effect is the anti-reflection coating at the right-hand side of the structure that works better for frequency B than for frequency A. As a consequence, the value of the mode functions at the QW position and therefore the coupling between the QW and the light modes is larger for frequency A than for frequency B.

Additionally, Figure 6.3c shows the reflection (solid line) and transmission (dashed

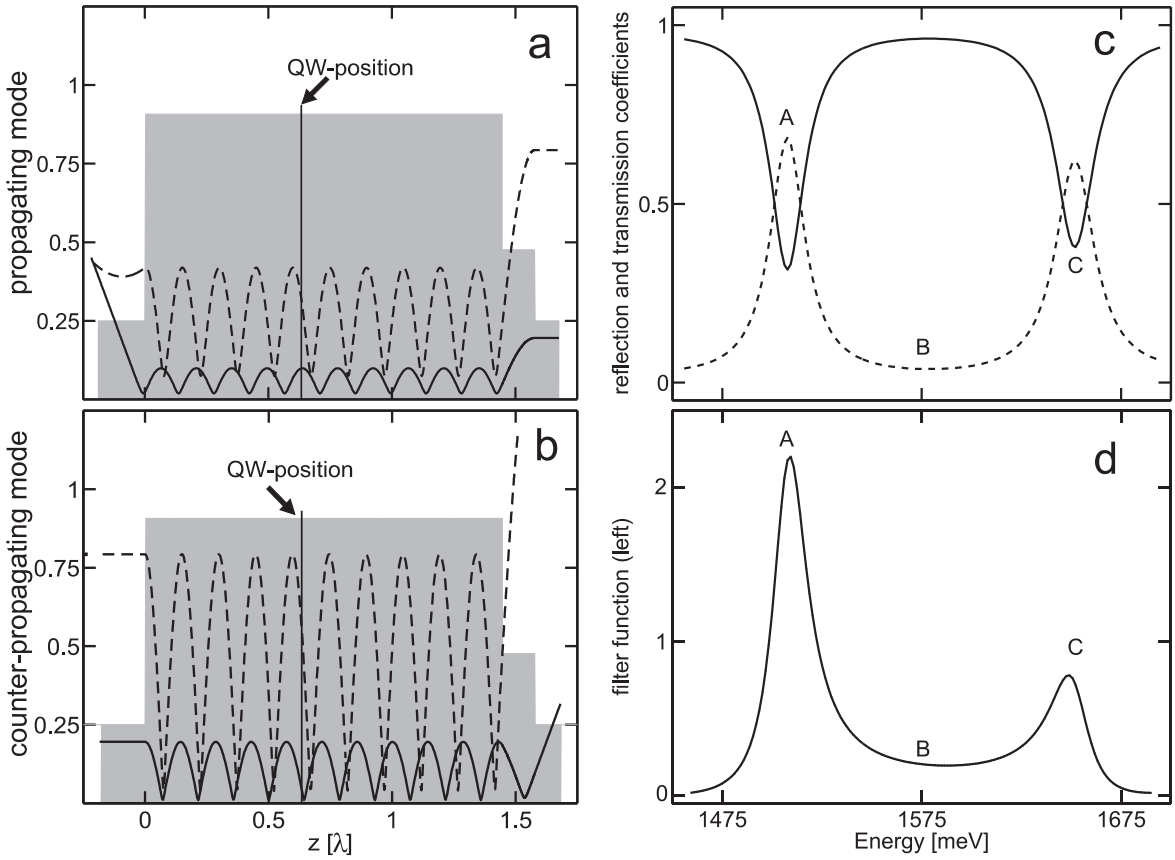

Figure 6.3.: Frames a and b show the propagating and counter-propagating modes for the frequencies corresponding to the peak maximum A(B) in Fig. 6.2b as a dashed (solid) line. The mode function corresponding to peak C is qualitatively similar to case A. The QW position is indicated via a black arrow. The shaded area shows the refractive index profile. The frequency dependent reflection and transmission coefficients are indicated as solid and dashed lines in frame c. The filter function for a detector positioned to the right of the sample was already shown as an inset in Fig. 6.2b and for better comparison is redrawn here as frame d.

line) coefficients of the background structure as a function of the energy. We obtain a maximum of the transmission at the frequency corresponding to A while the reflection is maximized at frequency B. Applying Eq. (6.10), we obtain the filter-function shown in Fig. 6.3d. The filter function shows pronounced maxima at energies A and C while it is minimal in B.

Since the total PL is obtained as the product of the filter function and the vacuum spectrum, it is large if either one is large. Therefore, the spectral peak at frequency B originates from the large value of the free-space PL at that energy while the local maxima in A and C come from the large value of the filter function which is multiplied with the tail of the free-space spectrum. Consequently, the peaked structure can be explained as

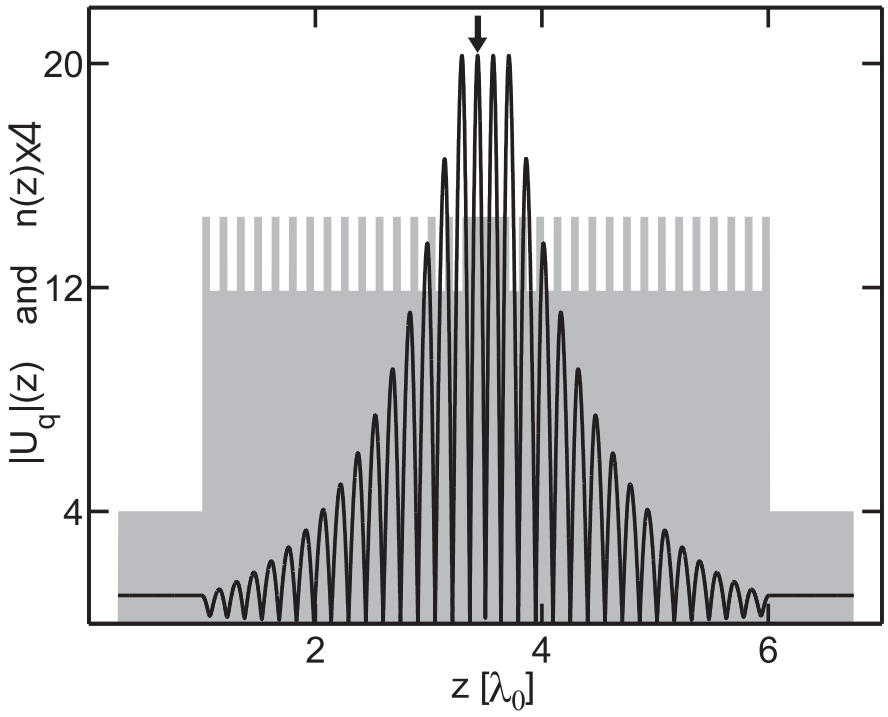

Figure 6.4.: A cavity with 15 Bragg-periods of n=2.97 and n=3.63 to each side. The size of the cavity is $\frac{3\lambda_0}{2n}$, where λ_0 is the light-wave length in vacuum corresponding to the 1s-energy and n is its refractive index. The shaded area shows the refractive index profile while the black solid line line depicts the resonant mode. The QW position at the mode maximum is indicated by a black arrow.

an interplay between the free-space PL and the filter function containing the structure of the mode functions. Despite the strong modifications of the PL-spectra for large angles, we obtain a very good agreement between the full-SLE results and the filter-function approximation. Consequently, the filter-function approximation includes the full angle dependence of the PL and thus constitutes a very reliable method to predict PL spectra in the weak-coupling regime for a large variation of realistic dielectric structures.

6.5. Limits of the extended filter-function approach

The role of the stimulated contribution can become so decisive that a simple approximative inclusion of the radiative broadening is not sufficient. In order to determine the limits of the extended filter-function approximation (EFFA), we calculate the QW PL when the QW is placed between two DBR. This cavity should strongly enhance the stimulated effects. A typical DBR structure as investigated in this section is shown in Fig. 6.4. Since the reflectivity of the Bragg mirrors can be controlled by changing the number of Bragg layers, we investigate cavities with different mirrors. For each of

the cavities, we adjust the cavity resonance such that it coincides with the 1s-exciton resonance.

In Fig. 6.5a, we show the PL spectra that are computed via the full SLE for cavities whose Bragg mirrors contain between 1 (bottom curve) and 12 (top curve) Bragg layers. The black vertical lines mark the position of the PL peaks. Frame b presents the mode strengths at the QW position $|U_{QW}|^2$ that belong to the respective cavities as a function of the energy. The curves corresponding to 5 and 10 Bragg-layers in both frames are shown by the black solid lines as a guide to the eye. We find single-peaked PL spectra for QWs inside cavities with 1-4 Bragg layers. Between 5 and 7 layers, the PL becomes strongly non-Lorentzian. The PL eventually bifurcates into two peaks corresponding to the typical normal-mode splitting [82] for more than 8 Bragg-layers. At the same time, the mode function develops a pronounced cavity resonance (Fig. 6.5b).

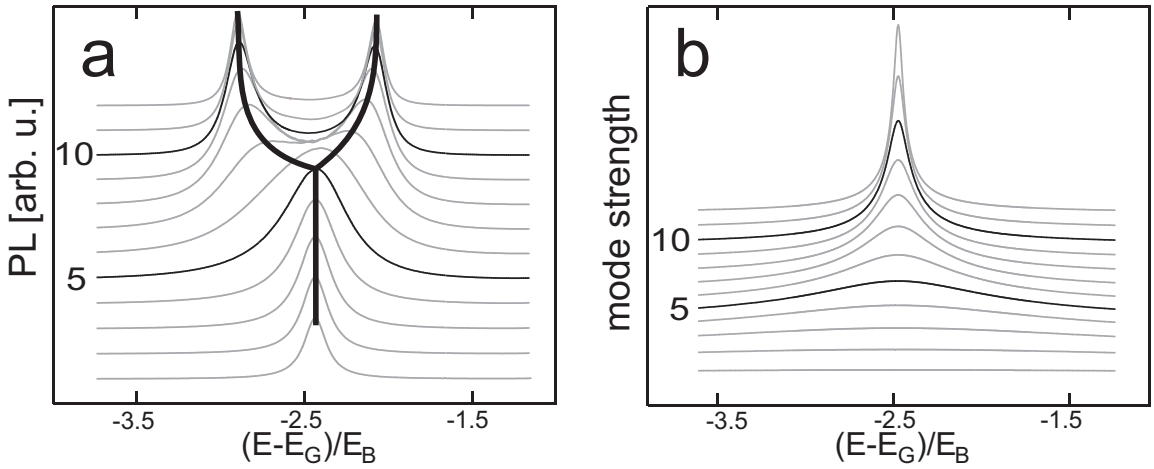

Figure 6.5.: *Normal mode splitting:* Frame a shows the PL spectra for cavities with different number of Bragg layers. The spectra related to DBRs with 5 and 10 Bragg-mirrors are indicated in black. The peak positions are marked by the black vertical lines to emphasize the normal-mode splitting. Frame b shows the absolute value of the mode function for the same cavities as in frame a.

In order to test the applicability of the EFFA, we analyze in Fig. 6.6a the energetic half width γ_{cav} of the cavity resonance (black triangles) as a function of the number of Bragg layers and compare it to the radiative decay constant (gray squares) obtained from Eq. (6.14). We observe that Γ_{rad} increases with the number of layers in the DBR, i.e. with the increase of the mirror reflectivity. This enhancement of radiative decay is obviously related to the Purcell effect. We now notice that Γ_{rad} and γ_{cav} become roughly equal when six layers are used.

The central peak position of the PL spectra shown in Fig. 6.5a is plotted in Fig. 6.6b for the cavities with up to 7 Bragg layers and compared against the EFFA. The results of the full computation are presented by the black triangles and the results from the EFFA are depicted as gray squares. We notice now that in the full computation the

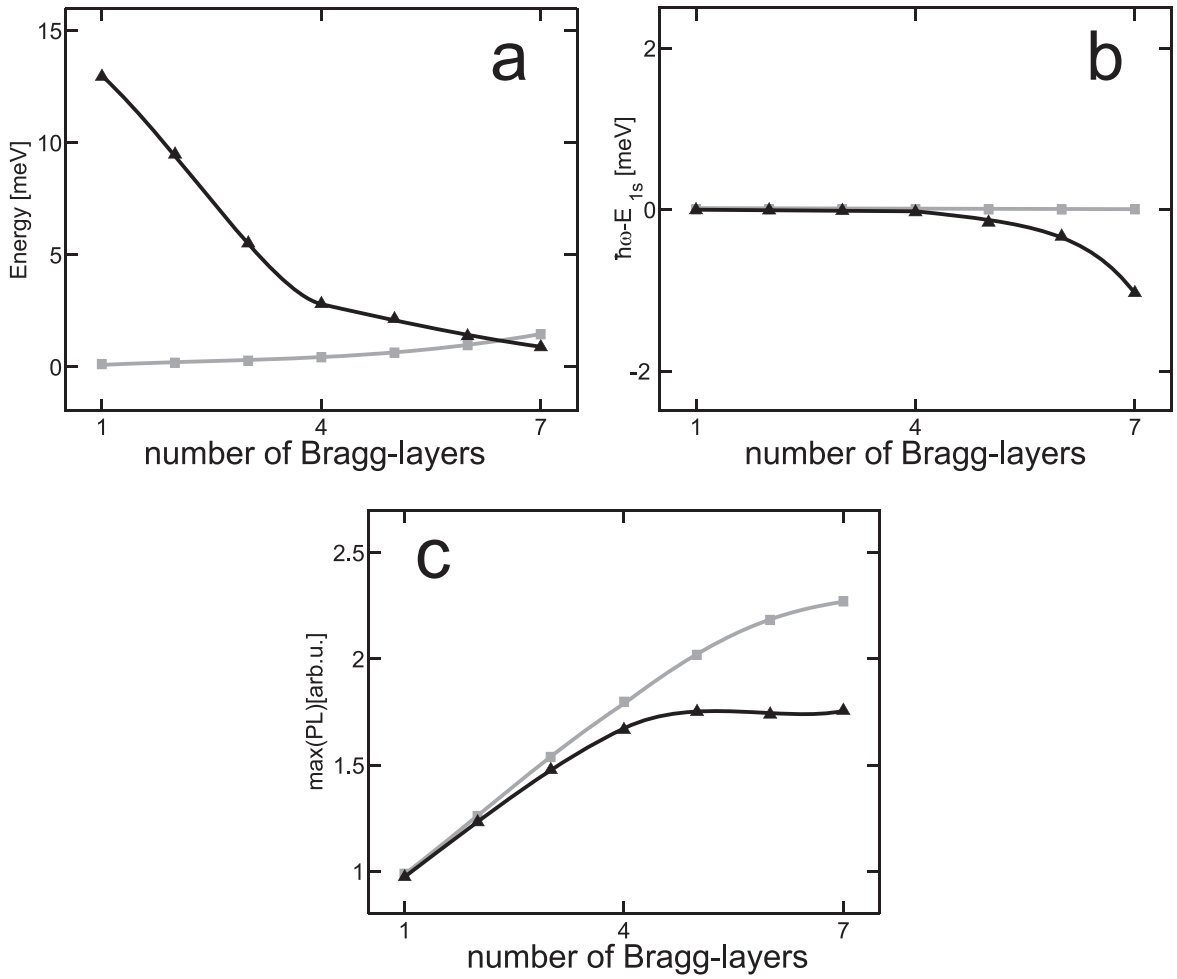

Figure 6.6.: *Comparison of QW-microcavity PL:* full computation vs. extended filter-function approach. a) The radiative decay constant (gray squares) evaluated from Eq. (6.14) and the half-width of the cavity mode (black triangles) are presented as a function of the number of Bragg layers in the DBR mirrors. b) Position of the PL peak evaluated using the extended filter-function approach (gray squares) compared to the full PL (black triangles). c) Comparison of the maximum PL computed by the full SLE (black triangles) and the maximum PL using the extended filter-function approach (gray squares). The triangles and the squares are connected via lines as a guide to the eye.

onset of the normal-mode splitting leads to a shift of the maximum PL for 5 to 7 Bragg layers due to the strongly non-Lorentzian peak shape. At the same time, we see that the EFFA describes the PL peak positions correctly for structures with up to four layers. To demonstrate more clearly the accuracy of the EFFA, we also compare the maximum PL intensity obtained using the extended filter-function result and the full PL. As shown in Fig. 6.6c, the maximum PL of the full computation and the EFFA agree rather well for structure with up to about four layers while clear deviations appear for layer numbers

greater than five. Obviously, the breakdown of the EFFA coincides with the regime where Γ_{rad} starts to exceed γ_{cav}. Thus, we conclude that the *EFFA approach works as long as the radiative broadening of the exciton resonance remains lower than the half width of the mode-function resonance.*

6.6. Comparison between experiment and theory

In the previous sections, we have derived the EFFA and investigated under which conditions the approximation is valid. We found that the EFFA is appropriate as long as the system is in the weak coupling regime.

In this section, we compare the numerical results of the EFFA with experimental PL spectra for a MQW system that is embedded inside a complicated dielectric environment. As we will see later in Chap. 7, the MQW structure adds some new features to the light-matter coupling that cannot be obtained in single-QW systems. These features strongly depend on the number of the QWs and their precise spacing with respect to the resonance wave length. They modify the observed PL spectra, such that in general the filter function derived for single-QW systems does not hold for MQW systems. Additionally, the SLE (5.4) show that the same terms that are responsible for the coupling between QW and dielectric environment introduce also coupling among the QWs. Thus, the strength of the QW coupling in principle depends on the exact dielectric structure and the position of the QWs therein.

However, for large homogeneous broadenings as they are typically obtained in laser structures at moderate to high carrier densities and at room temperature, the MQW coupling can often be neglected. In this limit, we can assume the QWs to be uncoupled such that a filter function can be determined for each QW separately according to Eqs. (6.11) and (6.12). The total filter function can then simply be derived from the averaging over the single-QW filter-functions

$$F_{tot}^{L/R} = \frac{1}{N} \sum_{m=1}^{N} F_m^{L/R}, \tag{6.16}$$

where N is the number of QWs and $F_m^{L/R}$ is the filter function belonging to QW m.

In order to test this approximation, we compare the numerical results for the MQW filter function (6.16) against an experiment. The investigated structure is a 14-QW sample depicted in Fig. 6.7a. The shaded area shows the refractive-index profile while the black vertical lines indicate the QW positions. The red (blue) line depicts the (counter-)propagating mode resonant with the 1s exciton.

Frame b shows the free-space spectrum as a black line. The colored lines are the measured edge-PL that is emitted almost parallel to the QW planes. In this direction there are no steps in the refractive-index profile such that the measurement directly corresponds to the free-space emission. The colors blue, red and green correspond to the different spot radii 3 mm, 8 mm and 13 mm, respectively. The respective lattice temperature is 275 K.

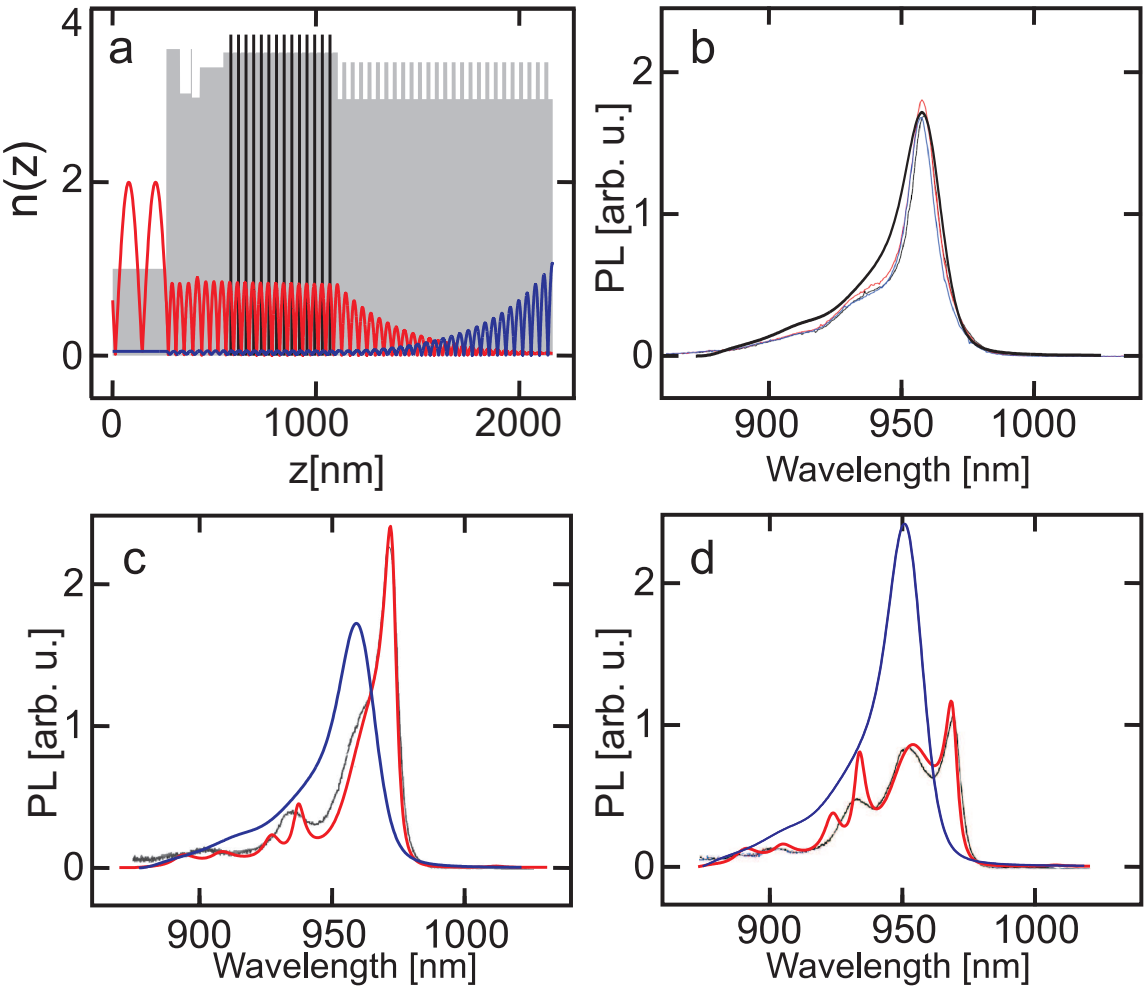

Figure 6.7.: *Test of the filter function: experiment vs. theory* Frame a shows the refractive index profile as a shaded area. The positions of the QWs are indicated by vertical black lines while the red and blue lines show the propagating and the counter-propagating mode that are resonant with the 1s-exciton energy. Frame b shows the experimental edge PL that is emitted almost parallelly to the QW planes as lines of different colors corresponding to different spot radii. The black line indicates the calculated edge PL. The two bottom frames show the surface PL that is emitted perpendicularly to the QW planes at temperature 275 K (left) and 300 K (right). The black curves indicate the experimental results while the red lines show the numerical evaluation using the filter function ind multiplying it on the edge PL. The blue lines show the numerically evaluated edge PLs. *The measurement was performed in the group of H.M Gibbs and G. Khitrova, Tucson; the edge PL was computed by the group of J.V. Moloney, Tucson*

The two frames c and d show the surface-PL that is emitted perpendicular to the QW planes and thus modified by the dielectric environment. Frame c shows the 275 K

result while the same results for 300 K are depicted in frame d. In both frames, the black line shows the experimentally measured surface PL, while the red line shows the PL that is observed by multiplying the total filter function (6.16) with the edge PL. The respective edge PL spectra are shown as blue curves. The difference between the results for the two temperatures is mainly caused by the band-gap shift that leads to a shift of the free-space PL such that the maximum of the free-space PL coincides with different parts of the filter function. For both temperatures, we find good agreement between experiment and theory.

7. Multiple quantum-well luminescence and exciton lifetimes

In the previous chapter, we have concentrated on the PL of a single QW and have investigated how the PL spectra are changed due to the dielectric environment of the QW. We found that we can describe the environment of a single QW system in the weak coupling regime via a filter function that is multiplied by the free-space emission of the QW.

In this section, we concentrate on the radiative coupling of a MQW system which often shows a multitude of intriguing effects that cannot be obtained in single-QW structures. For example, a periodic and parallel alignment of two or more QWs can lead to superradiance [86–89], solitons [90–92], the splitting of emission peaks [93, 94], and modified Rabi intersubband oscillations [95, 96].

The origin of these effects is the optical coupling between the QWs which is caused by the virtual emission and re-absorption of photons within the MQW system. The strength of the coupling depends on the spacing between the QWs and in general is strongest for Bragg structures, i.e. for QW spacings equaling one half of the wavelength of the 1s-exciton resonance [97]. Consequently, we investigate the quantum emission of MQW Bragg-structures and compare their emission to the PL of a single QW in Sec. 7.1. We will also investigate the size and nature of the PL modifications as a function of the QW number.

In Sec. 7.2, we analyze the influence of the modified emission properties on the lifetime of excitons. The exciton lifetime is of considerable interest because single-QW systems show a fast recombination of carriers that leads to a rapid decay of low-momentum excitons on a 10-ps time scale [55, 57, 98]. This property is clearly undesirable in many situations, e.g., when Bose-Einstein condensation is pursued [13]. Therefore, it is interesting to search for situations where the lifetime of the low-momentum excitons is enhanced and their recombination is suppressed. Thus, it will be one of our goals to determine which conditions optimize the radiative recombination process with respect to the exciton lifetime. Finally, we show in Sec. 7.3 how an exciton population can be created due to the PL emission of radiatively coupled QWs.

7.1. Subradiance

Most of the results that we will discuss in Secs. 7.1–7.3 have been published in Ref. [85]. The argumentation is therefore kept close to that paper. In order to get a first clue of the MQW-coupling effects, we analyze how the luminescence per QW is influenced by

the number of QWs in the system. More specifically, we compare the single and 16 QW PL by solving the corresponding steady-state luminescence I^{PL} from (5.2), (5.4), and (5.12) when only an uncorrelated electron-hole plasma is present, i.e. when the exciton populations are vanishingly small. For this situation, we may neglect the carrier-recombination dynamics because it happens on a ns time scale, which is slow compared to the ps time scale we are investigating here. We assume a carrier density of $n = 8{\cdot}10^8$ cm^{-2} in thermal equilibrium and a carrier temperature of $T = 77$ K in a GaAs QW-structure. Thus, we are in the low density regime and use a homogeneous broadening with $\gamma = 0.05E_B$.

In order to compare the single and 16 QW photoluminescence, we define a normalized luminescence per QW

$$I_{\mathrm{norm}}(\omega) \equiv I^{PL}(\omega)/N \; . \tag{7.1}$$

Figure 7.1 shows $I_{\mathrm{norm}}(\omega)$ for a single QW (shaded area) and for MQW systems consisting of 16 QWs with a QW separation $\Delta s = \lambda/4$ (dashed line) and $\Delta s = \lambda/2$ (solid line), respectively. The PL per QW is plotted as a function of the energy of the quantum emission. The energy is given relatively to the unrenormalized band gap energy, which is denoted by E_G. We observe that the emission per QW is strongly reduced in MQW systems. This effect is referred to as *subradiance*.

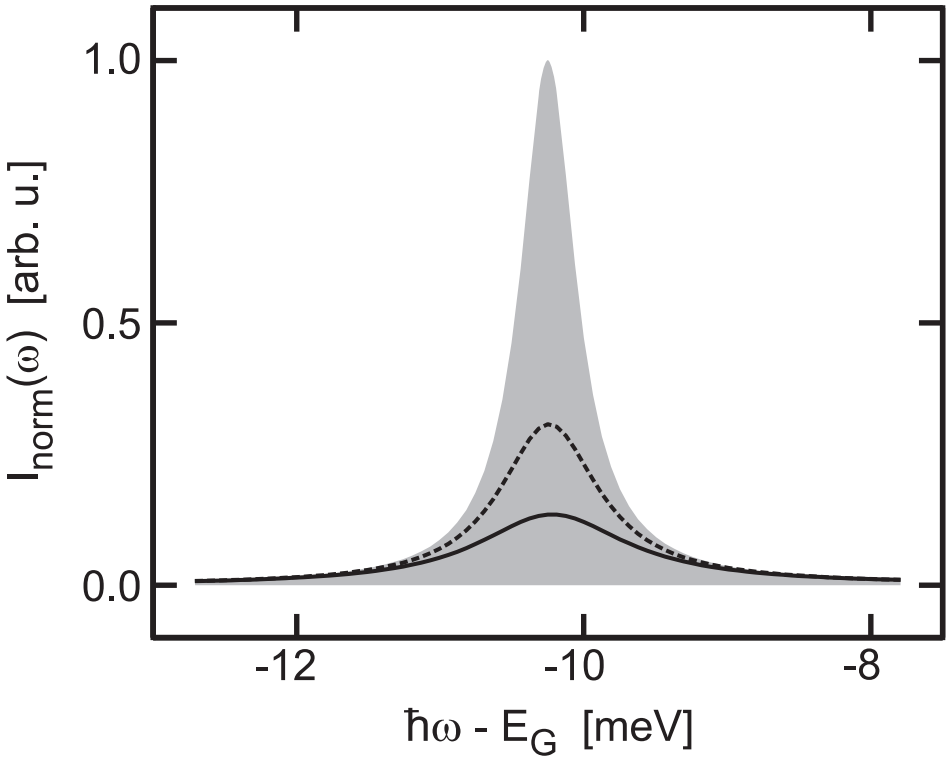

Figure 7.1.: Steady-state spectra of the luminescence per QW for a single QW (shaded area) and systems of 16 QWs with spacings $\lambda/2$ (solid line) and $\lambda/4$ (dashed line). For these computations, we use $T = 77$ K carrier temperature and a Fermi-distributed carrier density of $8 \cdot 10^8$ cm^{-2}.

As a general trend, subradiance is strongest for the Bragg structures. Any detuning of the spacing away from the Bragg-condition leads to a weakening of this effect. The subradiance has a minimum for the QW separation $\lambda/4$ (anti-Bragg spacing) if the number of QWs in the system is even. For odd QW numbers, the minimum is also in the vicinity of the $\lambda/4$ separation but the exact value depends non-trivially on the number of QWs. To have maximally suppressed radiation, we mostly concentrate on Bragg-structures in the following. If the carrier density is large, the QWs display gain and the coupling effects produce superradiance as shown in Ref. [34]. The overall behavior of the emission is clearly different from the decay of the coherent polarization for which the radiative coupling effects produce a superradiant behavior in Bragg-structures regardless of the carrier density [88]. This difference is a consequence of the fact that the broadening of the coherent spectrum corresponds to a faster (i.e. superradiant) decay of populations whereas the broadening of the spectrum in Fig. 7.1 is related to the dephasing of Π. The area under the curve determines the total PL.

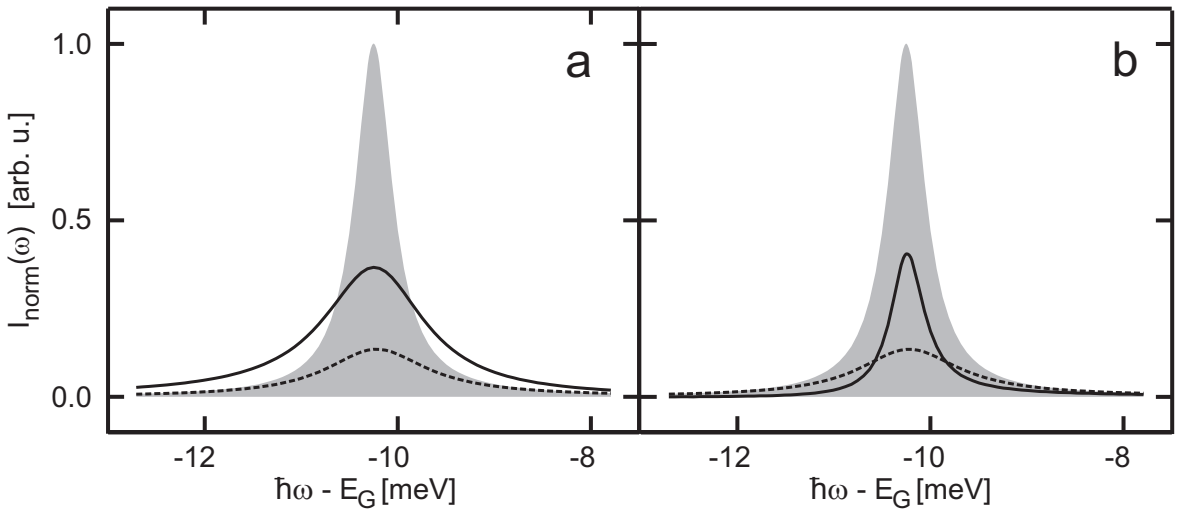

Figure 7.2.: *Origin of subradiance:* Steady-state spectra for the luminescence per QW showing the result of a full computation for a single QW (shaded area) and a system of 16 QWs with spacing $\lambda/2$ (dashed line) as well as the results of a system of 16 QWs where only the stimulated contribution is included and the recombination-correlation is neglected (solid line in subfigure a) and an analogous system where the recombination correlation is included and the stimulated contribution is neglected (solid line in subfigure b). The carrier temperature is $T = 77$ K and we use a Fermi-distributed carrier density of $8 \cdot 10^8$ cm^{-2}.

In order to pinpoint the origin of the subradiance, we have to identify the terms which are responsible for the QW coupling. In Eq. (5.4), the only terms which couple different QWs are the recombination correlation Ω_m^{RC} and the stimulated contribution $\Omega^{ST} \equiv \Delta\langle B^\dagger_{\mathbf{q}_\parallel,q_\perp} B_{\mathbf{q}_\parallel \Sigma_m}\rangle$. We perform a switch-off analysis to investigate the relevance of these two terms for the subradiance of a 16-QW system. In Fig. 7.2 we compare

the results of a full calculation for a single QW with that of a system of 16 QWs with spacing $\lambda/2$. Additionally, we show in Fig. 7.2a the result of e calculation for 16 QWs where only Ω^{ST} is included. In Fig. 7.2b, we present the result of a computation where we kept only the Ω_m^{RC} term. The comparisons in Fig. 7.2 indicate that the stimulated emission term leads to a smaller but broadened resonance peak compared to the single QW result. This effect is clearly analogous to the broadening of a coherent spectrum under superradiant conditions. However, the area under the peak, which determines the total number of emitted photons, remains unchanged. If we only include Ω^{RC} we do not observe a broadening of the resonance but a depletion of the luminescence per QW, i.e. the area under the peak is strongly diminished compared to the single QW emission. Therefore, we conclude that the recombination correlations are dominantly responsible for the subradiance effects.

Since subradiance is a QW coupling phenomenon it is interesting to see how the strength of the subradiance depends on the number of QWs in the Bragg structure and how Ω^{RC} effects the subradiance. Consequently, we compare the luminescence per QW $I_{\mathrm{norm}}(\omega)$ in the three cases including: i) the full SLE, ii) the stimulated contribution only, and iii) the recombination correlation only. We perform this comparison for Bragg-structures with 1 to 10 QWs and use the same parameters as in the computations before. The results of this analysis are shown in Fig. 7.3 where the full calculation (solid line) is compared with computations with only Ω^{ST} (dashed line) and Ω^{RC} (dotted line). We observe that the area under the PL peak decreases with increasing QW number, i.e. the radiance is increasingly suppressed.

7.2. Exciton lifetime in multiple quantum-well systems

As we have seen, MQW systems may lead to the suppression of incoherent emission. As a consequence, an excitations of the system should exhibit an enhancement of its lifetime. In the following, we consequently investigate the influence of the MQW structure on the lifetime of bright excitons. In single-QW systems, the radiative lifetime of coherent excitons, i.e. the square of the polarizations in the classical limit, and the radiative lifetime of bright excitons in the incoherent limit are the same due to the identical structure of the SBE and the SLE. Hence, one finds the radiative lifetime of bright excitons in a single QW to be $\tau_1 = \hbar/(2\Gamma_{rad})$. The origin of the radiative decay is the recombination of optically active exciton populations, which happens rapidly on a 10-ps time scale. This fast recombination efficiently removes excitons at low momentum states. As a result, the exciton distributions show strong nonequilibrium characteristics [20, 66, 68] around $\mathbf{q}_{\parallel} = 0$.

As another general feature, one finds [34] a strict conservation law

$$I^{PL} = \frac{\partial}{\partial t} \sum_{q_\perp} \Delta \langle b^\dagger_{0,q_\perp} b_{0,q_\perp} \rangle = \frac{\partial}{\partial t} \sum_{\mathbf{k}_\parallel} f^{e,h}_{\mathbf{k}_\parallel} \,, \tag{7.2}$$

which implies that the number of recombined electron-hole pairs equals the number of emitted photons. When the MQW system reduces the total I^{PL} due to subradiance, one

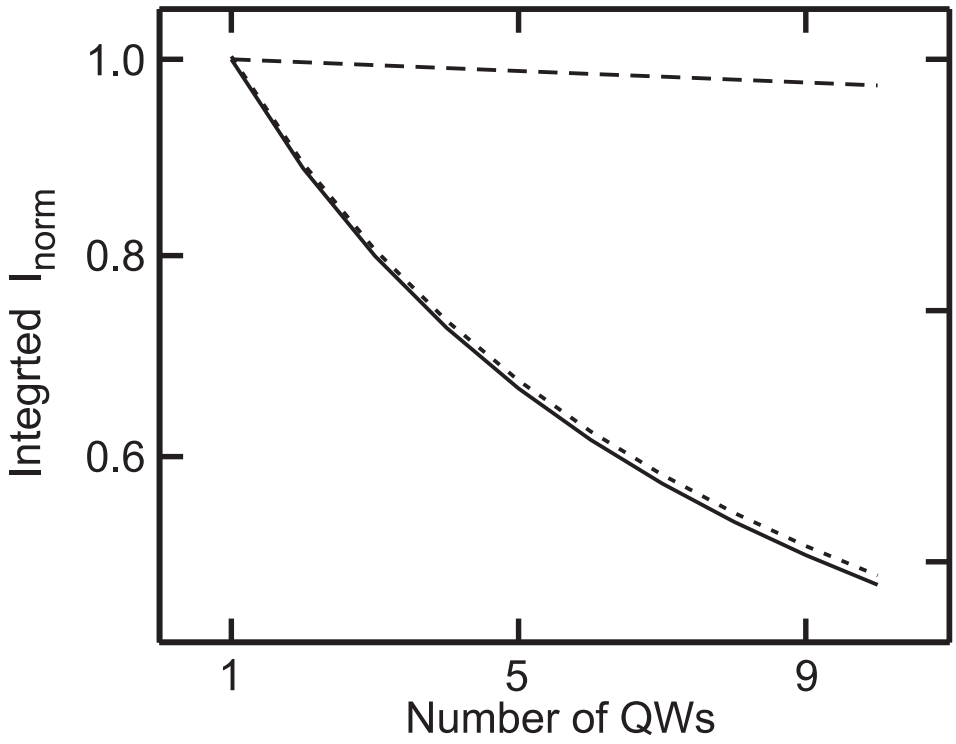

Figure 7.3.: *Strength of subradiance vs. number of QWs:* Comparison of the integrated luminescence per QW using the full SLE (solid line) to the cases with including only $\Delta\langle B^{\dagger}_{\mathbf{q}_\parallel,q_\perp} B_{\mathbf{q}_\parallel \Sigma_m}\rangle$ (dashed line) or Ω^{RC} (dotted line) for different numbers of QWs. Carrier temperature and density were kept the same as in Fig. 7.2.

simultaneously obtains an enhanced optical lifetime of excitations in the system. Thus, it is interesting to study whether one can apply the subradiance to tailor the radiative lifetime of quasi particles in semiconductors. The aim here is to determine how one can maximally enhance the exciton lifetime in a MQW system.

We know from the investigations in the previous section that the subradiance becomes stronger for a larger number of QWs. For that reason, we analyze the influence of the number of QWs on the radiative lifetime of excitons in a Bragg structure by solving Eqs. (5.2), (5.4), (5.12), (5.15), and (5.16). We initially insert a certain number of excitons into each QW. The carrier density is set to $8 \cdot 10^8$ cm^{-2} and the exciton density is $7.36 \cdot 10^8$ cm^{-2} (exciton fraction is 92%) such that nearly all carriers occur as a part of an exciton. The carrier temperature and the homogeneous broadening remain unchanged compared to the previous analysis. The results of this investigation are presented in Fig. 7.4 where the exciton lifetime is plotted against the number of QWs for MQW systems with 1 to 10 QWs. The solid line shows the results obtained from the full numerical analysis while the shaded area corresponds to the lifetimes computed with the help of a simplified analytical model discussed in appendix C. For the analytical investigation, we use the known exciton lifetime τ_1 in a single QW and the result for

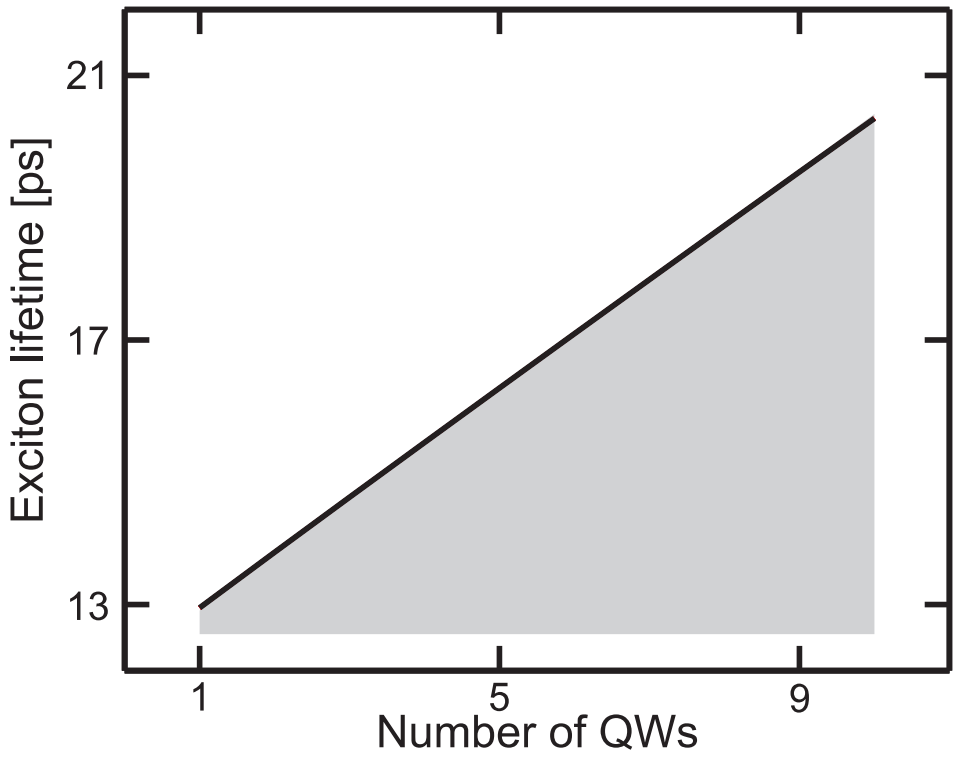

Figure 7.4.: Excitonic lifetime computed in different Bragg-structured MQW-systems. The solid line shows the full numerical result. The shaded area is obtained from a linear extrapolation of the exciton lifetime for 1 and 2 QWs.

the exciton lifetime of a 2-QW system calculated by the simplified model. We compute the difference between the lifetimes in these two systems and assume a linear lifetime increase with increasing QW number,

$$\tau_N = \tau_1 + (N-1)\Delta\tau_{12} \quad , \tag{7.3}$$

where

$$\Delta\tau_{12} = \tau_1 \frac{\sqrt{\gamma^2 + 4\Gamma^2} - \gamma}{\gamma + 2\Gamma - \sqrt{\gamma^2 + 4\Gamma^2}} \, . \tag{7.4}$$

Figure 7.4 shows that the lifetime of the full numerical computation rises linearly with increasing QW number. We find that the increase of the exciton lifetime is roughly 0.834 ps per additional QW for the homogeneous γ used in the computations. Furthermore, the simplified model reproduces the lifetimes of the full numerical model very well, although the corresponding analytic calculation only includes exciton contributions. The linear increase of the exciton lifetime with increasing number of QWs corresponds directly to the increase of the subradiance effect. From these observations, we conclude that the suppression of the photon emission results in an enhancement of the radiative lifetime of excitations in the system. For cases other than $\lambda/2$ spacing, one cannot determine a

single decay constant or an exciton lifetime since the decay dynamics consists of several modes with different decay constants.

Besides the number and the spacing of the QWs, the simple formula (7.4) predicts that the chosen homogeneous broadening of the photoluminescence affects the exciton lifetime. In realistic experiments one can alter γ via the lattice temperature and/or the background carrier-density since γ depends on phonon and Coulomb scattering. Note that the dependence of the exciton lifetime on the homogeneous broadening is introduced by the dephasing constant in the equation of motion for the correlated electron-hole pairs in Eq. (5.21). Even though the decay constant is used for off-diagonal exciton correlations only, it influences the radiative decay of diagonal exciton populations via Ω^{RC}. In the following, we analyze this influence for systems of 10 QWs with Bragg spacing by varying γ for the same carrier and exciton densities as already used in Fig 7.4. The carrier temperature is $T = 77$ K and the radiative broadening is $\Gamma = 0.025$ meV. In Fig. 7.5, we show the exciton lifetimes in units of the radiative exciton lifetime in

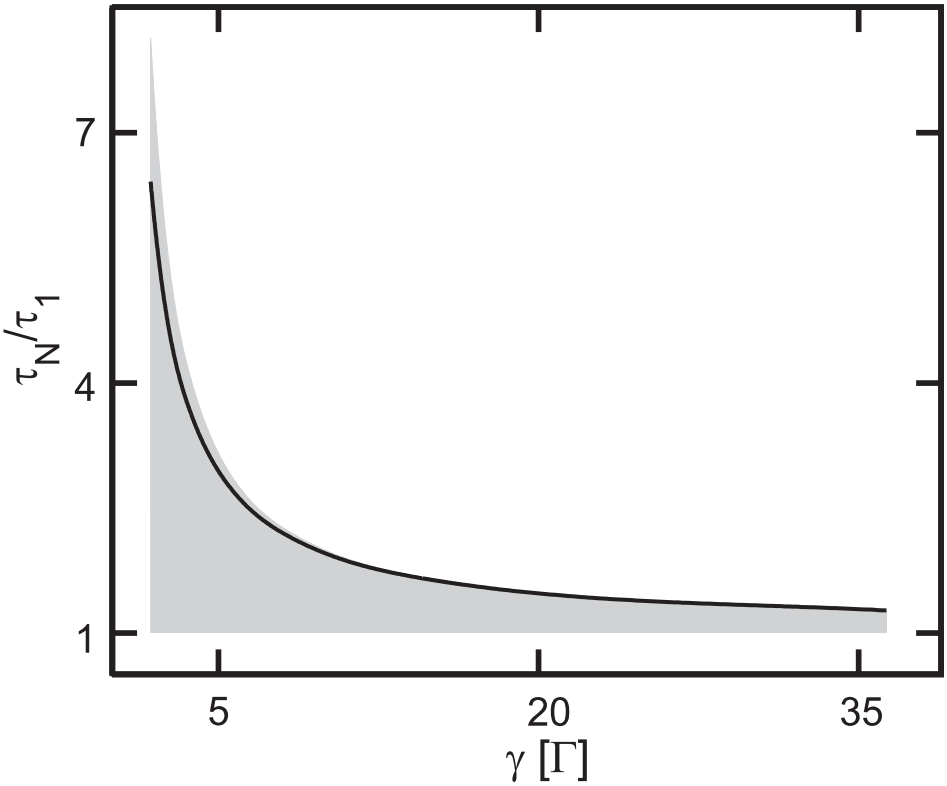

Figure 7.5.: Exciton lifetime computed for different dephasing constants in Bragg structures with 10 QWs. The solid line shows the full numerical result. The shaded area is the result gained from the analytical approximation presented in the Appendix C.

a single QW. Thus, we compare the results of the full numerical analysis (solid line) against the radiative lifetimes gained by using Eqs. (7.3) and (7.4) (shaded area). We find that the lifetime increase becomes stronger for small γ, e.g. we obtain a lifetime of

about 76.6 ps for a Bragg structure with 10 QWs and $\gamma = 2\Gamma$. For large γ, the QWs become uncoupled such that one recovers the single-QW exciton lifetime of about 13 ps. The simplified model predicts the full numerical results very well. For small γ, Eq. (7.4) slightly overestimates the radiative lifetime increase. This deviation can be explained by additional super- and subradiant modes which occur in a 10 QW system and alter the result slightly for small γ. In a two-QW system these modes are absent and thus are not taken into account in the simplified analytical model.

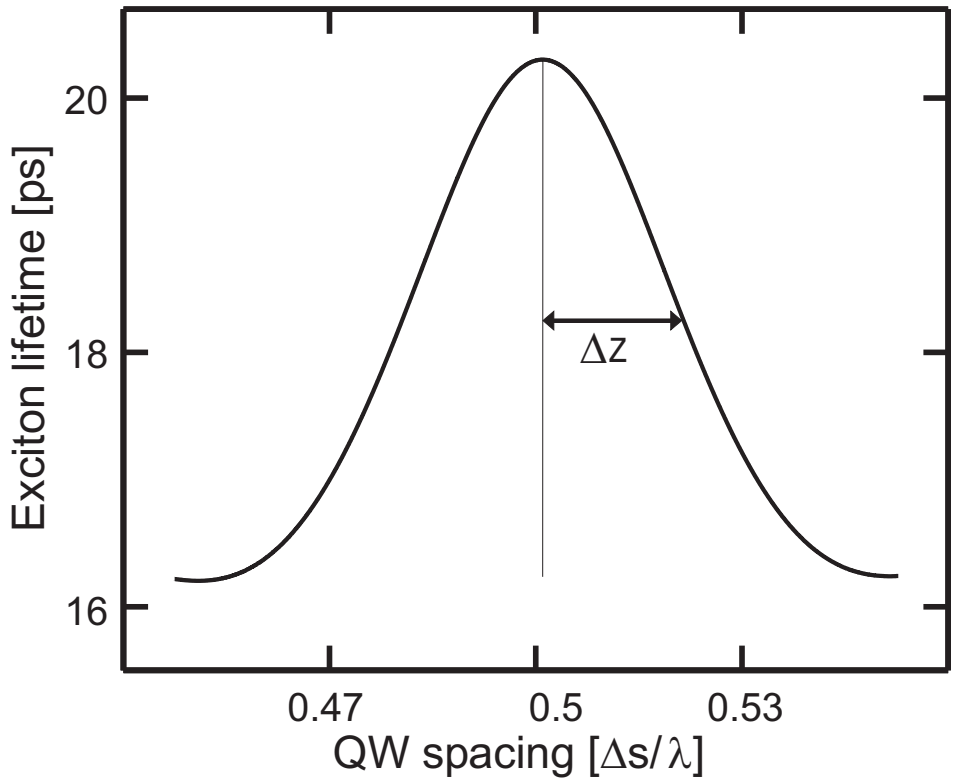

Figure 7.6.: Exciton lifetime for different QW spacings in a system of 10 QWs. The half width of the resonance around the Bragg-condition is denoted by Δz.

In Fig. 7.1, we have already shown that the influence of the subradiance is strongest for the Bragg condition. We next investigate the robustness of this subradiance by tuning away from the Bragg spacing. For this purpose, we use the same parameters as in Fig. 7.4 and plot in Fig. 7.6 the exciton lifetime for a 10 QW system as a function of the spacing. As suggested from the subradiance results, the exciton lifetime is largest for systems where the QW spacing is around $\lambda/2$. Interestingly, we find the maximum lifetime increase at a QW spacing that slightly differs from the exact value of $\lambda/2$. This deviation is a consequence of the emission from exciton populations in states other than the 1s state since photons from different exciton states have different energies. Thus, the Bragg conditions for these photons is satisfied at different spacings for emission from different exciton states.

In order to compare the sensitivity of the lifetime enhancement to the detuning in

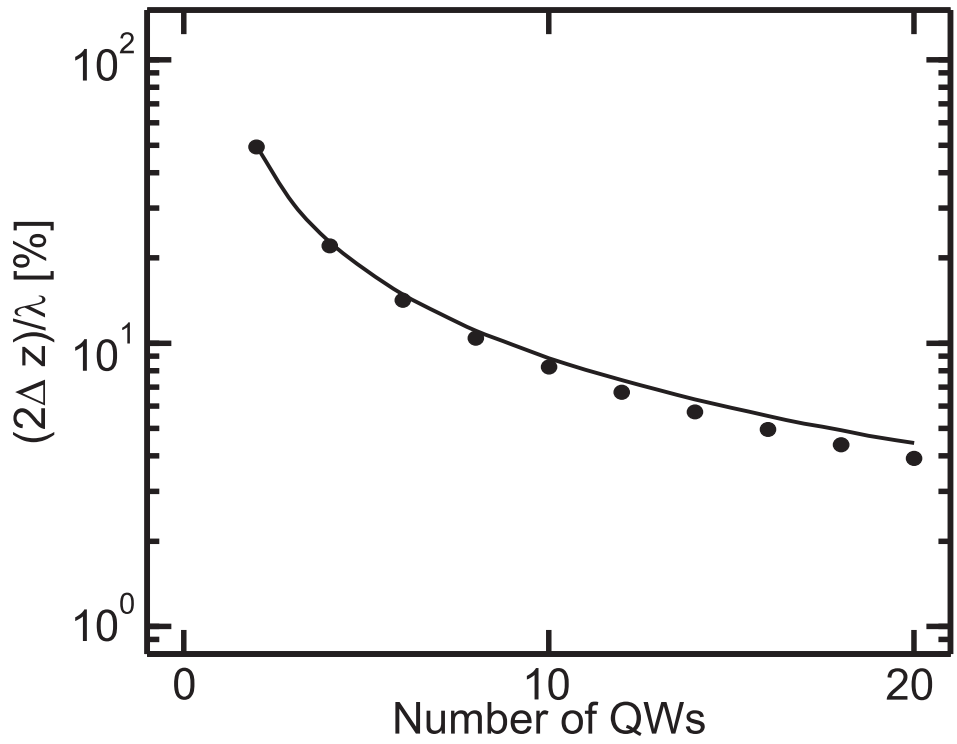

Figure 7.7.: Half width of the lifetime peak around the Bragg-condition for QW arrangements with 2 to 20 QWs. The solid line shows the result gained from Eq. (7.5) while the filled circles show the full numerical analysis.

different MQW structures, we define Δz to be the half width of the lifetime Bragg-resonance, as indicated in Fig. 7.6. Additionally, we use a simplified model for the SLE introduced in the Appendix of Ref. [34] and extend it, such that exciton populations are taken into account. This analysis allows us to deduce the half width of the Bragg-resonance analytically from

$$\frac{\sin(\mathrm{N}q_{1\mathrm{s}}\Delta\mathrm{z})}{\sin(q_{1\mathrm{s}}\Delta\mathrm{z})} = \frac{N}{\sqrt{2}}\,, \tag{7.5}$$

where q_{1s} is the photon momentum corresponding to the energy of the exciton-resonance energy. The number of QWs is denoted by N. The first root of Eq. (7.5) defines Δz. The result obtained from this formula (solid line) is compared with the full numerical computation (filled circles) for QW arrangements with 2 to 20 QWs in Fig. 7.7. We observe that the computed half widths excellently agree with those calculated by the numerical analysis of the SLE. Additionally, we find that the shape of the lifetime peak is broad for a small number of QWs and quickly gets sharper for higher numbers of QWs.

7.3. Exciton pumping

So far, we have demonstrated that the exciton lifetime is strongly influenced by the radiative coupling between different QWs. Since spontaneous emission has its maximum at the exciton resonance, even without the presence of exciton populations [18], one might ask if this emission lead to exciton generation in MQW systems. Hence, it is interesting to investigate whether even plasma excitation conditions and plasma luminescence may lead to the formation of excitons indirectly via radiative coupling. To analyze this basic phenomenon, we study a Bragg structure of two radiatively coupled QWs. We assume that the first QW has an initial carrier density of $3 \cdot 10^{10}$ cm^{-2}, while the other QW is unexcited. Additionally, we assume that no exciton populations are present in the beginning. The temperature is chosen to be $T = 20$ K and the carrier

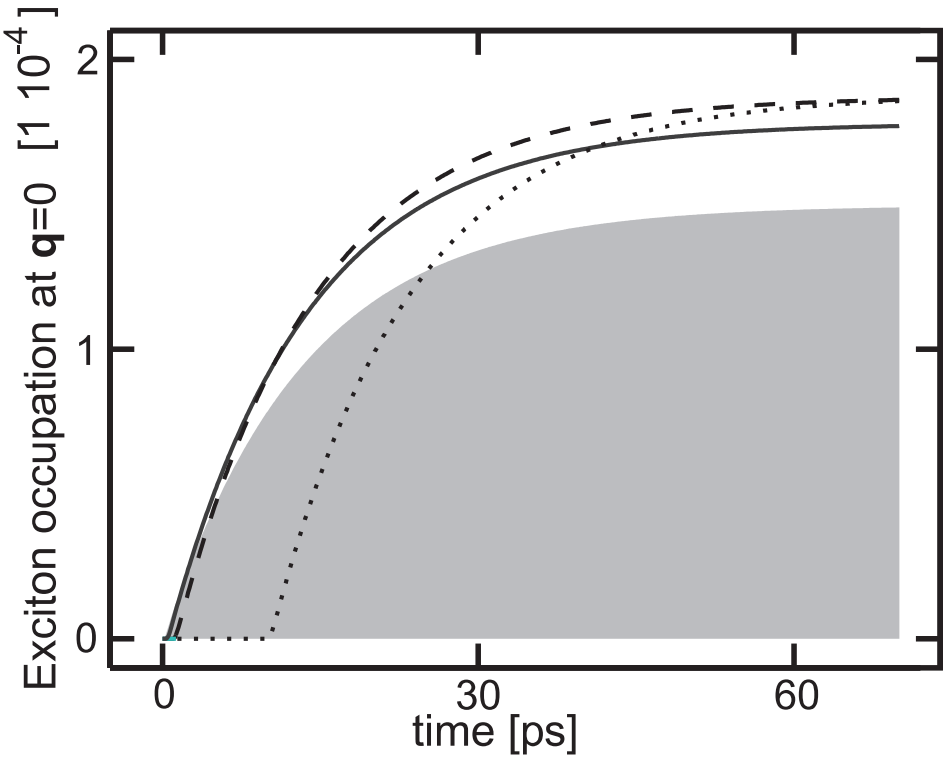

Figure 7.8.: Excitation of excitons in two radiatively coupled QWs. The first QW is assumed to be populated by a Fermi-distributed carrier density of $3 \cdot 10^{10}$ cm^{-2}, while the second QW is initially empty. In the beginning there are no excitons in neither of the two QWs. The exciton occupation at $\mathbf{q}_{\parallel} = 0$ in the second QW is depicted as a function of time for the four different QW spacings with 1.4fs $\simeq \lambda/2$ (shaded area), 0.315 ps (solid line), 1 ps (dashed line) and 10 ps (dotted line) propagation time between the QWs.

density in the first QW follows a Fermi distribution. Due to the relatively high density in the first QW, the homogeneous broadening is chosen to be 2.1 meV, according to computation of excitation induced dephasing [20]. Since the 2nd QW is empty, we use

a lower homogeneous broadening of 0.42 meV there. In Fig. 7.8, the exciton occupation at $\mathbf{q}_{\parallel} = 0$ for different spacings between the two QWs is presented. The shaded area shows the case where the two QWs are separated by only $\Delta s = \lambda/2$ which corresponds to a 1.4 fs time delay in the light propagation between the QWs. We have also tested other QW distances consisting of integer multiples of $\lambda/2$. The cases where the spacing corresponds to roughly 0.315 ps (solid line), 1 ps (dashed line), and 10 ps (dotted line) are also shown in Fig. 7.8. The exciton distribution at $\mathbf{q}_{\parallel} = 0$ in the second QW reaches values of about $1.86 \cdot 10^{-4}$ which corresponds to an exciton density of about $7.5 \cdot 10^4$ cm^{-2}. This is not a very high population, but it demonstrates the fundamental possibility that pure plasma excitations are able to pump excitons in radiatively coupled QWs. The obtained maximum level of pumped excitons can be enhanced considerably by increasing the carrier density in the first QW.

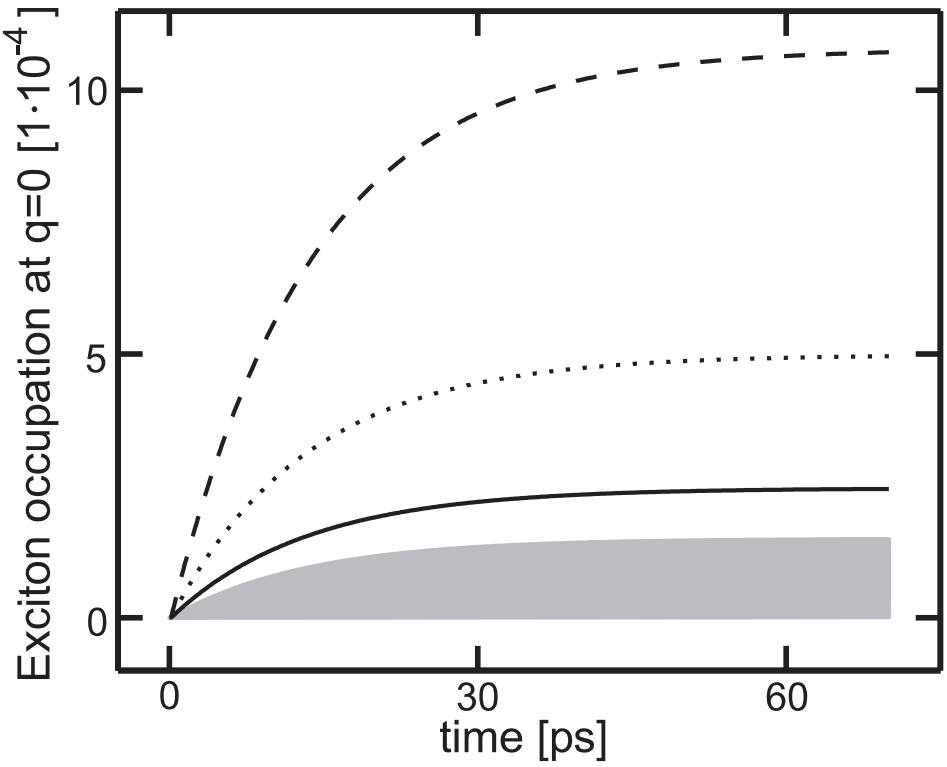

Figure 7.9.: Exciton occupation at $\mathbf{q}_{\parallel} = 0$ of an initially unexcited QW in Bragg-structures with 2 (shaded area), 3 (solid line), 5 (dotted line) and 10 (dashed line) QWs. The other QWs are initially populated by a Fermi-distributed carrier density of $3 \cdot 10^{10}$ cm^{-2}.

Additionally, we obtain a slight increase in the amount of created excitons for larger QW spacing. This increase stops for QW separations leading to a larger than roughly 0.32 ps delay time, which at the same time matches the dephasing time $\tau_\gamma = \hbar/\gamma = \hbar/(2.1\text{meV})$ of the pumping QW. The radiative coupling between QWs is limited by τ_γ, since the QWs become radiatively uncoupled once the QW separation exceeds the spacings corresponding to τ_γ. The homogeneous dephasing in the initially empty QW is

much smaller than γ in the pumping QW and therefore its contribution to this effect is only weak.

An interesting feature of the excitons in the second QW is that all excitons exclusively populate the state of $\mathbf{q}_{\parallel} = 0$. Detailed investigations [66] show that the excitons in this state show long-range order and reduced phonon and Coulomb scattering. Hence, the excitons are generated in a quantum-degenerate state, i.e. an exciton condensate.

In order to find out whether more plasma-excited QWs may influence the amount of created excitons in a radiatively coupled and initially empty QW, we compare the cases of 2, 3, 5 and 10 QWs with spacings $\lambda/2$. The last QW in all structures is initially empty while the other QWs are initially populated by a Fermi-distributed carrier density of $3 \cdot 10^{10}$ cm^{-2} each. The result of this comparison is shown in Fig. 7.9. The exciton occupation at $\mathbf{q}_{\parallel} = 0$ in the second QW of the system of two QWs is depicted by the shaded area. The solid line shows the corresponding occupation in the third QW of the 3-QW system. The cases of 5 and 10 QWs where the last QW is initially empty are presented by the dotted and the dashed line, respectively. From Fig. 7.9, we observe that the number of created excitons in the initially empty QW can be strongly increased by using more plasma excited QWs as a source. The amount of created excitons scales nearly linearly with the QW number.

8. Conclusion and outlook

In the framework of this thesis, we have applied and extended a microscopic theory that allows for a systematical treatment of the light-matter interaction effects in semiconductor heterostructures in the coherent and the incoherent light-emission regime.

In the first part of this thesis, we have concentrated on the coherent regime where we have investigated the optical response of a Gallium arsenide or a Germanium quantum well for different carrier densities. For the treatment of the carrier scattering in Germanium, we have derived a theory that allows us to describe scattering contributions due to electrons at the L-point. In Gallium arsenide, we have recovered the well known "excitation-induced dephasing". In particular, we found that the exciton resonances are broadened and bleached if the carrier density is increased. Additionally, the energy of the exciton resonance stays almost constant if carrier scattering beyond the Hartree-Fock approximation is used. Investigating the carrier scattering in Germanium quantum wells, we found that electrons at the L-point do not contribute to Pauli blocking and band-gap renormalizations. Thus, the L-point electrons enter only the description of the carrier-carrier scattering.

We have compared the numerical results for different amount of electrons at the L-point against measured absorption spectra for different time delays after the excitation. For the investigated carrier density, we found via peak-shape comparison that electrons which are excited close to the Γ-point scatter to the L-point on a 140-femptosecond time scale. Thus, transient gain could be obtained only for short times after the excitation. When more electrons scatter to the L-point the exciton resonance starts to recover. However, the holes stay at the Γ-point and thus contribute to Pauli blocking. Additionally, all carriers still contribute to the carrier scattering and therefore lead to polarization dephasing. As a consequence, the exciton resonance does not fully recover and the exciton remains partially bleached, even when all electrons have scattered to the L-point.

If the Germanium quantum wells are embedded inside a Silicon substrate, the L-point electrons may be excited into the continuum states of the substrate and act as absorbers for a wide spectrum of photon energies. Thus, a population of L-point electrons leads to the absorption of photons from the pump pulse as well as from radiatively coupled QWs. The strength of the absorption increases with the amount of electrons at the L-point such that a sufficiently large electron populatation at that point inhibits the observation of optical gain in Germanium-quantum-well structures. As a consequence, Germanium quantum wells cannot be used as optically active region in laser structures.

In order to include the dielectric environment into our theoretical description, we have reviewed a transfer-matrix method that describes the partial reflection and transmission due to boundaries corresponding to steps in the background refractive index.

The quantum-well response was expressed in terms of reflection, transmission and absorption such that the microscopic description of the quantum well could be included into the transfer-matrix calculations. The results of this combined theory have been compared to experiments and showed excellent agreement over a wide energy range when the frequency dependence of the refractive-index profile was taken into account.

In the second part of this thesis, we have concentrated on the incoherent light-emission regime, i.e. on photoluminescence. We have investigated mainly the coupling of a single quantum well to its dielectric environment and the coupling among the quantum wells in multiple-quantum-well structures.

Due to the quantum-mechanical treatment of the light field and the detection process, the dielectric structure enters the relevant photoluminescence equations non-trivially in multiple places. Thus, even small changes of the dielectric environment imply that the full, numerically tedious, incoherent dynamics has to be solved again. We have introduced an approximation that allows for treating dielectric environment and incoherent quantum-well emission separately. The free-space luminescence needs to be computed only once while the dielectric environment is described via a environment-dependent filter function. The luminescence of the actual structure is then gained by multiplying the filter function and the free-space luminescence.

We have shown that this approximation excellently reproduces the full semiconductor luminescence equation results if the radiative broadening caused by the stimulated contribution to the photon-assisted polarization can be neglected. When the contribution of radiative broadening to the total peak broadening becomes significant, the radiative contribution has to be taken into account in the free-space calculation. Thus, we have presented a method that allows to determine the radiative broadening of a single QW only via the known mode functions of the dielectric structure. The modification of the free-space luminescence can be performed via a convolution such that it is not necessary to re-compute the free-space semiconductor luminescence equations. This extended filter-function approximation excellently agrees with the full calculations for structures in the weak coupling regime and allows for efficient sample design. As an additional feature, the filter -unction approximation enables us to predict the emission under finite angles if the perpendicular luminescence is known.

The filter-function approximation fails in the strong coupling regime when normal-mode coupling effects occur. For these cases, the full semiconductor luminescence equations need to be solved. Finally, we have used the filter-function approximation to explain the measured luminescence spectra of a multiple-quantum-well system that is embedded into a complicated dielectric environment. We have found very good agreement between experiment and theory.

In the last part of this thesis, we have investigated the radiative coupling in multiple-quantum-well systems. We found that these systems show a suppressed luminescence per quantum-well compared to a single-quantum-well system. The origin of this suppression is the recombination correlation that describes correlated processes where an electron-hole pair combines while at the same time another electron-hole pair is created in another quantum-well. The second term that is responsible for the radiative quantum-well coupling is the stimulated contribution. It leads to an additional peak

broadening but does not deplete the luminescence.

Together with the suppressed emission, the excitations in multiple quantum well systems exhibit an enhanced lifetime. The strength of the enhancement generally depends on the number of QWs and their spacing as well as on the homogeneous broadening. We have found longest lifetimes for Bragg-structures with small homogeneous broadening corresponding to low carrier densities at low temperatures. Additionally, we have derived an analytical expression for the exciton lifetime in a Bragg spaced two-quantum-well structure. This formula can be used to extrapolate the lifetime in Bragg spaced N-quantum-well structures, as in these structures, the exciton lifetime increases linearly with the number of quantum wells.

We could show that exciton populations can be created by the quantum emission of radiatively coupled quantum wells. This is even the case when the luminescence originates from the recombination of uncorrelated electron-hole plasma and initial exciton populations are not present.

Even though the presented theory is able to describe a large variety of coherent and incoherent light-matter coupling effects, there are some natural extensions that could yield insights into new and intriguing effects.

One could for example improve the treatment of the carrier scattering. The inclusion of the principle value of the 2nd-Born scattering matrix would allow us to investigate the optical response at low carrier temperatures. Additionally, one could include the full coherent and incoherent correlations in Eq. (3.15). This would enable us to investigate the effects on the optical response if different correlations or populations are present. Observations like the blue shift of the exciton resonance in the presence of exciton populations could probably be explained. On top of that, the full inclusion of the correlations should also allow for investigating how different light statistics of the pump pulse effect the absorption. The application of the microscopical scattering in the incoherent regime allows for analyzing the polariton condensation in microcavities or soliton effects in multiple quantum well systems.

Another interesting task would be the investigation of the coupling of the Semiconductor Bloch Equations and the Semiconductor Luminescence Equations. The coupled equations could then be used to investigate the interplay between coherent quantities and incoherent correlations in regimes when both contributions are important. Together with an appropriate treatment of the phonon interaction, this coupled theory could describe the full sequence of the light-matter-interaction process on a microscopical level, starting with the coherent excitation, the scattering and relaxation processes, and finally the creation of correlations and the quantum-emission. The results gained from such a theory would provide deep insights into the nature of light statistics and quantum correlations.

A. Wannier equation and excitonic eigenfunctions

The Wannier equation is the Schrödinger equation for the relative-motion problem of an electron-hole pair. This problem is formally identical to the hydrogen problem and therefore leads to bound hydrogen-like states plus a continuum of ionized states. The bound electron-hole pairs are also called excitons. The corresponding Schrödinger equation in real space is given by

$$-\frac{\hbar^2\nabla^2}{2\mu}\phi_\nu(r) - V(r)\phi_\nu(r) = \varepsilon_\nu\phi_\nu(r)\,. \tag{A.1}$$

A Fourier transformation into k-space yields

$$-\frac{\hbar^2 k^2}{2\mu}\phi_\nu(k) - \sum_{k'} V_{k-k'}\phi_\nu(k') = \varepsilon_\nu\phi_\nu(k)\,. \tag{A.2}$$

Equation (A.2) is structurally identical to the homogeneous part of the polarization equation (3.7) in the zero density limit. For finite carrier densities, the phase-space-filling factor $(1-f^e_{\mathbf{k}_\parallel}-f^h_{\mathbf{k}_\parallel})$ modifies the eigenvalue problem such that it becomes non-hermitian

$$\tilde{\varepsilon}_{\mathbf{k}_\parallel}\phi^R_\lambda(\mathbf{k}_\parallel) - \left(1 - f^e_{\mathbf{k}_\parallel} - f^h_{\mathbf{k}_\parallel}\right)\sum_{\mathbf{k}'_\parallel} V_{\mathbf{k}_\parallel-\mathbf{k}_\parallel{}'}\phi^R_\lambda(\mathbf{k}'_\parallel) = E_\lambda\phi^R_\lambda(\mathbf{k}_\parallel) \tag{A.3}$$

and we obtain left- and right eigenfunctions $\phi^L_\lambda(\mathbf{k}_\parallel)$ and $\phi^R_\lambda(\mathbf{k}_\parallel)$ that are related via

$$\phi^L_\lambda(\mathbf{k}_\parallel) = \frac{\phi^R_\lambda(\mathbf{k}_\parallel)}{1 - f^e_{\mathbf{k}_\parallel} - f^h_{\mathbf{k}_\parallel}}\,. \tag{A.4}$$

A Fourier transformation yields the corresponding exciton wave functions in real space

$$\phi^{R/L}_\lambda(\mathbf{r}_\parallel) = \frac{1}{\sqrt{S}}\sum_{\mathbf{k}_\parallel}\phi^{R/L}_\lambda(\mathbf{k}_\parallel)e^{i\mathbf{k}_\parallel\cdot\mathbf{r}_\parallel}\,. \tag{A.5}$$

The exciton eigenfunctions are orthogonal and obey

$$\sum_{\mathbf{k}_\parallel}\phi^L_\lambda(\mathbf{k}_\parallel)\phi^R_\nu(\mathbf{k}_\parallel) = \delta_{\lambda,\nu}\,, \tag{A.6}$$

and fulfill the completeness relation

$$\sum_{\lambda}\phi^L_\lambda(\mathbf{k}_\parallel{}')\phi^R_\lambda(\mathbf{k}_\parallel) = \delta_{\mathbf{k}_\parallel{}',\mathbf{k}_\parallel}\,. \tag{A.7}$$

B. Markov approximation

In this appendix, we will review the Markov approximation. Therefore, we consider a differential equation of the form

$$i\hbar\frac{\partial}{\partial t}P = (\varepsilon_k - i\delta)\,P + S\,, \tag{B.1}$$

where S is a driving term that is oscillation mainly with the frequency $E_S/\hbar$. The formal solution of Eq. (B.1) is given by

$$P(t) = -\frac{i}{\hbar}\int_{-\infty}^{t} S(t')e^{-\frac{i}{\hbar}(\varepsilon - i\delta)(t-t')}dt'\,. \tag{B.2}$$

In order to separate the fast oscillations contained in S from the slowly varying part, we use the ansatz

$$S(t) = S_0(t)e^{-\frac{i}{\hbar}E_S t}\,, \tag{B.3}$$

where $S_0(t)$ corresponds to the slowly varying part. We insert Eq. (B.3) into Eq. (B.4). The result reads

$$P(t) = -\frac{i}{\hbar}\int_{-\infty}^{t} S_0(t')e^{\frac{i}{\hbar}(E_S - \varepsilon + i\delta)(t-t')}dt'\,. \tag{B.4}$$

Since $S_0(t')$ varies much slower than the exponential function, we can assume $S(t) \approx S(t')$. Thus, Eq. (B.4) becomes

$$P(t) \approx -\frac{i}{\hbar}S_0(t)\int_{-\infty}^{t} e^{\frac{i}{\hbar}(E_S - \varepsilon + i\delta)(t-t')}dt'\,. \tag{B.5}$$

Formally solving the integral eventually yields

$$P(t) \approx \frac{S(t)}{E_S - \varepsilon + i\gamma}\,. \tag{B.6}$$

If several driving terms are present, Eq. (B.6) becomes

$$P(t) \approx \frac{S(t)}{E_S - \varepsilon + i\gamma} + \frac{T(t)}{E_T - \varepsilon + i\gamma} + \frac{U(t)}{E_U - \varepsilon + i\gamma} + \dots\,. \tag{B.7}$$

In this thesis, we use the Markov approximation to derive a closed expression for the carrier scattering in the second Born approximation. In particular, we apply the Markov approximation to solve the equation of motion for the coherent correlation (3.19). Thus, the driving term $S(t)$ is given by the singlet contribution (3.17) that contains carrier distributions as well as polarization contributions. Since we assume quasi-stationary and Fermi distributed carriers, the main rotating frequency of the singlet term is determined by the polarization that shows rotating frequency which correspond to energies close to the fundamental band gap.

C. Analytical model for exciton lifetimes in two-quantum-well systems

In the following analysis, we investigate the photoluminescence of two QWs via an analytical model. We therefore concentrate on a situation where the photoluminescence is dominated by excitons, i.e. when the uncorrelated plasma source $f^e f^h$ in Eq. (5.8) can be neglected such that the spontaneous emission reads $\Omega_m^{SE}(\mathbf{k}_\parallel, \mathbf{q}_\parallel) = \sum_{\mathbf{l}_\parallel} \mathcal{F}_{m,\mathbf{q}_\parallel,q_\perp} c_{X\,m,m}^{\mathbf{q}_\parallel,\mathbf{k}_\parallel,\mathbf{l}_\parallel}$. As a first step we can transform Eq. (5.4) into the exciton picture using the transformation (5.17) and additionally the relation

$$\Pi_{\mathbf{q}_\parallel,q_\perp}^{\mathbf{k}_\parallel,m} = \sum_\nu \widetilde{\Pi}_{\mathbf{q}_\parallel,q_\perp}^{m,\nu} \phi_\nu(\mathbf{k}_\parallel) \; . \tag{C.1}$$

We concentrate on 1s-exciton contributions only and drop the superscript $\nu = 1s$ for notational simplicity. We obtain

$$\begin{aligned} i\hbar \frac{\partial}{\partial t} \widetilde{\Pi}_{\mathbf{q}_\parallel,q_\perp}^{m}(t) &= \left(\tilde{\epsilon}_1 - \hbar\omega_{\mathbf{q}_\parallel} - i\gamma\right) \widetilde{\Pi}_{\mathbf{q}_\parallel,q_\perp}^{m}(t) \\ &- \sum_{q'_\perp} \mathcal{F}_{m,\mathbf{q}_\parallel,q'_\perp}^{1s} \Delta\langle B_{\mathbf{q}_\parallel,q_\perp}^\dagger B_{\mathbf{q}_\parallel,q'_\perp}\rangle(t) + \sum_n i\mathcal{F}_{n,\mathbf{q}_\parallel,q_\perp}^{1s} N_{m,n}^{\mathbf{q}_\parallel}(t) \; , \end{aligned} \tag{C.2}$$

where $\tilde{\epsilon}_1$ is the 1s eigenenergy and $\mathcal{F}_{m,\mathbf{q}_\parallel,q_\perp}^{1s} \equiv d_{cv}\mathcal{E}_q U_{m,\mathbf{q}_\parallel,q_\perp} \Phi_{1s}^\star(r=0)$ with $\Phi_{1s}(r=0)$ being the 1s-exciton wave function in real space at $r = 0$. We switch on the optical coupling at time $t = 0$ and assume the excitonic correlations, Eq. (5.12), to be constant for negative times. For positive times, the correlations are determined by the radiative coupling between the QWs. In order to eliminate the dependence of Eq. (C.2) on $\Delta\langle B^\dagger B\rangle$, we formally solve Eq. (5.2) assuming the absence of any external source and insert the result in Eq. (C.2). After an additional Fourier transform, we obtain

$$\begin{aligned} \left(\hbar\Omega - \epsilon_1 + \hbar\omega_{\mathbf{q}_\parallel} + i[\gamma+\Gamma]\right) \widetilde{\Pi}_{\mathbf{q}_\parallel,q_\perp}^{m}(\Omega) = \\ -i\Gamma \sum_{n\neq m} \widetilde{\Pi}_{\mathbf{q}_\parallel,q_\perp}^{m}(\Omega) e^{i(\omega_q+\Omega)\tau_{n,m}} \\ + \sum_n i\mathcal{F}_{n,\mathbf{q}_\parallel,q_\perp}^{1s} N_{m,n}^{\mathbf{q}_\parallel}(t=0)\delta(\Omega) \\ + \sum_n i\mathcal{F}_{n,\mathbf{q}_\parallel,q_\perp}^{1s} N_{m,n}^{\mathbf{q}_\parallel}(\Omega) \; , \end{aligned} \tag{C.3}$$

with the radiative lifetime Γ defined by Eq. (6.13). The retardation time is defined by $\tau_{n,m} = |z_n - z_m|/c$ where z_n and z_m are the positions of the 2 QWs in real space and c is the speed of light. Analogously, we transform Eq. (5.12) into

$$\begin{aligned}(\hbar\Omega + i2\gamma(1-\delta_{m,n}))\, N^{\mathbf{q}_\parallel}_{m,n}(\Omega) = \\ -\sum_{\mathbf{q}_\parallel} i\mathcal{F}^{1s}_{m,\mathbf{q}_\parallel,q_\perp}\left[\widetilde{\Pi}^{n}_{\mathbf{q}_\parallel,q_\perp}\right]^\star(\Omega) - \sum_{\mathbf{q}_\parallel} i\left[\mathcal{F}^{1s}_{n,\mathbf{q}_\parallel,q_\perp}\right]^\star \widetilde{\Pi}^{m}_{\mathbf{q}_\parallel,q_\perp}(\Omega)\ . \end{aligned} \tag{C.4}$$

We solve Eq. (C.3) and insert the result into Eq. (C.4). For that purpose, we assume that initially the exciton populations in the first QW $N_{1,1}$ and the second QW $N_{2,2}$ are identical and that there are no initial electron-hole correlations $N_{1,2}$ and $N_{2,1}$ between the two QWs, such that

$$\begin{aligned} N^{\mathbf{q}_\parallel}_{1,1}(t=0) &= N^{\mathbf{q}_\parallel}_{2,2}(t=0) = N_{\mathbf{q}_\parallel}\ , \\ N^{\mathbf{q}_\parallel}_{1,2}(t=0) &= N^{\mathbf{q}_\parallel}_{2,1}(t=0) = 0\ . \end{aligned}$$

If we choose the QW spacing to be $\Delta s = \lambda/2$, the populations in both QWs as well as both correlations remain identical for all times such that we end up with a set of two equations. Taking into account that only exciton populations or electron-hole correlations with vanishing center of mass momentum contribute to the coupling of the QWs, we find the relation

$$\begin{pmatrix} \hbar\Omega_E & -2i\Gamma \\ -2i\Gamma & \hbar\Omega_O \end{pmatrix} \cdot \begin{pmatrix} N_{11}(\Omega) \\ N_{12}(\Omega) \end{pmatrix} = \begin{pmatrix} -2\Gamma\delta(\Omega)N_{\mathbf{q}_\parallel=0} \\ -4\Gamma\delta(\Omega)N_{\mathbf{q}_\parallel=0} \end{pmatrix}, \tag{C.5}$$

with $\hbar\Omega_E = \hbar\Omega + 2i\Gamma$ and $\hbar\Omega_O = \hbar\Omega + 2i\Gamma + 2\gamma$. Diagonalizing the matrix and retransforming the results for the exciton populations into time domain yields one super- and one subradiant solution. The time evolution of the excitons in both QWs is then proportional to

$$N(t) \propto \Theta(t)\left[A\cdot e^{-(\lambda_+ t)/\hbar} + B\cdot e^{-(\lambda_- t)/\hbar}\right] \tag{C.6}$$

where A and B are $\gamma-$ and $\Gamma-$dependent prefactors. The decay constants are defined by

$$\lambda_\pm = \gamma + 2\Gamma \pm \sqrt{\gamma^2 + 4\Gamma^2}\ . \tag{C.7}$$

Thus, the plus sign denotes the superradiant mode while the minus sign denotes the subradiant mode. The radiative lifetimes corresponding to these two modes are given by

$$\tau_2(\pm) = \hbar/\lambda_\pm\ . \tag{C.8}$$

Comparing this result to the exciton lifetime obtained in a single QW, we find the lifetime difference

$$\Delta\tau_{12}(\pm) = \tau_2(\pm) - \tau_1 = \tau_1 \frac{\mp\sqrt{\gamma^2+4\Gamma^2} - \gamma}{\gamma + 2\Gamma \pm \sqrt{\gamma^2+4\Gamma^2}}\ . \tag{C.9}$$

The full analysis with the help of Eqs. (5.2), (5.4), (5.12), (5.15), and (5.16) shows that for early times the superradiant mode dominates the decay of the exciton population but after some picoseconds the subradiant mode overtakes and determines the decay.

D. List of parameters

D.1. General

Symbol	Value	Description
c	299792000 m/s	vacuum speed of light
e	1.609×10^{-19} C	free-electron charge
ε_0	8.85×10^{-12} As/Vm	dielectric constant
h	6.636×10^{-34} Js	Planck's constant
$\hbar$	$h/(2\pi) = 1.054 \times 10^{-34}$ Js	Planck's constant divided by 2π
m_0	9.11×10^{-31} kg	free-electron mass

D.2. GaAs

Symbol	Value	Description
m_e	0.0665 m_0	effective electron mass
m_h	0.457 m_0	effective hole mass
m_r	0.058 m_0	reduced hole mass
a_0	12.4 nm	3D-exciton Bohr radius
ε_r	13.74	static dielectric constant
E_B	4.2 eV	3D-exciton binding energy
E_G	1.573 eV	direct band-gap energy

D.3. Ge

Symbol	Value	Description
$m_e(\Gamma)$	0.041 m_0	effective electron mass
$m_e(L)$	0.401 m_0	effective electron mass
m_h	0.25 m_0	effective hole mass
m_r	0.035 m_0	reduced hole mass
a_0	24 nm	3D-exciton Bohr radius
ε_r	15.8	static dielectric constant
E_B	1.9 eV	3D-exciton binding energy
E_G	0.881 eV	direct band-gap energy

E. List of abbreviations

Abbreviations	**Meaning**
AR-coating	anti-reflection coating
DBR	distributed Bragg reflectors
EFFA	extended filter function approximation
EID	Excitation induced dephasing
FFA	filter function approximation
hline GaAs	Gallium arsenide
Ge	Germanium
LED(s)	Light-emitting diode(s)
MQW	multi-quantum well
PL	Photoluminescence
QW(s)	quantum well(s)
SBE	Semiconductor Bloch Equations
Si	Silicon
SLE	Semiconductor Luminescence Equations
VCSEL	Vertical-Cavity Surface-Emitting Laser
VECSEL	Vertical External Cavity Surface-Emitting Laser

Bibliography

[1] B. A. Joyce, P. D. Vvendensky, and C. T. Foxon. *Growth mechanisms in MBE and CBE of III-V compounds, Handbook on Semiconductors Volume 3a*. North Holland Publishing Company, Amersterdam, 1993.

[2] K. Seeger. *Semiconductor Physics. An Introduction*. Springer-Verlag GmbH, 7. edition, 2002.

[3] S. L. Chuang. *Physics of optoelectronic devices*. Wiley, New York, 1995.

[4] E. F. Schubert. *Light-Emitting Diodes*. Cambride University Press, Cambridge, 2006.

[5] W. W. Chow and S. W. Koch. *Semiconductor Laser Fundamentals*. Springer Verlag, New York, 1. edition, 1999.

[6] W. W. Chow, S. W. Koch, and M. Sargent III. *Semiconductor Laser Physics*. Springer Verlag, Berlin, 2. edition, 1994.

[7] R. V. Steele. Laser marketplace 2007: Diode-laser market takes a breather. *Laser Focus World*, 43 (2), 2007.

[8] L. V. Keldysh and Y. V. Kopaev. Possible instability of the semimetal state toward coulomb interaction. *Soviet Phys. JETP*, 6:2219, 1965.

[9] D. W. Snoke and J. P. Wolfe. Evidence for bose-einstein condensation of excitons in cu2o. *Phys. Rev. B*, 41:11171–11184, 1990.

[10] Xuejun Zhu, P. B. Littlewood, Mark S, Hybertsen, and T. M. Rice. Exciton condensate in semiconductor quantum well structures. *Phys. Rev. Lett.*, 74:1663–1636, 1995.

[11] L. V. Butov, A. Zrenner, G. Abstreiter, G. Böhm, and G. Weimann. Condensation of indirect excitons in coupled alas/gaas quantum wells. *Phys. Rev. Lett.*, 73:304–307, 1994.

[12] L. V. Butov, A. L. Ivanov, A. Imamoglu, P. B. Littlewood, A. A. Shashkin, V. T. Dolgopolov, K. L. Campman, and A. C. Gossard. Stimulated scattering of indirect excitons in coupled quantum wells: Signature of a degenerate bose-gas of excitons. *Phys. Rev. Lett.*, 86:5608–5611, 2001.

[13] L. V. Butov, C. W. Lai, A. L. Ivanov, A. C. Gossard, and D. S. Chemla. Towards boseeinstein condensation of excitons in potential traps. *Nature*, 417:47–52, 2002.

[14] J. Kasprzak, M. Richard, S. Kundermann, A. Baas, P. Jeambrun, J. M. J. Keeling, F. M. Marchetti, M. H. Szymanska, R. Andre, J. L. Staehli, V. Savona, P. B. Littlewood, B. Deveaud, and Le Si Dang. Bose-einstein condensation of exciton polaritons. *Nature*, 443:409, 2006.

[15] F. M. Marchetti, J. Keeling, M. H. Szymanska, and P. B. Littlewood. Thermodynamics and excitations of condensed polaritons in disordered microcavities. *Phys. Rev. Lett.*, 96:066405, 2006.

[16] M. H. Szymanska, J. Keeling, and P. B. Littlewood. Nonequilibrium quantum condensation in an incoherently pumped dissipative system. *Phys. Rev. Lett.*, 96:230602, 2006.

[17] D. Sarchi and V. Savona. Long-range order in the bose-einstein condensation of polaritons. *Phys. Rev. B*, 75:115326, 2007.

[18] S. Chatterjee, C. Ell, S. Mosor, G. Khitrova, H. M. Gibbs, W. Hoyer, M. Kira, S. W. Koch, J. P. Prineas, and H. Stolz. Excitonic photoluminescence in semiconductor quantum wells: Plasma versus excitons. *Phys. Rev. Lett.*, 92:067402, 2004.

[19] M. Kira, F. Jahnke, and S. W. Koch. Microscopic theory of excitonic signatures in semiconductor photoluminescence. *Phys. Rev. Lett.*, 81:3263, 1998.

[20] M. Kira and S. W. Koch. Microscopic theory of optical excitations, photoluminescence, and terahertz response in semiconductors. *Eur. Phys. J. D*, 36:143, 2005.

[21] J. Cerne, J. Kono, M. S. Sherwin, M. Sundaram, A. C. Gossard, and G. E. W. Bauer. Terahertz dynamics of excitons in GaAs/AlGaAs quantum wells. *Phys. Rev. Lett.*, **77**:1131–1134, 1996.

[22] I. Galbraith, R. Chari, S. Pellegrini, P. J. Phillips, C. J. Dent, A. F. G. van der Meer, D. G. Clarke, A. K. Kar, G. S. Buller, C. R. Pidgeon, B. N. Murdin, J. Allam, and G. Strasser. Excitonic signatures in the photoluminescence and terahertz absorption of a gaas/al$_x$ga$_{1-x}$as multiple quantum well. *Phys. Rev. B*, **71**:073302, 2005.

[23] M. Kira, W. Hoyer, and S. W. Koch. Terahertz signatures of the exciton formation dynamics in non-resonantly excited semiconductors. *Solid State Commun.*, 129:733, 2004.

[24] M. Kira and S. W. Koch. Exciton-population inversion and terahertz gain in resonantly excited semiconductors. *Phys. Rev. Lett.*, 93:076402, 2004.

[25] W. Hoyer, A. Knorr, J. V. Moloney, E. M. Wright, M. Kira, and S. W. Koch. Photoluminescence and terahertz emission from femtosecond laser-induced plasma channels. *Phys. Rev. Lett.*, 94:115004, 2005.

[26] D. F. Walls and G. J. Milburn. *Quantum Optics*. Springer-Verlag, New York, 1. edition, 1994.

[27] E. Moreau, I. Robert, L. Manin, V. Thierry-Mieg, J. M. Gérard, and I. Abram. Quantum cascade of photons in semiconductor quantum dots. *Phys. Rev. Lett.*, 87:183601, 2001.

[28] O. Benson, C. Santori, M. Pelton, and Y. Yamamoto. Regulated and entangled photons from a single quantum dot. *Phys. Rev. Lett.*, 84:2513, 2000.

[29] Y.-S. Lee, T. B. Norris, M. Kira, F. Jahnke, S. W. Koch, G. Khitrova, and H. M. Gibbs. Quantum correlations and intraband coherences in semiconductor cavity QED. *Phys. Rev. Lett.*, 83:5338, 1999.

[30] C. Ell, P. Brick, M. Hübner, E. S. Lee, O. Lyngnes, J. P. Prineas, G. Khitrova, H. M. Gibbs, M. Kira, F. Jahnke, S. W. Koch, D. G. Deppe, and D. L. Huffaker. Quantum correlations in the nonperturbative regime of semiconductor microcavities. *Phys. Rev. Lett.*, 85:5392–5395, 2000.

[31] M. Kira and S. W. Koch. Many-boy correlations and exciton effects in semiconductor spectroscopy. *Prog. in Quant. Electr.*, 30:155, 2006.

[32] G. Khitrova, H. M. Gibbs, F. Jahnke, M. Kira, and S. W. Koch. Nonlinear optics of normal-mode-coupling semiconductor microcavities. *Rev. Mod. Phys.*, 71:1591, 1999.

[33] M. Kira, F. Jahnke, and S. W. Koch. Quantum theory of secondary emission in optically excited semiconductor quantum wells. *Phys. Rev. Lett.*, 82:3544, 1999.

[34] M. Kira, F. Jahnke, W. Hoyer, and S. W. Koch. Quantum theory of spontaneous emission and coherent effects in semiconductor microstructures. *Prog. in Quant. Electr.*, 23:189, 1999.

[35] H. Haug and S. W. Koch. *Quantum Theory of the Optical and Electronic Properties of Semiconductors*. World Scientific Publ., Singapore, 4. edition, 2004.

[36] C. Cohen-Tannoudji, J. Dupont-Roc, and G. Grynberg. *Photons & Atoms*. Wiley, New York, 3. edition, 1989.

[37] M. Kira. *Complementary Quantum Dynamics*. Report Series in Theoretical Physics, Research Institude for Theoretical Physics, University of Helsinki, Helsinki, Finland, 1995.

[38] E. Mertzbacher. *Quantum mechanics*. Wiley, New York, 3. edition, 1998.

[39] M. Born and E. Wolf. *Principles of Optics, Electromagnetic Theory of Propagation, Interference and Diffraction of Light*. Cambridge University Press, Cambridge, 7. edition, 1999.

[40] H. W. Wyld and B. D. Fried. Quantum mechanical kinetic equations. *Annals of Physics*, 23(3):374, 1963.

[41] J. Fricke. Transport equations including many-particle correlations for an arbitrary quantum system: A general formalism. *Annals of Physics*, 252(2):479, 1996.

[42] T. Rappen, U. G. Peter, M. Wegener, and W. Schäfer. Polarization dependence of dephasing processes: A probe for many-body effects. *Phys. Rev. B*, 49:10774, 1994.

[43] F. Jahnke, M. Kira, S. W. Koch, G. Khitrova, E. K. Lindmark, T. R. Nelson Jr., D. V. Wick, J. D. Berger, O. Lyngnes, H. M. Gibbs, and K. Tai. Excitonic nonlinearities of semiconductor microcavities in the nonperturbative regime. *Phys. Rev. Lett.*, 77:5257, 1996.

[44] F. Jahnke, M. Kira, and S. W. Koch. Linear and nonlinear optical properties of quantum confined excitons in semiconductor microcavities. *Z. Physik B*, 104:559, 1997.

[45] W. Schafer, R. Lövenich, N. A. Fromer, and D. S. Chemla. From coherently excited highly correlated states to incoherent relaxation processes in semiconductors. *Phys. Rev. Lett.*, 86:344, 2001.

[46] S. Mukamel. *Principles of Nonlinear Optical Spectroscopy*. Oxford University Press, USA, 1995.

[47] J. Shah. *Ultrafst Spectroscopy of Semiconductors and Semiconductor Nanostructures*. Springer, 1996.

[48] M. Brinkmann, J. Hayden, and M. Letz. *Handbook of Lasers and Optics*. Springer, New York, 2007.

[49] N. F. Mott. The transition to the metallic state. *Philos. Mag.*, 6:287–309, 1961.

[50] H. Haug and S. Schmitt-Rink. Electron theory of the optical properties of laser excited semiconductors. *Prog. in Quant. Electr.*, 9:3, 1984.

[51] W. W. Chow, A.F. Wright, A. Girndt, F. Jahnke, and S. W. Koch. Microscopic theory of gain in an inhomogeneously broadened ingan-algan quantum-well laser. *Appl. Phys. Lett.*, 71:2608–2610, 1197.

[52] C. Lange, N. Köster, M. Schäfer, M. Kira, S.W. Koch, D. Chrastina, G. Isella, H.v. Känel, H. Sigg, and S. Chatterjee. Transient gain and optical amlification in Ge/SiGe/Si heterostructures. *to be puplished*, 2008.

[53] G. Hernandez. *Fabry-Perot interferometers*. Cambridge University Press, Cambridge, 1986.

[54] V. M. Agranovich and O. A. Dubowskii. Effect of retarded interaction of exciton spectrum in 1-dimensional and 2-dimensional crystals. *JETP Lett.*, 3:223, 1966.

[55] J. Feldmann, G. Peter, E. O. Göbel, P. Dawson, K. Moore, C. Foxon, and R. J. Elliott. Linewidth dependence of radiative exciton lifetimes in quantum wells. *Phys. Rev. Lett.*, 59:2337, 1987.

[56] E. Hanamura. Rapid radiative decay and enhanced optical nonlinearity of excitons in a quantum well. *Phys. Rev. B*, 38:1228, 1988.

[57] B. Deveaud, F. Clérot, N. Roy, K. Satzke, B. Sermage, and D. S. Katzer. Enhanced radiative recombination of free excitons in GaAs quantum wells. *Phys. Rev. Lett.*, 67:2355, 1991.

[58] P. W. M. Blom, P. J. Vanhall, C. Smit, J. P. Cuypers, and J. H. Wolter. Selective exciton formation in thin GaAs/$Al_xGa_{1-x}As$ quantum wells. *Phys. Rev. Lett.*, 71:3878, 1993.

[59] A. Vinattieri, J. Shah, T. C. Damen, D. S. Kim, L. N. Pfeiffer, M. Z. Maialle, and L. J. Sham. Exciton dynamics in GaAs quantum-wells under resonant excitation. *Phys. Rev. B*, 50:10868, 1994.

[60] R. Kumar, A. S. Vengurlekar, A. V. Gopal, T. Melin, F. Laruelle, B. Etienne, and J. Shah. Exciton formation and relaxation dynamics in quantum wires. *Phys. Rev. Lett.*, 81:2578, 1998.

[61] P. Borri, W. Langbein, J. M. Hvam, and F. Martelli. Well-width dependence of exciton-phonon scattering in $In_xGa_{1-x}As$/GaAs single quantum wells. *Phys. Rev. B*, 59:2215, 1999.

[62] B. Mieck, H. Haug, W. A. Hügel, M. F. Heinrich, and M. Wegener. Quantum-kinetic dephasing in resonantly excited semiconductor quantum wells. *Phys. Rev. B*, 62:2686, 2000.

[63] A. Thränhardt, S. Kuckenburg, A. Knorr, T. Meier, and S. W. Koch. Quantum theory of phonon-assisted exciton formation and luminescence in semicondutor quantum wells. *Phys. Rev. B*, 62:2706, 2000.

[64] W. Hoyer, M. Kira, and S. W. Koch. Influence of coulomb and phonon interaction on the exciton formation dynamics in semiconductor heterostructures. *Phys. Rev. B*, 67:155113, 2003.

[65] F. Tassone, F. Bassani, and L. C. Andreani. Quantum-well reflectivity and exciton-polariton dispersion. *Phys. Rev. B*, 45:6023, 1992.

[66] M. Kira and S. W. Koch. Quantum-optical spectroscopy of semiconductors. *Phys. Rev. A*, 73:013813, 2006.

[67] W. Hoyer, C. Ell, M. Kira, S. W. Koch, S. Chatterjee, S. Mosor, G. Khitrova, H. M. Gibbs, and H. Stolz. Many-body dynamics and exciton formation studied by time-resolved photoluminescence. *Phys. Rev. B*, 72:075324, 2005.

[68] S. W. Koch, M. Kira, and G. Khitrova abd H. M. Gibbs. Semiconductor excitons in new light. *Nature Materials*, 5:523–531, 2006.

[69] W. Hoyer, M. Kira, S. W. Koch, J. Hader, and J. V. Moloney. Coulomb effects on quantum-well luminescence spectra and radiative recombination times. *J. Opt. Soc. Am.*, 24:1344, 2007.

[70] M. Kira, F. Jahnke, S. W. Koch, J. D. Berger, D. V. Wick, T. R. Nelson Jr., G. Khitrova, and H. M. Gibbs. Quantum theory of nonlinear semiconductor microcavity luminescence explaining "boser" experiments. *Phys. Rev. Lett.*, 79:5170, 1997.

[71] C. Weisbuch, M. Nishioka, A. Ishikawa, and Y. Arakawa. Observation of the coupled exciton-photon mode splitting in a semiconductor quantum microcavity. *Phys. Rev. Lett.*, 69:3314, 1992.

[72] M. Kira, W. Hoyer, T. Stroucken, and S. W. Koch. Exciton formation in semiconductors and the influence of a photonic environment. *Phys. Rev. Lett.*, 87:176401, 2001.

[73] E. M. Purcell. Spontaneous emission probabilities at radio frequencies. *Phys. Rev.*, 69:681, 1946.

[74] F. D. Martini, G. Innocenti, G. R. Jacobovitz, and P. Mataloni. Spontaneous emission probabilities at radio frequencies. *Phys. Rev. Lett.*, 59:2955–2958, 1987.

[75] J. Martorell and N. M. Lawandy. Observation of inhibited spontaneous emission in a periodic dielectric structure. *Phsy. Rev. Lett.*, 65:1877–1880, 1990.

[76] J. P. Dowling and C. M. Bowden. Atomic emission rates in inhomogeneous media with applications to photonic band structures. *Phsy. Rev. A*, 46:612–622, 1992.

[77] A. G. Kofman, G. Kurizki, and B. Sherman. Spontaneous and induces atomic decay in photonic band structures. *J. Mod. Opt.*, 41:353–384, 1994.

[78] M. D. Tocci, M. Scalora, M. J. Bloemerand J. P. Dowling, and C. M. Bowden. Measurement of spontaneous-emission enhancement near the on-dimensional photonic band edge of semiconductor heterostructures. *Phys. Rev. A*, 53:2799, 1996.

[79] P. Lambropoulos, G. M. Nikolopoulos, T. R. Nielsen, and S. Bay. Fundamental quantum optics in structured reservoirs. *Rep. Prog. Phys*, 63:455–503, 2000.

[80] E. Yablonovitch. Inhibited spontaneous emission in solid-state physics and electronics. *Phys. Rev. Lett.*, 58:2059–2062, 1987.

[81] R. E. Slusher and C. Weisbuch. Optical microcavities in condensed matter systems. *Solid State Commun.*, 92:149–158, 1994.

[82] G. Khitrova, H.M. Gibbs, M. Kira, S.W. Koch, , and A. Scherer. Vacuum rabi splitting in semiconductors. *Nature Physics*, 2:81–90, 2006.

[83] I. Abram, S. Iung, R.Kuszelewicz, G. Le Rouc, C. Licoppe, J. L. Oudar, E. V. K. Rao, J. I. Bloch, R. Planel, and V. Thierry-Mieg. Nonguiding half-wave semiconductor microcavitites desplaying the exciton-photon mode splitting. *App. Phys. Lett.*, 65:2516, 1994.

[84] M. Schafer, W. Hoyer, M. Kira, and S. W. Koch. Influence of dielectric environment on quantum-well luminescence spectra. *J. Opt. Soc. Am. B*, 25:187, 2008.

[85] M. Schafer, M. Werchner, W. Hoyer, M. Kira, and S. W. Koch. Quantum theory of luminescence in multiple-quantum-well bragg structures. *Phys. Rev. B*, 74:155315, 2006.

[86] R. H. Dicke. Coherence in spontaneous radiation processes. *Phys. Review*, 93(1):99, 1954.

[87] Y. C. Lee and P. S. Lee. Coherent radiation from thin films. *Phys Rev. B*, 10:344, 1974.

[88] S. Haas, T. Stroucken, M. Hubner, J. Kuhl, B. Grote, F. Jahnke, S. W. Koch, R. Hey, and K. Ploog. Intensity dependence of superradiant emission from radiatively coupled excitons in multiple-quantum-well bragg structures. *Phys. Rev. B*, 57:14860–14868, 1998.

[89] B. Laikhtman and L. D. Shvartsman. Superradiance of nearly condensed excitons in inas-gasb coupled quantum wells. *Phys Rev. B*, 72:245333, 2005.

[90] B. I. Mantsyzov. Gap 2π pulse with an inhomogeneously broadened line and an oscillating solitary wave. *Phys Rev. A*, 51:4939, 1995.

[91] B. I. Mantsyzov, I. V. Mel'nikov, and J. S. Aitchison. Dynamic control over optical solitons in a resonant photonic crystal. *IEEE J. Quantum Electron.*, 10:893–899, 2004.

[92] I. V: Mel'nikov, J. S. Aitchison, and B. I. Matsyzov. Dynamic control over optical solitons in a resonant photonic crystal. *Opt. Lett.*, 29:289–291, 2004.

[93] T. Stroucken, A. Knorr, P. Thomas, and S. W. Koch. Coherent dynamics of radiatively coupled quantum-well excitons. *Phys. Rev. B*, 53:2026, 1996.

[94] M. Hubner, J. P. Prineas, C. Ell, P. Brick, E. S. Lee, G. Khitrova, H. M. Gibbs, and S. W. Koch. Optical lattices achieved by excitons in periodic quantum well structures. *Phys. Rev. Lett.*, 83:2841–2844, 1999.

[95] T. Shih, K. Reimann, M. Woerner, T. Elsaesser, I. Waldmuller, A. Knorr, R. Hey, and K. H. Ploog. Nonlinear response of radiatively coupled intersubband transitions of quasi-two-dimensional electrons. *Phys. Rev. B*, 72:195338, 2005.

[96] I. Waldmueller, W. W. Chow, and A. Knorr. Influence of radiative coupling on coherent rabi intersubband oscillations in multiple quantum wells. *Phys. Rev. B*, 73:035433, 2006.

[97] Y. Merled'Aubigne, A. Wasiela, H. Mariette, and T. Dietl. Polariton effects in multiple-quantum-well structures of cdte/$Cd_{1-x}Zn_x$te. *Phys. Rev. B*, 54:14003, 1996.

[98] L. C. Andreani, F. Tassone, and F. Bassani. Radiative lifetime of free excitons in quantum wells. *Solid State Commun.*, 77:641, 1991.

Publications

Paper

- C. Lange, N. Köster, M. Schäfer, M. Kira, S.W. Koch, D. Chrastina, G. Isella, H.v. Känerl, H. Sigg, and S. Chatterjee, *Transient Gain and Optical Amplification in Ge/SiGe/Si Heterostructures*, to be published
- M. Schäfer, W. Hoyer, M. Kira, and S.W. Koch,*Influence of Dielectric Environment on Quantum-Well Luminescence Spectra*, J.Opt.Soc.Am. B **25** 187 (2008)
- M. Schäfer, M. Werchner, W. Hoyer, M. Kira, and S.W. Koch, *Quantum Theory of Luminescenence in Multiple-Quantum-Well Bragg structures*, Phys.Rev. B **74** 166315 (2006)

Poster and Talks

- M. Schäfer, M. Kira, S.W. Koch, C. Lange, N. Köster, and S. Chatterjee, Talk: *Optical Non-Linearities in Quantum Wells with Indirect Band-Gap*, Materialforschungstag Mittelhessen Marburg, Germany (June 20, 2008)
- M. Werchner, M. Schäfer, W. Hoyer, M. Kira, and S.W. Koch, Talk: *Microscopic Investigations of Luminescence from Muliple Quantum-Well Structures*, DPG spring meeting Regensburg, Germany (March 26-30, 2007)
- M. Schäfer, W. Hoyer, M. Kira, S.W. Koch, M. Reichelt, J. Hader, and J.V. Moloney, Talk: *Semiconductor Laser Emission in Realistic Dielectric Structures*, DPG spring meeting Regensburg, Germany (March 26-30, 2007)
- M. Schäfer, M. Werchner, W. Hoyer, M. Kira, and S.W. Koch, Talk: *Radiative Lifetime of Excitons in Multi Quantum-Well systems*, DPG spring meeting Dresden, Germany (March 26-31, 2006)
- M. Werchner, M. Schäfer, W. Hoyer, M. Kira, and S.W. Koch, Talk: *Quantum-optical and classical spectroscopy with radiatively coupled quantum wells*, DPG spring meeting Frankfurt, Germany (March 13-17, 2006)
- M. Schäfer, M. Werchner, M. Kira, and S.W. Koch, Poster: *Multi Quantu-Well Luminescence*, Clif-Hotel Sellin/Rügen, Germany (March 14-17, 2004)

Danksagung

Ein ganz besonderer Dank gebührt meinen Eltern, die mich von Anfang an im Studium und während meiner Promotion unterstützt und mir den Rücken freigehalten haben. Ohne ihre Hilfe hätte ich mich sicherlich nicht in diesem Maße auf diese Doktorarbeit konzentrieren können. Sie haben somit einen wesentlichen Anteil an ihrem Zustandekommen. Außerdem danke ich meinem Bruder Stefan für die begleitenden Kommentare, die mich nach einer "tollen Entdeckung" schnell wieder auf den Boden der Tatsachen zurückgebracht haben und überhaupt für die gute Laune, die er immer versprüht. Beides sind notwendige Voraussetzungen, um abseits der Physik die Energie zu tanken, die für eine konzentrierte Arbeit so notwendig ist.
Ein besonderer Dank gebührt auch Prof. Dr. Stephan Koch für die Vergabe des interessanten Themas und die stetige Unterstützung und Förderung während meiner Promotionszeit. Außerdem danke ich Prof. Dr. Mackillo Kira und Dr. Walter Hoyer für die jahrelange enge Zusammenarbeit und die vielen fruchtbaren Diskussionen. Ohne ihren Rat oder ihre Bereitschaft, ihr Wissen mit mir zu teilen, wäre diese Arbeit sicherlich nicht in dieser Form entstanden.
Ich bedanke mich bei allen Mitgliedern der Arbeitsgruppe für die häufig sehr hilfreichen Diskussionen und Anregungen, die meine Arbeit positiv beeinflusst haben, und überhaupt für das nette und konstruktive Arbeitsklima. Besonderer Dank gebührt hier vor allem PD Dr. habil. Angela Thränhardt und Marco Werchner für die Nachhilfestunden in Sachen Englisch, und Ada Bäumner, die mir in der Endphase meiner Promotion viel Arbeit bei den Quantenmechanik-Tutorien abgenommen und mir somit Zeit für die Fertigung dieser Arbeit verschafft hat.
Ein herzlicher Dank gebührt auch PD Dr. habil. Wolfgang Stolz für die Übernahme des Zweitgutachtens.
Des weiteren bedanke ich mich bei Niko Köster, Christoph Lange und Dr. Sangam Chatterjee für die Zusammenarbeit bei den indirekten Halbleitern. Bei Niko Köster und Christoph Lange möchte ich mich auch noch mal für die kurze Einführung in die Messtechnik bedanken. Prof. Dr. Jerome Molonoy und seiner Arbeitsgruppe, insbesondere Colm Dineen und Hongbo Li, möchte ich gerne für die Zusammenarbeit bei den Filterfunktionen für die Lumineszenzrechnungen danken. Herzlichen Dank auch an Prof. Dr. Steve Cundiff und seine Arbeitsgruppe, insbesondere an Ryan Patrick Smith, für die Zusammenarbeit bei der Untersuchung des Einflusses der dielektrischen Umgebung auf die optische Antwort in Quantenfilmen.
Vielen Dank auch an alle Freunde, insbesondere in Kirchhain und Albshausen, für die vielen tollen Stunden abseits der Uni. Ihr habe es geschafft mich immer wieder aufzubauen, wenn sich die Natur mal wieder nicht in eine meiner Theorie pressen ließ. Es wird sicherlich eine Nachbesprechung dieser Arbeit in ungezwungem Rahmen geben.
Zu guter letzt möchte ich mich bei meiner Frau Marianne bedanken für die unendliche Geduld mit mir, den großen Rückhalt und die immerwährende Unterstützung. Du bist mit mir durch Dick und Dünn gegangen. Danke für jeden Moment mir Dir!!